

Non-Classical State Engineering for Quantum Networks

Von der Fakultät für Mathematik und Physik der
Gottfried Wilhelm Leibniz Universität Hannover
zur Erlangung des Grades

Doktorin der Naturwissenschaften
- Dr. rer. nat. -

genehmigte Dissertation von

Dipl.-Phys. Christina E. Vollmer

geboren am 30. Juni 1986 in Gütersloh

2014

Referent: Prof. Dr. Roman Schnabel
Korreferent: Prof. Dr. Karsten Danzmann
Tag der Promotion: 24.01.2014

Abstract

The wide field of quantum information processing and quantum networks has developed very fast in the last two decades. Besides the regime of discrete variables, which was developed first, the regime of continuous variables represents an alternative approach to realize many quantum applications. Non-classical states of light, like squeezed or entangled states, are a fundamental resource for quantum applications like quantum repeaters, quantum memories, quantum key distribution, quantum spectroscopy, and quantum metrology. These states can be generated successfully in the infrared wavelength regime. However, for some tasks other wavelengths, especially in the visible wavelength regime, are desirable. To generate non-classical states of light in this wavelength regime frequency up-conversion can be used, since all quantum properties are maintained in this process. The first part of this thesis deals with the experimental frequency up-conversion of quantum states. Squeezed vacuum states of light at 1550 nm were up-converted to 532 nm and a noise reduction of -1.5 dB at 532 nm was achieved. These states can be used for increasing the sensitivity of gravitational wave detectors or spectroscopic measurements. Furthermore, one part of an entangled state at 1550 nm was up-converted to 532 nm and, thus, entanglement between these two wavelengths was generated and characterized to -1.4 dB following Duan *et al.*. With such a quantum link it is possible to establish a quantum network, which takes advantage of the low optical loss at 1550 nm for information transmission and of atomic transitions around 532 nm for a quantum memory in a quantum repeater. For quantum networks the distribution of entanglement and especially of a quantum key is essential. In the second part of this thesis the experimental distribution of entanglement by separable states is demonstrated. The underlying protocol requires a special three-mode state, which is separable in two of the three splittings. With this state, entanglement between two distant parties can be established by sending only separable modes. This seemingly paradoxical protocol was experimentally realized for the first time within this thesis. Thereby, new and non-intuitive insights in the quantum world and its special properties are revealed.

Keywords: quantum networks, entanglement, squeezed states, frequency conversion

Kurzfassung

Das weite Feld der Quanteninformationsverarbeitung und Quantennetzwerke hat sich in den letzten 20 Jahren rapide entwickelt. Neben dem Bereich der diskreten Variablen, der zuerst entwickelt wurde, ist der Bereich der kontinuierlichen Variablen ein alternativer Zugang, um viele Quantenanwendungen zu realisieren. Nicht-klassische Zustände des Lichts, wie verschränkte oder gequetschte Zustände, sind fundamentale Hilfsmittel für Quantenanwendungen wie Quantenrepeater, Quantenspeicher, Quantenschlüsselverteilung, Quantenspektroskopie und Quantenmetrologie. Diese Zustände können im infraroten Wellenlängenbereich erfolgreich hergestellt werden. Allerdings sind für manche Anwendungen andere Wellenlängen, insbesondere im sichtbaren Bereich, wünschenswert. Um nicht-klassische Zustände in diesem Wellenlängenbereich herzustellen, kann Frequenzkonversion verwendet werden, da bei diesem Prozess die Quanteneigenschaften erhalten bleiben. Der erste Teil dieser Arbeit behandelt die experimentelle Frequenzkonversion von Quantenzuständen. Gequetschte Vakuumzustände des Lichts wurden von 1550 nm zu 532 nm hochkonvertiert, wobei eine Rauschunterdrückung von -1.5 dB erreicht wurde. Diese Zustände können für die Erhöhung der Sensitivität von Gravitationswellendetektoren oder spektroskopischen Messungen benutzt werden. Weiterhin wurde ein Teil eines verschränkten Zustands bei 1550 nm zu 532 nm hochkonvertiert und somit Verschränkung von -1.4 dB nach Duan *et al.* zwischen diesen beiden Wellenlängen erzeugt. Mit solch einer Quantenverbindung ist es möglich, ein Quantennetzwerk aufzubauen, das die geringen Verluste bei 1550 nm für die Informationsübertragung und atomare Übergänge um 532 nm für Quantenspeicher in Quantenrepeatern ausnutzt. Für Quantennetzwerke ist die Verteilung von Verschränkung und insbesondere eines Quantenschlüssels essentiell. Im zweiten Teil dieser Arbeit ist die experimentelle Verteilung von Verschränkung mit separablen Zuständen gezeigt. Das zugrunde liegende Protokoll erfordert einen speziellen Dreimodenzustand, der in zwei von drei Teilungen separabel ist. Mit diesem Zustand kann durch das Versenden von ausschließlich separablen Moden Verschränkung zwischen zwei entfernten Parteien erzeugt werden. Dieses scheinbare paradoxe Protokoll wurde im Rahmen dieser Arbeit erstmals realisiert. Dadurch werden neue und nicht-intuitive Einblicke in die Quantenwelt und ihren besonderen Eigenschaften sichtbar.

Schlüsselworte: Quantennetzwerke, Verschränkung, gequetschte Zustände, Frequenzkonversion

Contents

Abstract	i
Kurzfassung	iii
Glossary	xiii
1 Introduction	1
1.1 Quantum Networks	1
1.2 Quantum Spectroscopy and Imaging	3
1.3 Quantum Metrology	4
1.4 Structure of the Thesis	5
2 Theory of Non-Classical States of Light	7
2.1 Quantization of the Electro-Magnetic Field	7
2.2 Quadrature Operators	8
2.3 Density Operator	9
2.4 Wigner Function	9
2.5 Fock States	10
2.6 Coherent States	12
2.7 Squeezed States	13
2.7.1 Squeezed States and Optical Loss	14
2.8 The Class of Gaussian States	15
2.9 Gaussian Entangled States	16
2.9.1 Entanglement Criteria	17
2.9.2 Generation of Gaussian Entanglement	19

3	Nonlinear Processes	23
3.1	Basic Concepts	24
3.2	Sum-Frequency Generation in Classical Optics	24
3.3	Quantum Up-Conversion via Sum-Frequency Generation	29
3.4	Difference Frequency Generation and Optical Parametric Oscillation in Classical Optics	30
3.5	Quantum Description of Parametric Down Conversion	38
3.6	Phase-Matching	39
4	Basic Experimental Techniques	41
4.1	Squeezed-Light Generation	41
4.2	Homodyne Detection	42
4.3	Single Sideband Locking Scheme	44
4.4	Thermal State Generation	46
5	Quantum Up-Conversion	49
5.1	Experimental Setup	50
5.1.1	Laser Preparation	50
5.1.2	Non-Degenerate Optical Parametric Oscillator (NOPO)	52
5.1.3	Squeezed-Light Generation	55
5.1.4	Sum-Frequency Generation (SFG)	56
5.1.5	Homodyne Detectors	57
5.2	Squeezing Conversion	59
5.3	Entanglement Conversion	62
5.4	Conclusion	66
6	Entanglement Distribution by Separable States	69
6.1	Protocol of Entanglement Distribution by Separable States	70
6.2	Requirements for the three-mode state	71
6.3	Experimental Setup	75
6.3.1	Laser Source	75
6.3.2	Squeezed-Light Sources	75
6.3.3	Three-Mode State Preparation	78
6.3.4	Entanglement Distribution	78
6.4	Measurement Procedure	79
6.4.1	Reconstruction of the Covariance Matrix	79
6.4.2	Verifying the Entanglement	81
6.5	Results	81

6.6	Discussion	84
6.6.1	Inefficient Homodyne Detection	87
6.6.2	Phase Noise	89
6.6.3	Statistical Errors	91
6.7	Conclusion	91
7	Conclusion	93
A	Python Simulation	95
	Bibliography	98
	List of Publications	111
	Acknowledgments	113
	Curriculum Vitae	115

List of Figures

1.1	Principle of an optical quantum network	2
1.2	Methods to improve the sensitivity of a Michelson interferometer	4
2.1	Wigner functions of a vacuum and a coherent state	11
2.2	Wigner function of a squeezed vacuum state	14
2.3	Influence of optical loss on the squeezing strength	15
2.4	Entanglement generation with a squeezed vacuum state and a vacuum state at a balanced beam splitter	19
3.1	Principle of sum-frequency generation	26
3.2	Spatial variation of the sum-frequency field	29
3.3	Principle of optical parametric oscillation	31
3.4	Principle of difference frequency generation	32
3.5	Spatial variation of the generated fields from difference frequency generation	33
3.6	Gain profile and mode structure of a doubly resonant OPO	35
3.7	Visualization of mode hops and cluster jumps of an OPO	36
3.8	Mode hops and cluster jumps of an OPO	37
3.9	Different methods of phase-matching	40
4.1	Experimental generation of squeezed states	42
4.2	Principle of homodyne detection	43
4.3	Stabilization scheme of a phase gate	45
4.4	Error signals for stabilizing a phase gate	46
4.5	Generation of a thermal state	47
5.1	Schematic of quantum up-conversion of a squeezed vacuum field from 1550 nm to 532 nm	50
5.2	Experimental setup of quantum up-conversion	51

5.3	Wavelength tuning of the NOPO	53
5.4	Output power and conversion efficiency of the NOPO	54
5.5	Conversion efficiency of the SFG	58
5.6	Characterization of the homodyne detectors	58
5.7	Measurement of the up-converted squeezed vacuum states at 532 nm .	60
5.8	Experimental setup of entanglement conversion	62
5.9	Results of entanglement measurement between 1550 nm and 532 nm .	64
5.10	Result of squeezing conversion with an additional balanced beam splitter	65
6.1	Principle of entanglement distribution by separable states	70
6.2	State preparation scheme of the three-mode state	71
6.3	PPT_B value with respect to the variance of the initial states	73
6.4	PPT_B value for different variances of the input states	73
6.5	PPT_B value with respect to the thermal state's variance	74
6.6	Experimental setup for the entanglement distribution by separable states	76
6.7	Data Acquisition	79
6.8	Schematic of the experimental setup	82
6.9	Variation of the squeezed input state – Theory and experimental results	85
6.10	Experimental setup including effects that can potentially mask en- tanglement of the resulting three-mode state.	86
6.11	PPT values versus detection loss	88
6.12	Measured PPT values with subtraction of detection loss	88
6.13	QQ-plots of the homodyne data	90

List of Tables

5.1	Parameters of the two coupling mirrors for the SHG and OPA	55
5.2	Parameters of the two incoupling mirrors for the SFG	56
5.3	Optical efficiency of the squeezing measurement	60
5.4	Improvements for squeezing up-conversion	61
6.1	Homodyne detector settings for the reconstruction of the three-mode covariance matrix	80
6.2	Experimental results for different squeezed input states	84

Glossary

List of Abbreviations



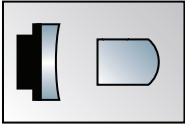
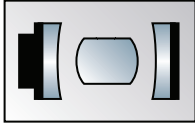




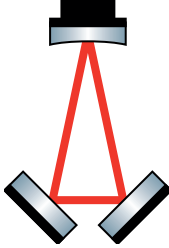
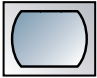
AC	alternating current
BHD	balanced homodyne detector
BS	beam splitter
CV	continuous variables
DBS	dichroic beam splitter
DC	direct current
EOM	electro-optic modulator
DFG	difference frequency generation
HD	homodyne detector
LO	local oscillator
MC	mode cleaner
OPA	optical parametric amplifier
OPO	optical parametric oscillator
PBS	polarization beam splitter
PD	photodiode
PDH	Pound-Drever-Hall
PPKTP	periodically poled potassium titanyl phosphate
PPT	positive partial transposition
PS	phase shifter
PZT	piezo-actuated transducer
SFG	sum-frequency generation
SHG	second harmonic generation
SSB	single side band
UV	ultra violet

List of Symbols

\hat{a}_k	annihilation operator
\hat{a}_k^\dagger	creation operator
α	complex amplitude
α_i	absorption coefficient at frequency ω_i
c_0	speed of light in vacuum
$\chi^{(N)}$	susceptibility N th order
ξ	quadrature vector
\hat{D}	displacement operator
d_{eff}	effective susceptibility
\mathbf{E}	quantized electric field
ϵ_0	dielectric permittivity
\mathbf{e}_k	polarization vector
η	efficiency
γ	covariance matrix
\hat{H}	Hamilton operator
\hbar	reduced Planck constant
\mathcal{I}	Duan value
\hbar	reduced Planck constant
\mathbf{k}	wave vector
Δk	wave vector mismatch
l	optical loss
m	modulation index
n_i	refractive index at frequency ω_i
\hat{n}	number operator
Ω	symplectic matrix
ω	angular frequency
\mathbf{P}	polarization vector
P_n	photon number statistic
\hat{P}	phase quadrature operator
r	squeezing parameter
$\hat{\rho}$	density operator
V	second-order covariance matrix
Var	variance
\hat{X}	amplitude quadrature operator
ξ	squeezing parameter

List of Pictograms

The following pictograms were designed by Alexander Franzen and used within this thesis in schematics of experimental setups.

	beam dump
	beam splitter
	cavity for second harmonic generation
	cavity for sum-frequency generation
	dichroic beam splitter
	electro-optical modulator
	faraday isolator
	lowpass filter
	mode cleaner
	non-degenerate optical parametric oscillator

List of Tables



phase shifter



phase shifter



photo diode



polarizing beam splitter



sine frequency generator

Introduction

Since 1935, when the famous paper “Can quantum-mechanical description of physical reality be considered complete” from Albert Einstein, Boris Podolsky, and Nathan Rosen was published [Ein35], quantum physics has been one of the most fascinating topics in the world of physics. So far, there have been many astonishing phenomena which can only be explained by quantum physics and often contradict our natural intuition. One of the first experimental proofs for the completeness of the quantum-mechanical description was given by Alain Aspect in 1982 [Asp82]. Since then, lots of experiments have been conducted to verify the predicted phenomena, and nowadays there is no doubt about the completeness of the quantum-mechanical description. In fact, quantum physics has become a fundamental and crucial resource for quantum networks and communication. In addition, quantum states have important application in other fields such as metrology, imaging or spectroscopy.

This thesis deals with the frequency up-conversion of squeezed and entangled states of light and the experimental distribution of entanglement by separable states. Both topics have in common that the special properties of the generated quantum states are important tools for establishing quantum networks. It was shown that squeezed states in particular, also have applications in quantum metrology and quantum imaging. These applications will be discussed in the following sections.

1.1 Quantum Networks

Quantum networks distribute non-classical states of light, like squeezed or entangled states, and thereby connect two distant parties. Quantum networks are required for secure communication via quantum key distribution [Gob04, Fur12] and for the realization of quantum teleportation schemes [Bou97, Bow03]. Quantum states

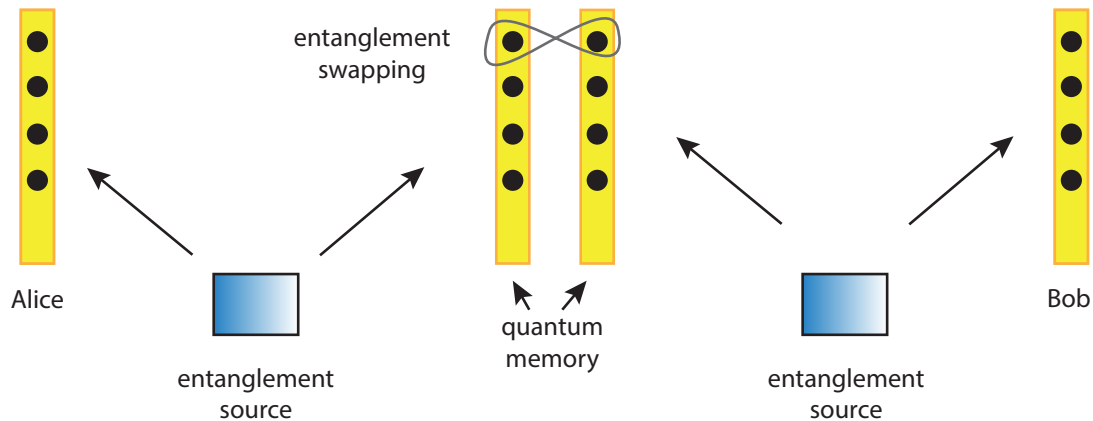


Figure 1.1: Principle of an optical quantum network. A quantum network, which links the two distant parties Alice and Bob, consists of one (or more) quantum repeaters in order to overcome loss that would otherwise destroy a quantum state. Within a quantum repeater the quantum state is stored in a quantum memory. Two quantum memories can be entangled via entanglement swapping, to create a connection in the network. The distance can be enlarged by more stages.

have the property that they are sensitive to optical loss. Even though telecommunication fibers have low attenuation at 1550 nm of about 0.17 dB/km [Li08], for long distances quantum repeaters are necessary to transfer the quantum states [Bri98, Dua01, Chi06, Cho08, San11]. Quantum repeaters can establish entanglement between two distant parties, usually called Alice and Bob, by connecting intermediate nodes of a quantum network via entanglement swapping [Žu93, Jia04]. Without quantum memories the success probability scales exponentially with n , where n is the number of stages within the quantum network. When quantum memories are used the scaling is proportional to n . A quantum memory stores the quantum states [Koz00, Jul04] until they get released on demand [Lou00]. Together with subsequent purification [Ben96] and distillation protocols [Fiu07, Hag08, Don08] a quantum network is established. This principle is also depicted in Fig. 1.1.

Quantum memories can be realized at different wavelengths corresponding to atomic transitions, and work mostly in the regime of 500–900 nm [Tit09]. Since for an efficient transmission of the quantum states the telecommunication wavelength of 1550 nm is preferred, quantum networks require a transfer between different wavelength regimes. Such a transfer was recently realized with photonic crystal fibers [McG10] and via four wave-mixing [Mej12]. Another possibility is to use quantum frequency conversion, which is demonstrated in this thesis. Since quantum memories have to store highly non-classical states, such as squeezed or entangled states [App08, Cho08, Hon08, Sag11], highly efficient frequency transitions which maintain

the quantum properties are mandatory [Chr13].

Even without a quantum memory, frequency conversion from the telecommunication wavelength to the visible wavelength regime provides the possibility of a highly efficient quantum state detection, since commercially available single photon counters are most efficient in the visible wavelength regime [Kam08, Pel12]. Recently, frequency conversion from the visible to the telecommunication wavelength regime has been realized [Iku12, FG13]. Within this thesis the reverse process will be demonstrated: on the one hand the experimental realization of frequency up-conversion of a squeezed state from 1550 nm to 532 nm will be shown and on the other hand the generation of entanglement between 1550 nm and 532 nm will be presented. These experiments show that the quantum properties are maintained in the process of frequency up-conversion via sum-frequency generation, as it was proposed by Prem Kumar [Kum90].

For future quantum networks multimode entanglement also plays an important role. It can exhibit more complex properties and features than two-mode entanglement. Therefore, multimode entanglement represents a valuable resource for lots of applications ranging from local realism tests [Zha03] to one-way quantum computing [Rau01, Wal05, Uka11]. For the quantum engineering of future networks we have to understand the special properties of multimode entanglement. Therefore, we have to think about new possibilities to generate entanglement between two distant parties. Proposed by Cubitt et al. [Cub03] the distribution of entanglement by separable states is experimentally realized within this thesis. This protocol, which seems to be counterintuitive at the first glance, is made possible by a specific three-mode state. Its special properties will be analyzed in detail to reveal the underlying structure of the protocol.

1.2 Quantum Spectroscopy and Imaging

Recently, Taylor *et al.* performed microrheology experiments and tracked lipid granules utilizing squeezed vacuum states of light [Tay13]. These states do not have a carrier field which would damage the sample. In addition, the special noise properties of squeezed vacuum states make measurements beyond the standard quantum limit possible. Therefore, they are highly suitable for quantum spectroscopy and quantum imaging [Tre03, Bra07, Bri10].

For applications like probing biological samples, the squeezed vacuum state would ideally be in the visible wavelength regime, to take advantage of higher detection efficiency, and its wavelength should match the probe's spectral transitions. Using convenient methods like parametric down-conversion, these states can be generated

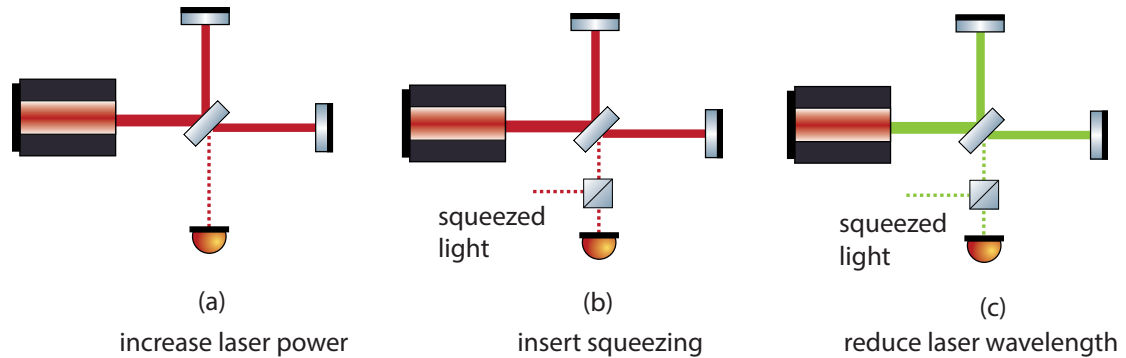


Figure 1.2: Methods to improve the sensitivity of a Michelson interferometer.

with high efficiency in the infrared wavelength regime [Ebe10, Meh11, Ste13]. For shorter wavelengths this technique is not applicable as ultra-violet light, which is required as a pump field, has a high absorption coefficient for nonlinear crystals [Koe06]. Squeezing via second harmonic generation [Tsu95] and self-phase modulation [Ber91] are further squeezing generation schemes. However, they can only generate squeezed states with a carrier field, which would damage the probe in quantum imaging.

In this thesis the technique of frequency conversion via sum-frequency generation was used to generate squeezed vacuum states of light at 532 nm.

1.3 Quantum Metrology

The improvement of gravitational wave detectors was the original motivation for generating strong squeezed vacuum states of light [Cav81]. Gravitational wave detectors use a Michelson interferometer as a measurement device, whose shot noise linear spectral density reads $\sqrt{S} = e^{-r} \sqrt{\hbar c \lambda / (2\pi P)}$, where P is the light power inside the interferometer, r is the squeezing factor and λ is the wavelength of the laser. That means that a Michelson interferometer can principally be improved by three methods: a) increasing the laser power, b) injecting squeezed light into the dark port of the interferometer, and c) decreasing the wavelength of the laser. These methods are illustrated in Fig. 1.2. The laser power cannot be increased indefinitely, as each component within the interferometer has to cope with the high laser power. This is especially true in the case of the beam splitter and the cavity mirrors, which encounter multiples of the initial laser power, since the cavity increases the optical power even further by interference effects. If the sensitivity of the interferometer should be improved by reducing the laser wavelength, squeezing should also be implemented to gain the best spectral density. First attempts to increase the detector

sensitivity by using shorter wavelengths are made in the design study for the future Japanese space antenna *DECIGO*[Kaw11], which shall operate in the visible region at a laser wavelength of 532 nm. As gravitational wave detectors based on a laser interferometer are shot noise limited in the kHz-regime [The11, Gro13], squeezed *vacuum* states of light are required. In this thesis the technique of frequency up-conversion is presented to also generate squeezed vacuum states of light at shorter wavelengths. It is currently the only known technique to obtain these states without any carrier field.

1.4 Structure of the Thesis

This thesis is structured as follows:

- Chapter 2 gives an introduction to the theory of non-classical states of light. The quantization of the electro-magnetic field and its description is presented and prominent examples of quantum states like squeezed and entangled states are given.
- Chapter 3 describes the nonlinear processes which underlie the presented experiments, such as sum-frequency generation, difference frequency generation and optical parametric amplification.
- Chapter 4 explains some of the basic techniques used for conducting the experiments, like squeezing generation, homodyne detection, single sideband locking scheme, and thermal state generation.
- Chapter 5 presents the experimental realization of quantum up-conversion. With this technique a squeezed state at 532 nm is generated and entanglement between 1550 nm and 532 nm is established.
- Chapter 6 shows the experimental entanglement distribution by separable states and the requirements for the underlying protocol.
- Chapter 7 summarizes this thesis.

Theory of Non-Classical States of Light

2.1 Quantization of the Electro-Magnetic Field

Quantum states of light show some nonintuitive behavior, which cannot be explained by a classical description. Therefore, we need a quantum description of the electromagnetic field. The derivation of this quantization can be found e.g. in [Ger10]. The quantized electric field operator of an N -mode free space radiation field at the position \mathbf{r} and time t is thereby described by

$$\hat{\mathbf{E}}(\mathbf{r}, t) = i \sum_{k=1}^N \left(\frac{\hbar}{2\omega_k \epsilon_0 V} \right)^{\frac{1}{2}} \mathbf{e}_k \left[\hat{a}_k e^{i(\mathbf{k}\mathbf{r} - \omega_k t)} + \hat{a}_k^\dagger e^{-i(\mathbf{k}\mathbf{r} - \omega_k t)} \right], \quad (2.1)$$

where \hbar is the reduced Planck constant $h/2\pi$, ω_k the angular frequency of the k th mode, \mathbf{e}_k the polarization vector, V an arbitrary volume, and \mathbf{k} the wave vector of the k th mode. The bosonic annihilation and creation operators of the k th mode \hat{a}_k and \hat{a}_k^\dagger are defined as

$$\begin{aligned} \hat{a}_k &= \frac{1}{(2\hbar\omega_k)^{1/2}} [\omega_k \hat{q}_k + i\hat{p}_k], \\ \hat{a}_k^\dagger &= \frac{1}{(2\hbar\omega_k)^{1/2}} [\omega_k \hat{q}_k - i\hat{p}_k], \end{aligned} \quad (2.2)$$

with \hat{p}_k, \hat{q}_k being the canonical position and momentum operator, respectively. They satisfy the bosonic commutation rule $[\hat{a}_k, \hat{a}_{k'}^\dagger] = \delta_{kk'}$. The energy of the electromagnetic field can be expressed in terms of these creation and annihilation operators,

by the Hamiltonian:

$$\begin{aligned}\hat{H} &= \sum_{k=1}^N \hbar\omega_k \left(\hat{a}_k^\dagger \hat{a}_k + \frac{1}{2} \right) \\ &= \sum_{k=1}^N \hbar\omega_k \left(\hat{n}_k + \frac{1}{2} \right),\end{aligned}\tag{2.3}$$

where

$$\hat{n}_k = \hat{a}_k^\dagger \hat{a}_k\tag{2.4}$$

represents the photon number operator of the k th mode. Thus, the energy of the electro-magnetic field can be calculated by the number of photons in each mode multiplied by the energy of a photon in that mode, plus $\frac{1}{2}\hbar\omega_k$, which corresponds to the energy of the vacuum fluctuations in each mode. These vacuum fluctuations are one of the special properties of quantum mechanics and are, e.g., responsible for the spontaneous emission that is the basic mechanism underlying lasing processes.

2.2 Quadrature Operators

To describe the quantized field and its states with Hermitian operators (i.e. observables) we introduce the quadrature operators

$$\begin{aligned}\hat{X}_k &= \hat{a}_k^\dagger + \hat{a}_k, \\ \hat{P}_k &= i(\hat{a}_k^\dagger - \hat{a}_k),\end{aligned}\tag{2.5}$$

satisfying the commutation relation [Wal10]

$$\left[\hat{X}_k, \hat{P}_k \right] = 2i.\tag{2.6}$$

Using this relation, it can be shown that the Heisenberg uncertainty relation [Ger10] for quadrature operators reads

$$\text{Var}(\hat{X}) \text{Var}(\hat{P}) \geq 1,\tag{2.7}$$

where $\text{Var}(\hat{A}) = \langle \hat{A}^2 \rangle - \langle \hat{A} \rangle^2$ is the variance of an operator \hat{A} . The mean $\langle \hat{A} \rangle$ of \hat{A} can be defined with the help of the density operator, which will be introduced in the following section.

The quadrature operators have eigenstates $|X_k\rangle$ and $|P_k\rangle$, which are called *quadrature*

ture states [Leo08],

$$\begin{aligned}\hat{X}_k|X_k\rangle &= X_k|X_k\rangle, \\ \hat{P}_k|P_k\rangle &= P_k|P_k\rangle,\end{aligned}\tag{2.8}$$

with continuous eigenvalues $X_k, P_k \in \mathbb{R}$. These quadrature states are orthonormal

$$\langle X_k|X'_k\rangle = \delta(X_k - X'_k), \quad \langle P_k|P'_k\rangle = \delta(P_k - P'_k)\tag{2.9}$$

and complete

$$\int |X_k\rangle\langle X_k|dX_k = \int |P_k\rangle\langle P_k|dP_k = 1.\tag{2.10}$$

2.3 Density Operator

A quantum system is fully described by its density operator [Ger10]

$$\hat{\rho} = \sum_i p_i |\Psi_i\rangle\langle\Psi_i|\tag{2.11}$$

on a Hilbert space \mathcal{H} , where p_i is the probability of finding the system in the state $|\Psi_i\rangle$ with $\sum_i p_i = \text{Tr } \hat{\rho} = 1$. For pure states $\text{Tr } \hat{\rho} = \text{Tr } \hat{\rho}^2 = 1$, while for mixed states $\text{Tr } \hat{\rho}^2 \leq 1$. $\text{Tr } \hat{\rho}^2$ is called the *purity* of a quantum system. Since all eigenvalues of the density operator are real and positive ($\hat{\rho} \geq 0$), the density operator is positive semi-definite.

With the density operator we can calculate the mean of an operator \hat{A} , as this value must be the average of all expectation values $\langle\Psi_i|\hat{A}|\Psi_i\rangle$ for each state $|\Psi_i\rangle$ weighted with the probability p_i of the system being in the state $|\Psi_i\rangle$ [Leo08]

$$\begin{aligned}\langle\hat{A}\rangle &= \sum_i p_i \langle\Psi_i|\hat{A}|\Psi_i\rangle \\ &= \text{Tr } \hat{\rho}\hat{A}.\end{aligned}\tag{2.12}$$

2.4 Wigner Function

Any density operator as a description of a quantum system has a phase space representation. One example of such a representation is the Wigner function, introduced by Eugene Wigner in 1932 [Wig32], which is a quasi probability distribution.

For one mode, the Wigner function for a phase space distribution reads

$$W(X, P) = \frac{1}{2\pi\hbar} \int \exp\left(\frac{iPx}{\hbar}\right) \left\langle X - \frac{x}{2} \left| \hat{\rho} \right| X + \frac{x}{2} \right\rangle dx\tag{2.13}$$

[Sch01]. The Wigner function is normalized

$$\int \int W(X, P) dX dP = 1$$

and for Hermitian operators $\hat{\rho}$ it is real

$$W^*(X, P) = W(X, P). \quad (2.14)$$

The marginal distributions

$$\begin{aligned} \int W(X, P) dP &= \langle X | \hat{\rho} | X \rangle, \\ \int W(X, P) dX &= \langle P | \hat{\rho} | P \rangle, \end{aligned} \quad (2.15)$$

retrieved by a projection of the Wigner function onto one of the quadrature axes, give us the amplitude and phase probabilities, respectively.

The Wigner function can also have negative values. It is from this reason that it is called a quasiprobability distribution. For Gaussian states, which are used throughout this thesis, the distribution will be positive everywhere.

With the help of the Wigner function we can illustrate states of light and easily show their special properties in phase space. Some of these special properties will be discussed in the following sections.

2.5 Fock States

One possible basis to describe quantum states of lights are the so called *Fock states*, named after V. A. Fock. Since they are defined as the eigenstates $|n_k\rangle$ of the photon-number operator \hat{n}_k (Eq. 2.4)

$$\hat{n}_k |n_k\rangle = n_k |n_k\rangle, \quad (2.16)$$

Fock states have a perfectly defined photon number, but a completely undefined phase. With the fundamental relations

$$\begin{aligned} \hat{a}_k |n_k\rangle &= \sqrt{n_k} |n_k - 1\rangle, \\ \hat{a}_k^\dagger |n_k\rangle &= \sqrt{n_k + 1} |n_k + 1\rangle, \end{aligned} \quad (2.17)$$

it becomes clear why \hat{a}_k and \hat{a}_k^\dagger are called the annihilation and creation operator, respectively – \hat{a}_k annihilates a photon from the k th mode of the field, while \hat{a}_k^\dagger

creates a photon in this mode. A Fock state can be obtained by applying the creation operator n_k times to the vacuum state $|0\rangle$

$$|n_k\rangle = \frac{\hat{a}_k^{\dagger n_k}}{\sqrt{n_k!}}|0\rangle. \quad (2.18)$$

The vacuum state $|0\rangle$ has a number of special properties: it contains zero photons (i.e. the mean photon number is zero) but its variances $\text{Var}(\hat{X})_0 = \text{Var}(\hat{P})_0 = 1$, thus minimizing Heisenberg's uncertainty relation. This is the reason why states that minimize the Heisenberg uncertainty relation are called *vacuum noise limited*. The Wigner function of a vacuum state can be found in Fig. 2.1 (a).

A notable consequence of vacuum fluctuations is that they couple into quantum optic experiments, whenever there are open ports or optical loss, and therefore have to be taken into account. One can see this e.g. in Subsection 2.9.2, where the generation of entanglement by overlapping a vacuum state with a squeezed state (cf. Sec. 2.7) at a beam splitter is derived.

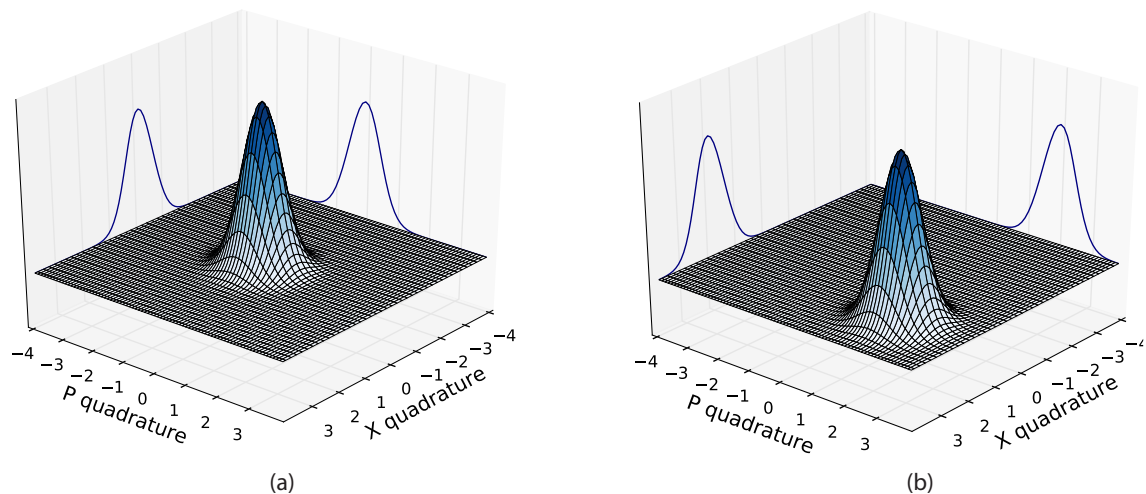


Figure 2.1: Wigner functions and their marginal distribution of (a) a vacuum state, and (b) a coherent state. The figure illustrates the fact that a coherent states are displaced vacuum states.

2.6 Coherent States

Another concept for describing quantum states are the *coherent states* as eigenstates of the annihilation operator \hat{a}_k

$$\hat{a}|\alpha\rangle = \alpha|\alpha\rangle. \quad (2.19)$$

They were introduced by R. J. Glauber [Gla63] and are composed by a vacuum state, which is displaced by a coherent amplitude α in phase space. Therefore, we introduce the displacement operator [Leo08]

$$\hat{D}(\alpha) = e^{\alpha\hat{a}_k^\dagger - \alpha^*\hat{a}_k}, \quad (2.20)$$

which creates a coherent state, when it is applied to a vacuum state

$$|\alpha\rangle = \hat{D}(\alpha)|0\rangle. \quad (2.21)$$

Coherent states also minimize Heisenberg's uncertainty relation, i.e. $\text{Var}(\hat{X}) = \text{Var}(\hat{P}) = 1$. In the Fock basis coherent states are defined as

$$\begin{aligned} |\alpha\rangle &= e^{-\frac{1}{2}|\alpha|^2} \sum_{n=0}^{\infty} \frac{\alpha^n}{\sqrt{n!}} |n\rangle \\ &= e^{-\frac{1}{2}|\alpha|^2} \sum_{n=0}^{\infty} \frac{\alpha^n}{n!} (\hat{a}^\dagger)^n |0\rangle, \end{aligned} \quad (2.22)$$

and have a Poissonian photon statistic

$$P_n = |\langle n|\alpha\rangle|^2 = e^{-|\alpha|^2} \frac{|\alpha|^{2n}}{n!}. \quad (2.23)$$

The Wigner function for a coherent state $|\alpha\rangle = |\frac{1}{2}(x + ip)\rangle$ is

$$W(X, P) = \frac{1}{2\pi} \exp\left(-\frac{(X-x)^2}{2} - \frac{(P-p)^2}{2}\right). \quad (2.24)$$

Figure 2.1 shows the Wigner functions of a vacuum state and a coherent state, which illustrates again that coherent states are displaced vacuum states. Besides the Wigner function the probability distributions of the X and P quadratures are depicted by projecting the Wigner function onto the respective quadrature.

2.7 Squeezed States

As we have already seen, vacuum states and coherent states are minimum uncertainty states according to Heisenberg's Uncertainty Principle. Moreover, their fluctuations are equally distributed in all quadratures. In contrast to this, the noise of *squeezed states* drops below the vacuum noise in one quadrature, while it is larger in the orthogonal quadrature to fulfill Heisenberg's Uncertainty Principle. We introduce the squeezing operator [Ger10]

$$\hat{S} = \exp \left[\frac{\xi}{2} (\hat{a}^2 - \hat{a}^{\dagger 2}) \right], \quad (2.25)$$

where $\xi = r e^{i\phi}$ with the squeezing parameter $r \geq 0$ and the squeezed quadrature angle $0 \leq \phi \leq 2\pi$. With an increasing squeezing parameter r , the variance in the squeezed quadrature becomes less, while the corresponding variance in the orthogonal quadrature increases. The variances of an amplitude-squeezed state ($\phi = 0$) read

$$\begin{aligned} \text{Var}(\hat{X}) &= e^{-2r} < 1, \\ \text{Var}(\hat{P}) &= e^{2r} > 1. \end{aligned} \quad (2.26)$$

Thus, the corresponding noise distribution becomes an ellipse in phase space.

We obtain a squeezed vacuum state by applying the squeezing operator to a vacuum state

$$|\Psi\rangle = \hat{S}(\xi)|0\rangle \quad (2.27)$$

and a displaced squeezed vacuum state by additionally applying the displacement operator cf. 2.20

$$|\Psi\rangle = \hat{D}(\alpha)\hat{S}(\xi)|0\rangle. \quad (2.28)$$

Throughout this thesis we will deal with squeezed vacuum states of light.

A special property of squeezed states is that photons are only generated in pairs. This behavior can be seen in the photon number statistic [Leo08]

$$P_n = \begin{cases} \binom{n}{n/2} \frac{1}{\cosh(r)} \left(\frac{1}{2} \tanh(r)\right)^n, & \text{for } n \text{ even} \\ 0, & \text{for } n \text{ uneven.} \end{cases} \quad (2.29)$$

It can also be shown that these photon pairs are entangled [Hag10b].

The Wigner function for a squeezed state is given by

$$W(X, P) = \frac{1}{2\pi} \exp \left(-\frac{(X-x)^2}{2} e^{2r} - \frac{(P-p)^2}{2} e^{-2r} \right). \quad (2.30)$$

Fig. 2.2 depicts this Wigner function and its marginal distributions.

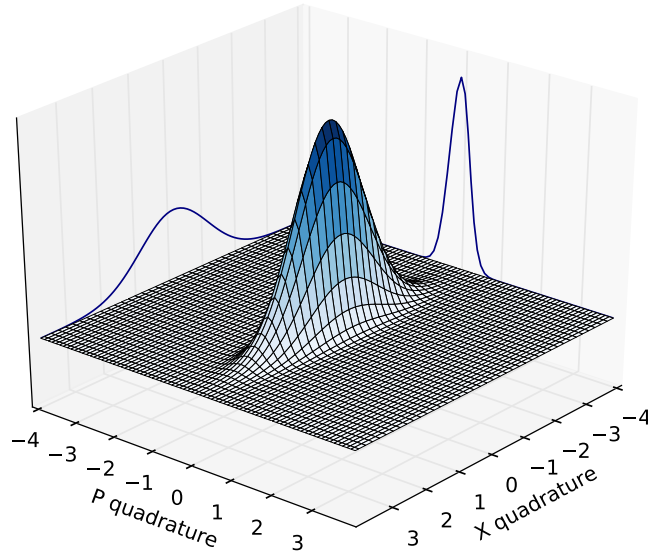


Figure 2.2: Wigner function and its marginal distributions of a squeezed vacuum state. In the P quadrature the noise drops below the vacuum noise, while in the X quadrature the noise increases.

2.7.1 Squeezed States and Optical Loss

The influence of loss on squeezed states of light is crucial in all experiments accomplished for this thesis, since optical loss introduces vacuum noise and thus decrease the squeezing degree. On the one hand we want reduce optical loss as much as possible to measure highly squeezed states of light and on the other hand a specific amount of loss is required to implement the protocol for distributing entanglement by separable states. Therefore, we will have a closer look on the influence of optical loss on squeezing in this subsection.

The optical loss l which a squeezed light field a_{sqz} experiences in an optical setup can be represented by an additional beam splitter with amplitude reflectivity \sqrt{l} and transmissivity $\sqrt{1-l}$. The resulting field (here: the outgoing field) is given by

$$\hat{a}_1 = \sqrt{1-l}\hat{a}_{\text{sqz}} + \sqrt{l}\hat{a}_{\text{vac}}, \quad (2.31)$$

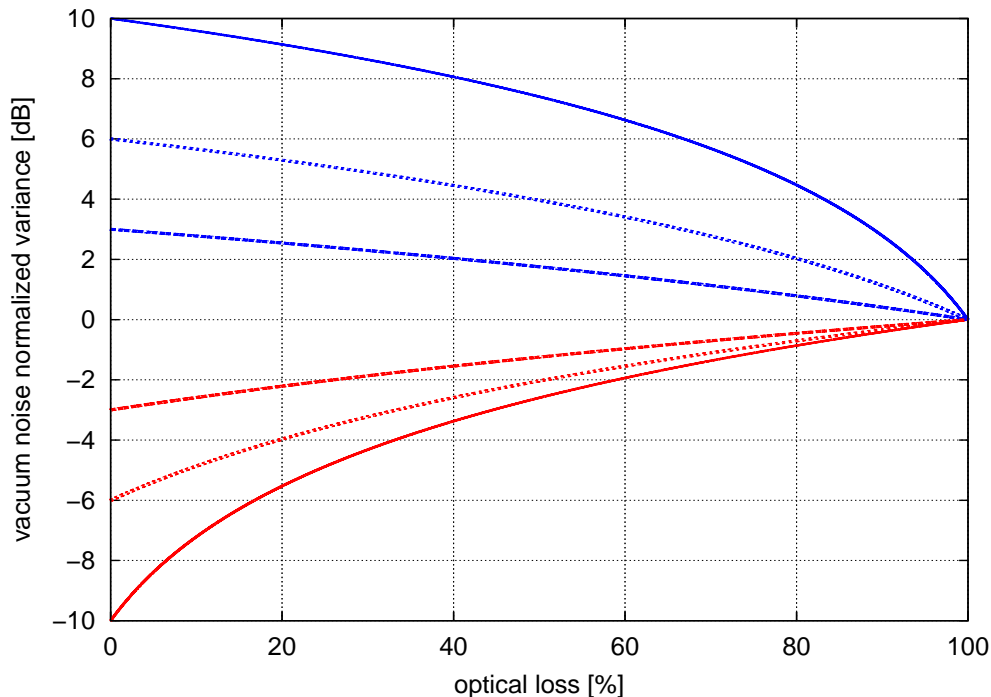


Figure 2.3: Influence of optical loss on the squeezing strength. For 3 dB (dashed lines), 6 dB (dotted lines), and 10 dB (solid lines) initial squeezing the influence of optical loss is depicted. Squeezing (red) and anti-squeezing (blue) strengths are affected differently by optical loss. For more than 50% loss the squeezing strength cannot exceed -3 dB.

where \hat{a}_{vac} denotes the vacuum input. Thus, the variance of an arbitrary quadrature reads

$$\text{Var}(\hat{X}_1(\vartheta)) = (1 - l) \text{Var}(\hat{X}_{\text{sqz}}(\vartheta)) + l \text{Var}(\hat{X}_{\text{vac}}). \quad (2.32)$$

In Fig. 2.3 the influence of optical loss on the squeezing strength is illustrated, where we used the convenient logarithmic scale for the variances via the relation

$$\text{Var}_{\text{dB}} = 10 \log_{10}(\text{Var}). \quad (2.33)$$

The figure shows that the squeezed quadrature is much more influenced by optical loss than the anti-squeezed quadrature. Furthermore, it depicts the fact that with an optical loss of more than 50% the squeezing strength cannot exceed -3 dB.

2.8 The Class of Gaussian States

Throughout this thesis we will deal with Gaussian states of light, i.e. states of light that we can describe by continuous variables (CV) with Gaussian statistics. The

Wigner function of Gaussian states is completely determined by the second order covariance matrix V . To describe this matrix, we introduce the $2N$ -dimensional vector of quadratures $\hat{\gamma} = (\hat{X}_1, \hat{P}_1, \dots, \hat{X}_N, \hat{P}_N)^T$ and can therefore express the canonical commutation rule cf. Eq. 2.6 in the compact form

$$[\gamma_j, \gamma_k] = 2i\Omega_{jk} \quad (j, k = 1, 2, \dots, N) \quad (2.34)$$

with

$$\Omega = \bigoplus_{i=1}^N J = \begin{pmatrix} J & & \\ & \ddots & \\ & & J \end{pmatrix}, \quad J = \begin{pmatrix} 0 & 1 \\ -1 & 0 \end{pmatrix} \quad (2.35)$$

as the symplectic matrix. With the quadrature vector γ the element V_{jk} of the covariance matrix V is defined by

$$\begin{aligned} V_{jk} &= \frac{1}{2} \langle \Delta \hat{\gamma}_j \Delta \hat{\gamma}_k + \Delta \hat{\gamma}_k \Delta \hat{\gamma}_j \rangle \\ &= \frac{1}{2} \langle \hat{\gamma}_j \hat{\gamma}_k + \hat{\gamma}_k \hat{\gamma}_j \rangle - \langle \hat{\gamma}_j \rangle \langle \hat{\gamma}_k \rangle, \end{aligned} \quad (2.36)$$

with $\Delta \hat{\gamma}_j = \hat{\gamma}_j - \langle \hat{\gamma}_j \rangle$. Note that the variances of the quadrature operators can be found as the diagonal elements of the covariance matrix, i.e. $V_{ii} = \text{Var}(\gamma_i)$. The covariance matrix is a $2N \times 2N$ real and symmetric matrix, which satisfies the uncertainty principle [Sim94]

$$V + i\Omega \geq 0. \quad (2.37)$$

This equation is equivalent to the property that all eigenvalues of the matrix are non-negative and thus, that the covariance matrix is positive definite $V > 0$.

2.9 Gaussian Entangled States

Entanglement was first considered by Einstein, Podolsky, and Rosen (EPR) in their famous paper about the completeness of quantum mechanics [Ein35]. They demonstrated, with the example of an entangled system, that the description of quantum mechanics cannot be complete if the concept of local realism holds. In Schrödinger's answer to this paper [Sch35] he introduced the term *entangled state* for a state that cannot be separated into factorized terms. Although Schrödinger did not believe in the local hidden variable theory suggested by EPR, he also could not believe in nonlocality. However, in 1964 Bell demonstrated [Bel64] that there are correlations of quantum states, which cannot be explained by any local hidden variable theory and thus the concept of local realism had to be dismissed. Since 1935 the term en-

tanglement has not lost its magic and its potential for fundamental discussions, but nowadays we understand entanglement more as a resource for quantum information rather than as a mystery.

Mathematically a system consisting of N modes is entangled, if the total density operator $\hat{\rho}$ cannot be written as a mixture of its product states [Wee12]

$$\hat{\rho} = \sum_i p_i \hat{\rho}_i^1 \otimes \dots \otimes \hat{\rho}_i^N, \quad (2.38)$$

with $\sum_i p_i = 1$. In the following we will introduce two more practical entanglement criteria, which can be easily applied to our experiments. In a next step it is shown how entanglement can be generated utilizing a squeezed vacuum state and a beam splitter.

2.9.1 Entanglement Criteria

Inseparability Criterion

A particular useful inseparability criterion was introduced by Duan *et al.* in the year 2000 [Dua00] and provides a sufficient criterion for entanglement of bipartite states in the continuous variable regime. For Gaussian states it is also a necessary condition for inseparability.

We follow the calculations in [Dua00] and consider a bipartite state consisting of the two modes A and B . We introduce the operators

$$\begin{aligned} \hat{U} &= |a| \hat{X}_A - \frac{1}{a} \hat{X}_B, \\ \hat{V} &= |a| \hat{P}_A + \frac{1}{a} \hat{P}_B, \end{aligned} \quad (2.39)$$

where $a \neq 0$ is a real arbitrary number. If the modes A and B experience the same amount of loss, $|a|$ is equal to 1, and it gets larger, if the amount of losses becomes different. Due to the inseparability criterion the modes A and B are entangled, if

$$\mathcal{I} = \text{Var}(\hat{U}) + \text{Var}(\hat{V}) \leq 2a^2 + \frac{2}{a^2}. \quad (2.40)$$

For $|a| = 1$, which is usually the case in the experiments of this thesis, this inequality reduces to

$$\begin{aligned} \mathcal{I} &= \text{Var}(\hat{U}) + \text{Var}(\hat{V}) \\ &= \text{Var}(X_A - X_B) + \text{Var}(P_A + P_B) \\ &\leq 4. \end{aligned} \quad (2.41)$$

When we want to refer to the inseparability criterion in the following, we will use the term *Duan value* for \mathcal{I} . This criterion is somehow intuitive, since it is directly obvious that when vacuum states are used for the two modes with completely uncorrelated noise, the Duan values equals the threshold 4.

PPT-criterion

If we want to investigate the entanglement properties of a state with more than two modes, we need another criterion. A. Peres and P. Horodecki introduced a criterion for separability [Per96, Hor97], which was proved by R. Simon to be necessary and sufficient for all bipartite Gaussian states [Sim00] and to be necessary and sufficient for states with $1 \times N$ modes by R. Werner and W. Wolf [Wer00]. Since we will check if a covariance matrix is still positive under partial transposition, this criterion is called *PPT-criterion* (sometimes it is also called Peres-Horodecki-criterion due to its original inventors). In the following we will restrict ourselves to the tripartite case with the quadrature vector $\boldsymbol{\xi} = (\hat{X}_A, \hat{P}_A, \hat{X}_B, \hat{P}_B, \hat{X}_C, \hat{P}_C)^T$, the covariance matrix V , and the bipartite splittings $A|BC$, $B|AC$, and $C|AB$.

In the continuous variable regime the partial transpose corresponds to a mirror reflection in the Wigner phase space [Sim00] or, equivalently, to the transformation that changes the sign of the i th mode's P coordinate [Gie01, Miš09]

$$V \mapsto V^{(T_i)} = R_i V R_i^T \quad i = A, B, C \quad (2.42)$$

with the diagonal matrices $R_A = \sigma_z \oplus \mathbb{1} \oplus \mathbb{1}$, $R_B = \mathbb{1} \oplus \sigma_z \oplus \mathbb{1}$, and $R_C = \mathbb{1} \oplus \mathbb{1} \oplus \sigma_z$, where σ_z is the Pauli diagonal matrix $\sigma_z = \text{diag}(1, -1)$. To check if a state is separable, the new matrix $V^{(T_i)}$ has to fulfill Eq. 2.37

$$V^{(T_i)} + i\Omega \geq 0. \quad (2.43)$$

However, if the lowest eigenvalue is negative, the state is inseparable or entangled with respect to the $i|jk$ splitting ($i, j, k \in A, B, C$).

Instead of the procedure described above, we can also investigate the symplectic eigenvalues of the covariance matrix to check if the state is separable or inseparable. We take advantage of the fact, that for any partial transposed matrix $V^{(T_i)}$ there is a real, symplectic 6×6 matrix S , satisfying $S\Omega S^T = \Omega$ and introducing the diagonal form

$$S V^{(T_i)} S^T = \text{diag}(s_A, s_A, s_B, s_B, s_C, s_C) \quad (2.44)$$

with the symplectic eigenvalues s_i , $i \in A, B, C$. With this symplectic matrix we can say, that a state is separable with respect to the $i|jk$ splitting, if and only if $s_i \geq 1 \quad \forall i$. Further information for this symplectic transposition can be found in

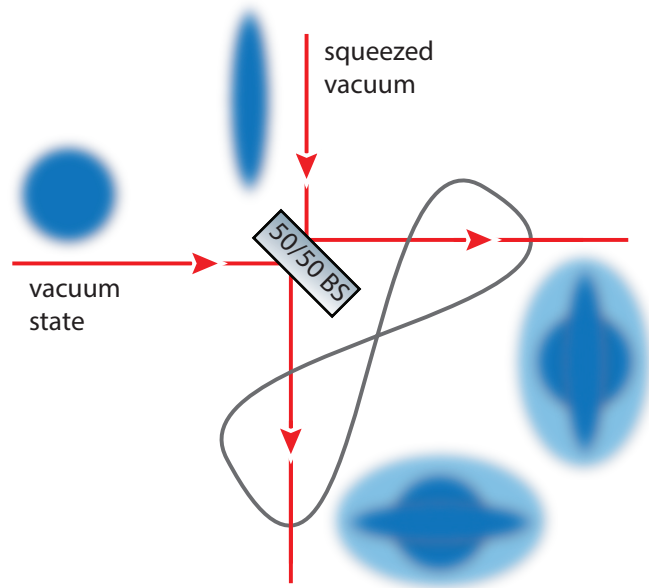


Figure 2.4: Entanglement generation with a squeezed vacuum state and a vacuum state at a balanced beam splitter (BS). The blue blurred shapes illustrate the noise of the input states (squeezed vacuum and vacuum state). After the superposition at the balanced beam splitter, the noise of resulting modes (light blue) is composed of the noise of the two input states.

[Miš09, Vid01]. Within this thesis we will call the lowest symplectic eigenvalue the *PPT value*, to have a measure for the inseparability of a certain state.

2.9.2 Generation of Gaussian Entanglement

Entanglement can be generated in several ways, e.g. in optical parametric oscillators operated below or above threshold. In such a device one photon decays into two photons, which are called *signal* and *idler* due to historical reasons. These two outgoing photons are entangled, since they are generated simultaneously and have to conserve energy and momentum. Experiments demonstrating this kind of entanglement generation can be found in [Kwi99, Vil05, Sam11] for entanglement in optical parametric oscillators above threshold and in [Ou92, Bou97, How04] for entanglement in optical parametric amplifiers below the threshold.

In contrast to these experiments, in this thesis we generated entanglement by sending a squeezed state at a balanced beam splitter, whose two output modes are then entangled. This kind of entanglement generation will be investigated in the following subsection.

Figure 2.4 shows the principle of the entanglement generation with a squeezed

state and a beam splitter. Since we use a vacuum state as a second input of the beam splitter, this kind of entanglement is called *v-class* entanglement, in contrast to the scheme utilizing two squeezed states overlapped at a beam splitter, which is called *s-class* entanglement [DiG07] and is demonstrated e.g. in [Fur98, Bow03, Ste13].

The covariance matrix of the total system before the beam splitter can be written as

$$V = \begin{pmatrix} V_1 & 0 \\ 0 & V_2 \end{pmatrix} = \begin{pmatrix} e^{-2r} & 0 & 0 & 0 \\ 0 & e^{2r} & 0 & 0 \\ 0 & 0 & 1 & 0 \\ 0 & 0 & 0 & 1 \end{pmatrix}, \quad (2.45)$$

where r denotes the squeezing parameter of the squeezed mode. It is obvious from the Duan criterion that this two mode state is separable, since

$$\begin{aligned} \mathcal{I} &= \text{Var}(X_1 - X_2) + \text{Var}(P_1 + P_2) \\ &= \underbrace{e^{-2r} + e^{2r}}_{\geq 2} + 2 \geq 4. \end{aligned} \quad (2.46)$$

The beam splitter transformation for a two mode system is given by [Wee12]

$$S_{\text{BS}}(\tau) = \begin{pmatrix} \sqrt{\tau} & 0 & \sqrt{1-\tau} & 0 \\ 0 & \sqrt{\tau} & 0 & \sqrt{1-\tau} \\ -\sqrt{1-\tau} & 0 & \sqrt{\tau} & 0 \\ 0 & -\sqrt{1-\tau} & 0 & \sqrt{\tau} \end{pmatrix}, \quad (2.47)$$

where $\tau \in [0, 1]$ denotes the beam splitter's power transmissivity. We restrict ourselves to the case of a balanced beam splitter with $\tau = 1/2$. If we apply this beam splitter matrix to the covariance matrix, we get the new covariance matrix for the two modes behind the balanced beam splitter

$$\begin{aligned} V_{\text{BS}} &= S_{\text{BS}}(1/2) V S_{\text{BS}}(1/2)^T \\ &= \begin{pmatrix} \frac{1}{2}(1 + e^{-2r}) & 0 & \frac{1}{2}(1 - e^{-2r}) & 0 \\ 0 & \frac{1}{2}(1 + e^{2r}) & 0 & \frac{1}{2}(1 - e^{2r}) \\ \frac{1}{2}(1 - e^{-2r}) & 0 & \frac{1}{2}(1 + e^{-2r}) & 0 \\ 0 & \frac{1}{2}(1 - e^{2r}) & 0 & \frac{1}{2}(1 + e^{+2r}) \end{pmatrix}. \end{aligned} \quad (2.48)$$

For an overlap of a squeezed vacuum state and a vacuum at a balanced beam splitter and without considering any loss, the Duan value for the two-mode state

behind the beam splitter reads

$$\begin{aligned}\mathcal{I} &= \text{Var}(X'_1 - X'_2) + \text{Var}(P'_1 + P'_2) \\ &= \text{Var } X_1 + \text{Var } X_2 - 2\text{Cov}(X_1 X_2) + \text{Var } P_1 + \text{Var } P_2 + 2\text{Cov}(P_1 P_2) \quad (2.49) \\ &= 2(e^{-2r} + 1) < 4 \quad \text{for } r > 0,\end{aligned}$$

where $\text{Cov}(xy)$ denotes the covariance of x and y , which is defined by the covariance matrix V_{ik} (Eq. 2.36). Equation 2.49 shows that the two-mode state behind the beam splitter is always entangled, if a squeezed and a vacuum state are used as the two input states.

Nonlinear Processes

Nonlinear optical processes are the basis for all experiments demonstrated within this thesis, since only these processes can transform classical states of light into non-classical states of light. They occur when materials show special properties due to the presence of intense light. Usually only laser light has sufficient power for starting nonlinear processes. With an intense laser field the polarization of a medium can develop new frequencies, which can act as sources for new frequency components of the electro-magnetic field. Such nonlinear behavior is for example responsible for second harmonic generation, which provides the pump field for the other nonlinear processes within the experiments conducted for this thesis.

In this chapter these nonlinear processes are described in detail. Prior to the description of specific nonlinear processes we will introduce some basic concepts of nonlinear optics. In Section 3.2 we start with the sum-frequency generation process for up-converting squeezed and entangled fields from 1550 nm to 532 nm utilizing a pump field at 810 nm (cf. Chapter 5). Its quantum description follows in Section 3.3. Section 3.4 deals with difference frequency generation and optical parametric oscillation for generating the twin beams at 1550 nm and 810 nm. The quantum description of optical parametric amplification, which generates squeezed vacuum states of light for use in the entanglement distribution experiment (cf. Chapter 6) and the quantum up-conversion experiments (cf. Chapter 5), is given in Section 3.5. At the end of this chapter in Section 3.6 the principle of phase-matching and ways for achieving it are introduced.

3.1 Basic Concepts

In linear optics the dipole moment per unit volume, i.e. the polarization $P(t)$, is proportional to the strength $E(t)$ of an applied optical field linearly, and can be described by

$$\mathbf{P}^{(1)}(t) = \epsilon_0 \chi^{(1)} \mathbf{E}(t), \quad (3.1)$$

where $\chi^{(1)}$ denotes the linear susceptibility and ϵ_0 is the dielectric permittivity. If, however, the incident light power is sufficiently large, the polarization vector has to be expressed by a power series of the field strength $E(t)$ as

$$\begin{aligned} \mathbf{P}(t) &= \epsilon_0 [\chi^{(1)} \mathbf{E}(t) + \chi^{(2)} \mathbf{E}^2(t) + \chi^{(3)} \mathbf{E}^3(t) + \dots] \\ &= \mathbf{P}^{(1)}(t) + \mathbf{P}^{(\text{NL})}(t). \end{aligned} \quad (3.2)$$

Here, $\chi^{(2)}$ and $\chi^{(3)}$ are the second- and third-order susceptibility and typically on the order of 10^{-11} and 10^{-20} , respectively. All higher-order susceptibilities $\chi^{(N)}$ are even orders of magnitude smaller and do thus not play a role within the laser intensities we can achieve in our laboratories.

As soon as the response of the material due to an electric field is nonlinear, additional field components are generated. For the second-order nonlinear interaction this can be easily seen when a single-frequency field $E(t) = E_0 e^{-i\omega t} + \text{c. c.}$ is used. The second-order polarization then reads

$$P^{(2)} = 2\epsilon_0 \chi^{(2)} [E_0 E_0^* + E_0^2 e^{-2i\omega t}] + \text{c. c.}, \quad (3.3)$$

with c. c. denoting the complex conjugate, and is responsible for the generated field at twice the frequency. This process is called *Second Harmonic Generation* (SHG) and is used within for providing the pump field for two devices: the optical parametric oscillator, generating the 810 nm and 1550 nm field, and the optical parametric amplifier, generating squeezed states of light.

When more than one frequency is injected, the second-order interaction also leads to the generation of sum or difference frequencies. These processes will be derived in the next sections.

3.2 Sum-Frequency Generation in Classical Optics

Sum-frequency generation is at the heart of the quantum up-conversion experiment described in Chapter 5. There, a strong pump field at 810 nm is overlapped with

a squeezed field at 1550 nm, to generate a squeezed field at the sum-frequency corresponding to 532 nm. In the following we will calculate the solution for the wave equations of this process with exactly this boundary condition, that the pump field is strong and thus undepleted compared to the signal field. The section follows the calculation presented in [Boy08].

One can derive the optical wave equation by using Maxwell's equation in matter and assuming a medium without sources and free currents

$$\nabla^2 \mathbf{E} - \frac{1}{c^2} \frac{\partial^2 \mathbf{E}}{\partial t^2} = \frac{1}{\epsilon_0 c^2} \frac{\partial^2 \mathbf{P}}{\partial t^2}. \quad (3.4)$$

The wave equation can be simplified by assuming a lossless, dispersionless, isotropic medium

$$\nabla^2 \mathbf{E} - \frac{\epsilon^{(1)}}{c^2} \frac{\partial^2 \mathbf{E}}{\partial t^2} = \frac{1}{\epsilon_0 c^2} \frac{\partial^2 \mathbf{P}^{(\text{NL})}}{\partial t^2}, \quad (3.5)$$

where $\epsilon^{(1)} = 1 + \chi^{(1)}$ denotes the relative permittivity and $\mathbf{P}^{(\text{NL})}$ is the nonlinear polarization vector introduced in Eq. 3.2. However, most nonlinear media are dispersive. That is the reason why each frequency component ω_N with $N = 1, 2, \dots$ has to be treated separately to obtain the wave equation

$$\nabla^2 \mathbf{E}_N - \frac{\epsilon^{(1)}(\omega_N)}{c^2} \frac{\partial^2 \mathbf{E}_N}{\partial t^2} = \frac{1}{\epsilon_0 c^2} \frac{\partial^2 \mathbf{P}_N^{(\text{NL})}}{\partial t^2}, \quad (3.6)$$

where the right-hand side of the equation shows the nonlinear response of the medium, which acts as a source for new radiating frequencies. Equation 3.6 will now be used for deriving the sum-frequency generation.

Figure 3.1 shows the principle of the sum-frequency generation. Due to the nonlinear interaction a pump field at frequency ω_2 and a signal field at ω_1 generate a field at the sum frequency ω_3 . We assume monochromatic, continuous-wave input beams with an angle of incidence of zero degree. The solution for the sum-frequency component of Eq. 3.6 propagating in the z-direction is given by

$$E_3(z, t) = A_3(z) e^{i(k_3 z - \omega_3 t)} + \text{c. c.}, \quad (3.7)$$

with

$$k_3 = \frac{n_3 \omega_3}{c}, \quad n_3^2 = \epsilon^{(1)}(\omega_e), \quad (3.8)$$

and $A_3(z)$ is the amplitude of the field at ω_3 , where we assumed $A_3(z)$ to be a slowly varying function of z . This assumption is called the *slowly varying amplitude*

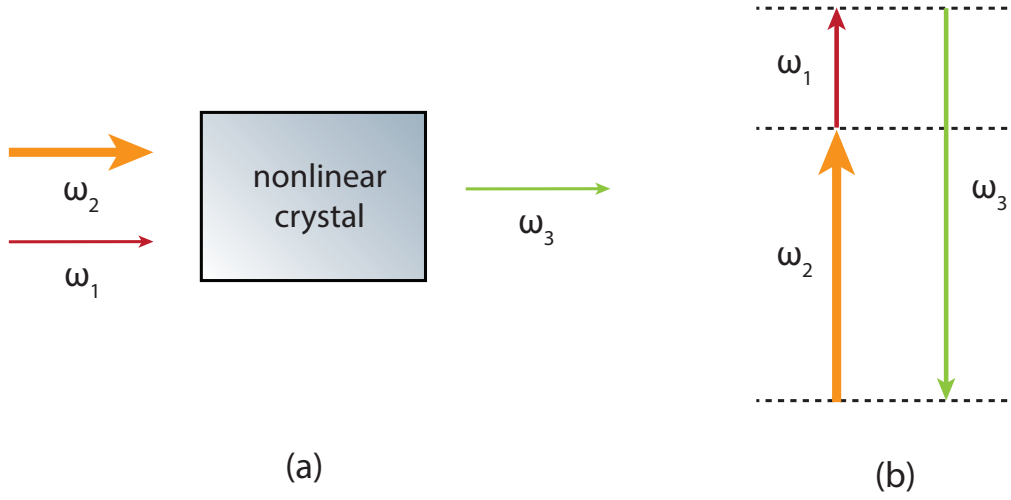


Figure 3.1: Principle of sum-frequency generation. (a) A strong pump field at frequency ω_2 interacts with a signal field at ω_1 in a nonlinear medium. This leads to the sum-frequency generation of $\omega_3 = \omega_1 + \omega_2$. (b) The corresponding energy level diagram.

approximation, and is valid whenever the inequality

$$\left| \frac{d^2 A_3}{dz^2} \right| \ll \left| k_3 \frac{dA_3}{dz} \right| \quad (3.9)$$

holds. Since we will use a strong pump field at ω_2 in comparison to the signal field at ω_1 , the amplitude A_2 is unaffected by the interaction and we can use A_2 as a constant. This leads us to the coupled-amplitude equations

$$\frac{dA_1}{dz} = K_1 A_3 e^{-i\Delta k z}, \quad (3.10a)$$

$$\frac{dA_3}{dz} = K_3 A_1 e^{i\Delta k z}, \quad (3.10b)$$

where we used

$$K_1 = \frac{2i\omega_1^2 d_{\text{eff}}}{k_1 c^2} A_2^*, \quad K_3 = \frac{2i\omega_3^2 d_{\text{eff}}}{k_3 c^2} A_2, \quad (3.11)$$

with the effective susceptibility $d_{\text{eff}} = \chi^{(2)}/2$ and the wave vector mismatch

$$\Delta k = k_1 + k_2 - k_3. \quad (3.12)$$

Since the frequencies ω_1 and ω_3 are coupled to each other, we expect them to display the same spatial variation, and assume the solution for the Eqs. 3.10a and 3.10b to

be of the form

$$A_1(z) = (Fe^{igz} + Ge^{-igz})e^{-i\Delta kz/2}, \quad (3.13a)$$

$$A_3(z) = (Ce^{igz} + De^{-igz})e^{i\Delta kz/2}, \quad (3.13b)$$

where the rate of the fields' spatial variation is denoted by g and the values of the constants C, D, F , and G depend on the boundary conditions. In order to find an appropriate expression for these constants, we substitute Eqs. 3.13a and 3.13b into Eq. 3.10a and obtain

$$\begin{aligned} (igFe^{igz} - igGe^{-igz})e^{-i\Delta kz/2} - \frac{1}{2}i\Delta k(Fe^{igz} + Ge^{-igz})e^{-i\Delta kz/2} \\ = (K_1Ce^{igz} + K_1De^{igz})e^{-i\Delta kz/2}. \end{aligned} \quad (3.14)$$

This equation has to hold for all values of z . Therefore, the terms of the equation depending on e^{igz} and e^{-igz} have to satisfy the equality separately, and their coefficients have to be related by

$$F\left(ig - \frac{1}{2}i\Delta k\right) = K_1C, \quad (3.15)$$

$$-G\left(ig + \frac{1}{2}i\Delta k\right) = K_1D. \quad (3.16)$$

Like before we substitute Eqs. 3.13a and 3.13b into Eq. 3.10b and obtain

$$\begin{aligned} (igCe^{igz} - igDe^{-igz})e^{i\Delta kz/2} + \frac{1}{2}i\Delta k(Ce^{igz} + De^{-igz})e^{i\Delta kz/2} \\ = (K_3Fe^{igz} + K_3Ge^{igz})e^{i\Delta kz/2}. \end{aligned} \quad (3.17)$$

The relation which the coefficients have to satisfy this time is given by

$$C\left(ig + \frac{1}{2}i\Delta k\right) = K_3F, \quad (3.18)$$

$$-D\left(ig - \frac{1}{2}i\Delta k\right) = K_3G. \quad (3.19)$$

With Eqs. 3.15 and 3.18 we obtain a condition for F and C in matrix form

$$\begin{pmatrix} i\left(g - \frac{1}{2}\Delta k\right) & -K_1 \\ -K_3 & i\left(g + \frac{1}{2}\Delta k\right) \end{pmatrix} \begin{pmatrix} F \\ C \end{pmatrix} = 0. \quad (3.20)$$

In order to solve this set of equations, the determinant of the matrix has to vanish,

i.e.

$$g = \sqrt{-K_1 K_3 + \frac{1}{4} \Delta k^2}. \quad (3.21)$$

For a final solution of the wave equations 3.10a and 3.10b for the sum-frequency generation we assume that the initial input fields $A_1(0)$ and $A_3(0)$ are known and we find with Eqs. 3.13a and 3.13b the additional relations for the coefficients

$$A_1(0) = F + G, \quad (3.22)$$

$$A_3(0) = C + D. \quad (3.23)$$

Now we have four and thus sufficient relations for the four coefficients $C, D, F,$ and $G,$ thus, we can give the solution for the wave equations by

$$A_1(z) = \left[A_1(0) \cos gz + \left(\frac{K_1}{g} A_3(0) + \frac{i\Delta k}{2g} A_1(0) \right) \sin gz \right] e^{-i\Delta kz/2}, \quad (3.24a)$$

$$A_3(z) = \left[A_3(0) \cos gz + \left(\frac{-i\Delta k}{2g} A_3(0) + \frac{K_3}{g} A_1(0) \right) \sin gz \right] e^{i\Delta kz/2}. \quad (3.24b)$$

Usually there is no sum-frequency field at the beginning of the process, i.e. $A_3(0) = 0$ and Eq. 3.24b reduces to

$$A_3(z) = \frac{K_3}{g} A_1(0) \sin gz e^{i\Delta kz/2}. \quad (3.25)$$

The intensity of the generated wave at ω_3 is then given by

$$|A_3(z)|^2 = |A_1(0)|^2 \frac{|K_3|^2}{g^2} \sin^2 gz. \quad (3.26)$$

It is important to note that with increasing $\Delta k,$ i.e. with increasing wave vector mismatch, the maximum intensity of the generated field is decreased and the oscillation frequency of the generation process is increased. This behavior is shown in Fig. 3.2, where the intensity of the generated sum-frequency field is depicted with respect to the length of the nonlinear medium for different $\Delta k.$ For a perfect wave vector matching ($\Delta k = 0$) the intensity reaches a maximum. After the maximum is reached at a certain penetration depth, the converted field is back-converted to the initial frequencies ω_1 and ω_2 until the whole field is back-converted and the conversion process starts again.

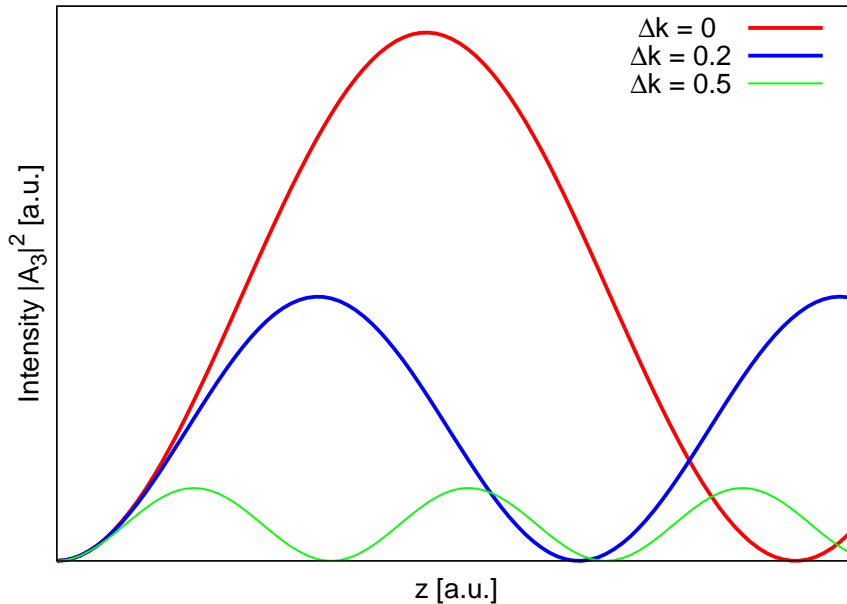


Figure 3.2: Spatial variation of the sum-frequency field. The intensity of the generated field is plotted versus the length of the nonlinear medium for different wave vector mismatches Δk . For increasing Δk the maximum intensity decreases and is reached earlier.

3.3 Quantum Up-Conversion via Sum-Frequency Generation

In the last section we treated the sum-frequency generation process in a classical manner. In the following section we will show that the sum-frequency generation process utilizing an undepleted pump field is highly suited for the up-conversion of quantum states, since the quantum properties of a weak signal field at ω_1 are maintained when the field is converted to a field at ω_3 . The presented calculations follow [Kum90].

We start our consideration of quantum sum-frequency generation with the Hamiltonian describing this process

$$\hat{H}_{\text{SFG}} = i\hbar\chi'(\hat{a}_1\hat{a}_2\hat{a}_3^\dagger - \hat{a}_1^\dagger\hat{a}_2^\dagger\hat{a}_3), \quad (3.27)$$

where \hbar denotes the reduced Planck constant and χ' is the coupling constant of the interaction and is proportional to the second-order susceptibility $\chi^{(2)}$ of the nonlinear material. Since we assume a strong and undepleted pump field at ω_2 the

Hamiltonian reduces to

$$\hat{H}_{\text{SFG}} = i\hbar\chi(\hat{a}_1\hat{a}_3^\dagger - \hat{a}_1^\dagger\hat{a}_3), \quad (3.28)$$

with $\chi = \chi'\langle\hat{a}_2\rangle$. The time evolution of this process can be obtained by using Heisenberg's equation of motion

$$\frac{d\hat{a}}{dt} = \frac{i}{\hbar} [\hat{H}, \hat{a}] + \frac{\partial\hat{a}}{\partial t}. \quad (3.29)$$

This yields the coupled wave equations for \hat{a}_1 and \hat{a}_3

$$\frac{d\hat{a}_1}{dt} = -\chi\hat{a}_3, \quad \frac{d\hat{a}_3}{dt} = \chi\hat{a}_1, \quad (3.30)$$

where we exploit the fact that \hat{a}_1 and \hat{a}_3 have no explicit time dependence in the interaction picture, i.e. $\partial\hat{a}_1/\partial t = \partial\hat{a}_3/\partial t = 0$. The coupled wave equations are solved by

$$\begin{aligned} \hat{a}_1(t) &= \hat{a}_1(0) \cos \chi t - \hat{a}_3(0) \sin \chi t, \\ \hat{a}_3(t) &= \hat{a}_3(0) \cos \chi t + \hat{a}_1(0) \sin \chi t. \end{aligned} \quad (3.31)$$

Since

$$\hat{a}_3(t = \pi/2\chi) = \hat{a}_1(0) \quad \text{and} \quad \hat{a}_1(t = \pi/2\chi) = -\hat{a}_3(0). \quad (3.32)$$

this solution directly shows that at a certain time $t = \pi/2\chi$, which depends on the power of the pump field, the quantum state at ω_1 is completely converted to a quantum state at ω_3 , while its coherence properties are completely preserved. Thus, we can use the process of sum-frequency generation to convert squeezed and entangled states from the infrared wavelength regime to the visible wavelength regime, as will be shown in Chapter 5.

3.4 Difference Frequency Generation and Optical Parametric Oscillation in Classical Optics

For providing the pump field for the sum-frequency generation and for the generation of squeezed and entangled states at 1550 nm, we need strong coherent fields at 810 nm and 1550 nm. These fields were generated by an optical parametric oscillator (OPO). The principle of an OPO is depicted in Fig. 3.3 (a). It is based on the process of difference frequency generation (DFG), which corresponds to the inverse process of SFG described in the sections before. A photon at frequency ω_3 decays into two photons at the frequencies ω_1 and ω_2 . The nonlinear crystal, which is responsible for the DFG, is thereby placed inside a cavity (cf. Fig. 3.3 (b)) to achieve parametric amplification or oscillation for the generated fields. In principle, a strong pump field

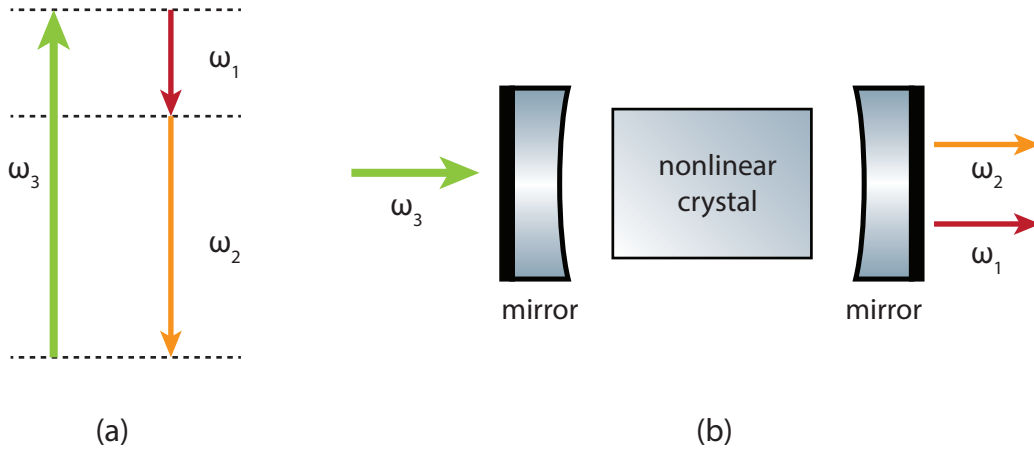


Figure 3.3: Principle of optical parametric oscillation. a) Energy level diagram of optical parametric oscillation. b) Setup of an OPO, where a nonlinear crystal is placed inside a cavity.

and vacuum fluctuations at ω_1 and ω_2 are sufficient to initiate this process.

If we just want to consider this device in a classical way, i.e. when it is operated far above the threshold and provides strong coherent states, it is sufficient and easier to calculate the basic process of difference frequency generation, which is illustrated in Fig. 3.4. Thereby, in addition to the initial pump field at ω_3 , the light field at ω_1 is also injected and due to the nonlinear process, the light fields at ω_1 and at the difference frequency $\omega_2 = \omega_3 - \omega_1$ are enhanced and generated, respectively.

In the following we will treat the DFG classically like the SFG before (cf. Sec. 3.2) and see that the threshold for starting the oscillation, when the nonlinear medium is placed inside a cavity, depends on the pump power at ω_3 . Again we follow [Boy08]. After illustrating the classical DFG, we will see that if we consider the process in the degenerate case ($\omega_1 = \omega_2$) and in a quantum manner, this device can generate squeezed states of light.

As before, we assume that the pump field (in this case at ω_3) is strong and undepleted by the nonlinear interaction, i.e. the amplitude A_3 remains constant. Furthermore, we set the boundary conditions

$$A_2(0) = 0, \quad A_1(0) \text{ arbitrary}, \quad (3.33)$$

i.e. at the beginning there is no field at ω_2 . For this classical treatment we start with a non-vanishing light field at ω_1 . Similar to Section 3.2 we obtain the coupled

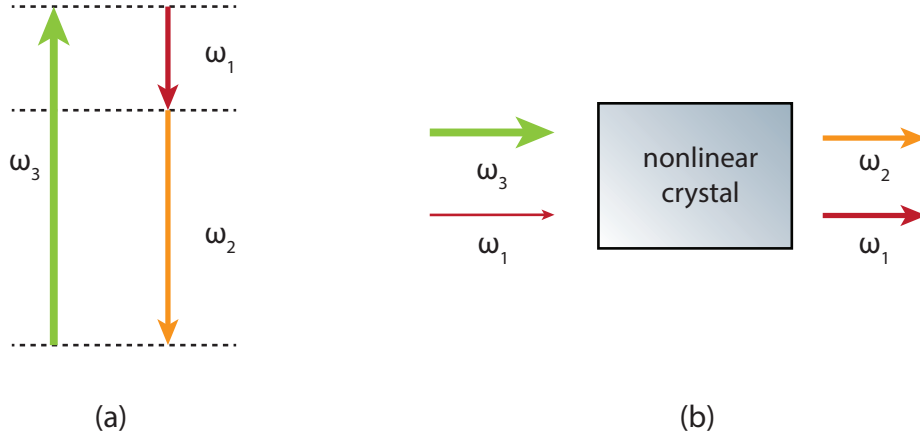


Figure 3.4: Principle of difference frequency generation. a) Energy level diagram of DFG. b) For DFG the field at frequency ω_1 is also sent to the nonlinear crystal. A cavity is not necessarily required.

wave equations

$$\frac{dA_1}{dz} = \frac{2i\omega_1^2 d_{\text{eff}}}{k_1 c^2} A_3 A_2^* e^{i\Delta k z}, \quad (3.34a)$$

$$\frac{dA_2}{dz} = \frac{2i\omega_2^2 d_{\text{eff}}}{k_2 c^2} A_3 A_1^* e^{i\Delta k z}, \quad (3.34b)$$

with the wave vector mismatch

$$\Delta k = k_3 - k_1 - k_2. \quad (3.35)$$

With the quantities

$$g = \sqrt{\kappa_1 \kappa_2^* - (\Delta k/2)^2}, \quad \kappa_i = \frac{2i\omega_i^2 d_{\text{eff}} A_3}{k_i c^2} \quad (3.36)$$

the solution of the coupled wave equations is given by

$$A_1(z) = \left[A_1(0) \left(\cosh gz - \frac{i\Delta k}{2g} \sinh gz \right) + \frac{\kappa_1}{g} A_2^*(0) \sinh gz \right] e^{i\Delta k z/2}, \quad (3.37a)$$

$$A_2(z) = \left[A_2(0) \left(\cosh gz - \frac{i\Delta k}{2g} \sinh gz \right) + \frac{\kappa_2}{g} A_1^*(0) \sinh gz \right] e^{i\Delta k z/2}. \quad (3.37b)$$

If we additionally use the boundary conditions in Eq. 3.33, these equations simplify to

$$A_1(z) = \left(\cosh gz - \frac{i\Delta k}{2g} \sinh gz \right) A_1(0) e^{i\Delta k z/2}, \quad (3.38a)$$

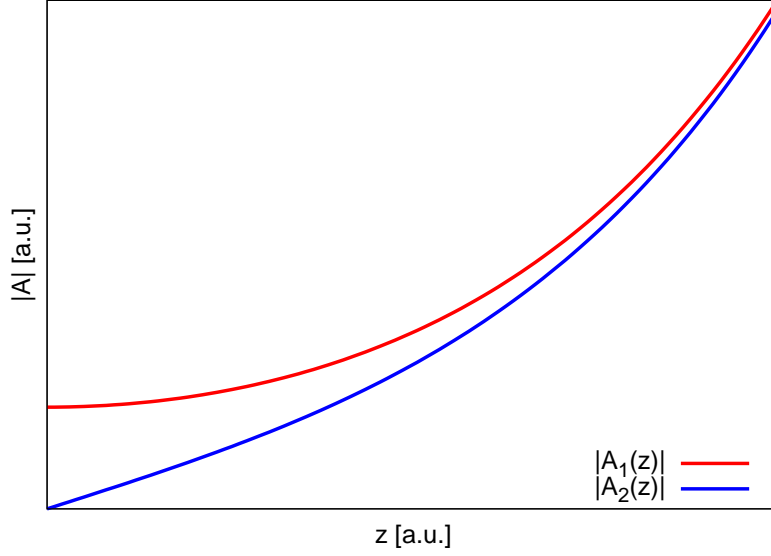


Figure 3.5: Spatial variation of the generated fields from difference frequency generation. The intensity of the generated field grows exponentially with increasing penetration depth z in the nonlinear medium.

$$A_2(z) = \left(\frac{\kappa_2}{g} A_1^*(0) \sinh gz \right) e^{i\Delta kz/2}. \quad (3.38b)$$

For large z both fields grow exponentially, which can be seen in Fig. 3.5, where the intensity of the fields are plotted versus the length of the nonlinear medium.

In the next step we consider the case when the nonlinear medium is placed inside a cavity and can thus provide oscillating fields at ω_1 and ω_2 . The process (and also the device) is then called optical parametric oscillation (optical parametric oscillator, respectively) or in short OPO. In the following we want to derive a formula for the threshold power which is needed to generate oscillating fields at ω_1 and ω_2 . Therefore, we have to describe the nonlinear crystal with length L inside a cavity (cf. Fig. 3.3) with mirror reflectivities R_1 and R_2 . For simplicity, the length of the cavity equals the length of the nonlinear crystal.

Generally, one can say that the fields within the cavity have to replicate themselves after each round trip to achieve optical parametric oscillation. If we also assume perfect phase matching ($\Delta k = 0$) this condition leads to the equations

$$A_1(0) = \left[A_1(0) \cosh gL + \frac{\kappa_1}{g} A_2^*(0) \sinh gL \right] (1 - l_1), \quad (3.39a)$$

$$A_2(0) = \left[A_2^*(0) \cosh gL + \frac{\kappa_2^*}{g} A_1(0) \sinh gL \right] (1 - l_2), \quad (3.39b)$$

where $l_i = 1 - R_i e^{-\alpha_i L}$ corresponds to the fractional amplitude loss per pass with α_i being the absorption coefficient of the crystal at frequency ω_i . These equations have to be satisfied simultaneously. Thus, the threshold condition can be written as

$$\cosh gL = 1 + \frac{l_1 l_2}{2 - l_1 - l_2}. \quad (3.40)$$

Since we just want to consider the doubly resonant case, we can assume the losses for the two generated fields to be very low ($l_1, l_2 \ll 1$) and can approximate $\cosh gL$ by $1 + \frac{1}{2}g^2 L^2$. In this limit, the threshold condition for a doubly resonant oscillator with perfect phase matching is

$$g^2 L^2 = l_1 l_2. \quad (3.41)$$

Without assuming perfect phase matching ($\Delta k \neq 0$) we obtain the threshold condition

$$g^2 L^2 \text{sinc}^2(\Delta k L/2) = l_1 l_2. \quad (3.42)$$

When we use the simplified threshold condition Eq. 3.41 and express the pump field A_3 in terms of the intensity [Yar89]

$$I_3 = \frac{1}{2} \sqrt{\frac{\epsilon_0 n_3^2}{\mu_0}} A_3^2, \quad (3.43)$$

we can even obtain an intensity threshold for the pump field at ω_3 . This threshold can be written as

$$I_{\text{thr}} = 8 \left(\frac{\epsilon_0}{\mu_0} \right)^{3/2} \frac{n_1 n_2 n_3 (1 - l_1)(1 - l_2)}{\omega_1 \omega_3 l^2 d^2}, \quad (3.44)$$

with d being the nonlinear coefficient of the nonlinear medium. When the threshold condition for the OPO is satisfied, it can generally produce any wavelengths which fit the condition $\omega_1 + \omega_2 = \omega_3$. For a doubly resonant non-degenerate OPO it is worth having a closer look at its tuning characteristics. If such a device is used, oscillation will occur when both modes are simultaneously resonant and can thus oscillate. That is the reason why a doubly resonant OPO cannot be tuned in a smooth way. Small fluctuations in the pump frequency, the cavity's length or the temperature cause disproportionately large variations in the signal and idler field. As the cavity modes are not equally spaced (due to the different wavelength of the signal and idler field and the wavelength depending refractive index) it can happen that two modes oscillate which are not closest to perfect phase-matching. This situation is illustrated in Fig. 3.6, where the mode structure and the gain profile for a doubly resonant OPO are depicted. The oscillation occurs for non-perfect

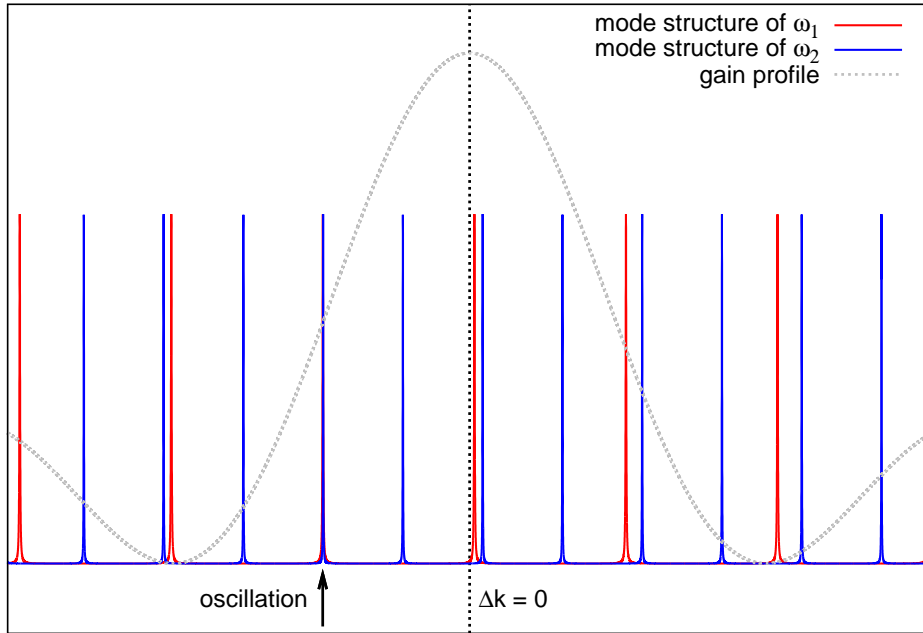


Figure 3.6: Gain profile and mode structure of a doubly resonant OPO. Oscillation occurs when both modes are simultaneously resonant. These modes are not necessarily the closest to perfect phase-matching.

phase-matching. Thus, the OPO does not provide as much power in the signal and idler mode as it could for a vanishing wave vector mismatch. If one of the cavity's parameters is tuned (e.g. the crystal's temperature or the length), an axial mode hop occurs and two adjacent modes can oscillate. In Fig. 3.7 (a)–(c) these mode hops are illustrated. In Fig. 3.7 (d) the situation is slightly different since a variation of a cavity parameter now leads to a cluster jump.

When a mode hop occurred, the signal resonance frequencies increased, while the idler resonance frequencies decreased. For a cluster jump the resonance frequencies move in the opposite direction. To illustrate this behavior Fig. 3.8 shows the measured wavelength of the outgoing signal field from the OPO used within this thesis as the crystal temperature is varied. The mode hops lay on the black lines, while two black lines correspond to two different clusters. One can see, that if the temperature is increased continuously, the outgoing wavelength also increases as long as it decreases to another cluster. In this manner the wavelength decreases with increasing temperature if we average over a larger distance.

A detailed description of mode hops and cluster jumps of an OPO can be found in the paper from Eckhard *et al.* [Eck91].

For the experiments executed within this thesis we used a doubly resonant OPO

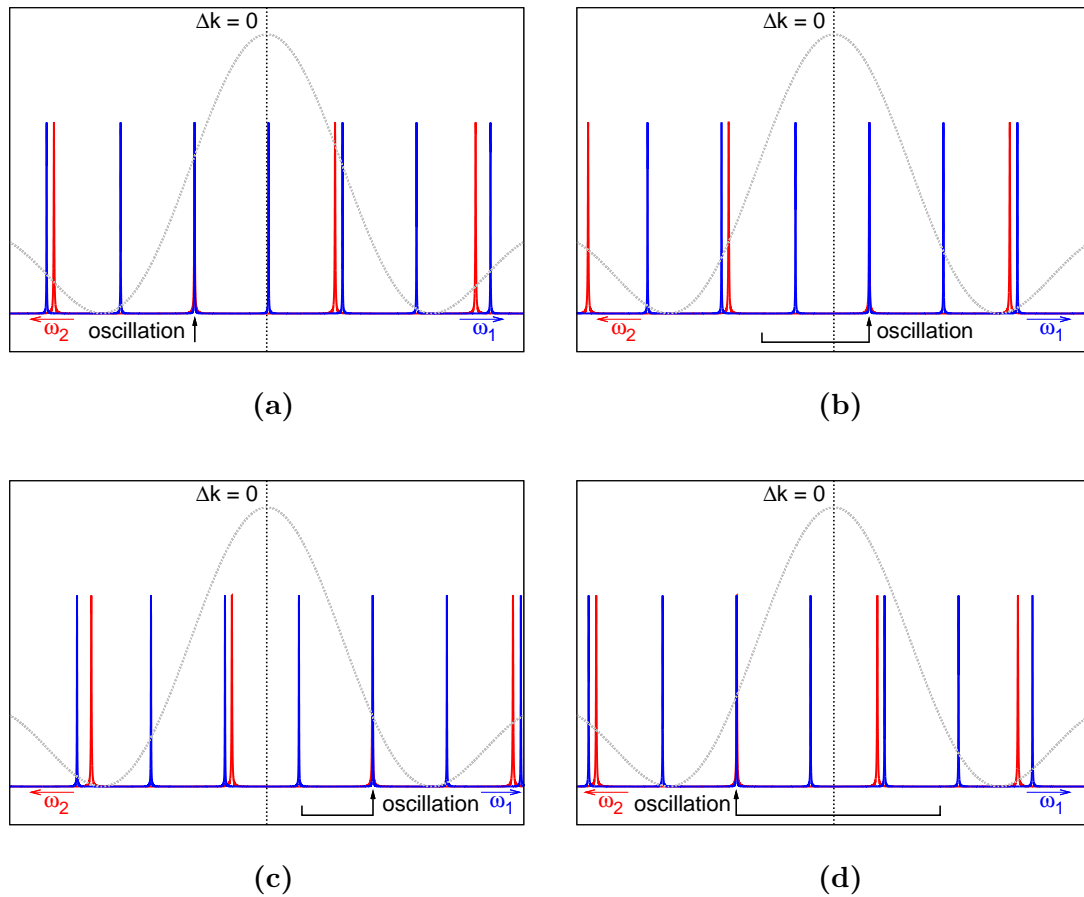


Figure 3.7: Mode hops and cluster jumps of an OPO. If a parameter of the cavity is tuned (e.g. the crystal's temperature or the cavity's length), the resonance condition is changed and the resonance frequencies of ω_1 move to the right, while the resonances of ω_2 move to the left. Therefore, modes hops occur from (a)→(b) and (b)→(c). From (c)→(d) a change of the resonance condition leads to a cluster jump, which results in larger oscillating frequencies.

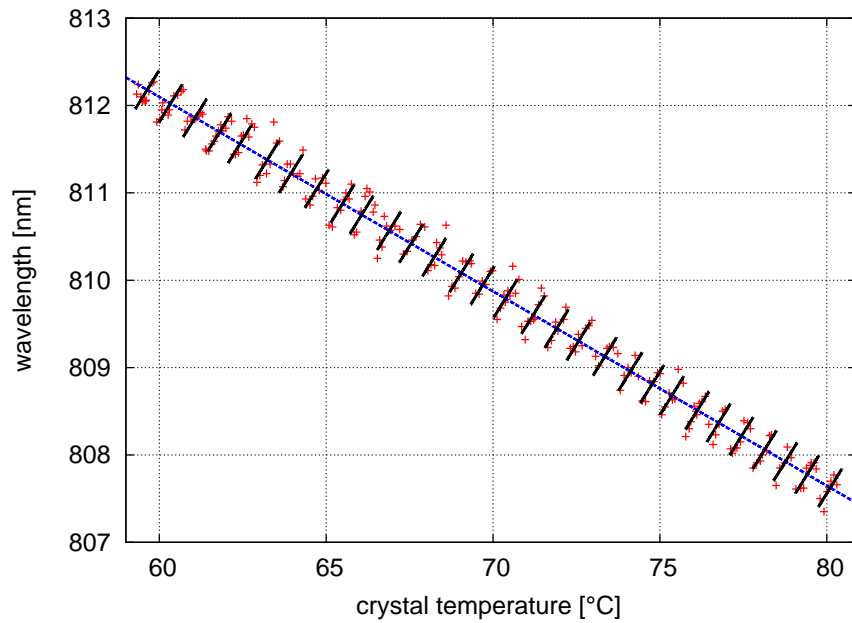


Figure 3.8: Mode hops and cluster jumps of an OPO. The red crosses show the measured outgoing wavelength of the OPO’s signal field used in this thesis. The black lines illustrate different clusters. The blue dashed line shows an overall average of the decreasing wavelength for an increasing temperature. Details can be found in reference [Sam12].

which is pumped at 532 nm to have a source of highly coherent outputs at 1550 nm and 810 nm. The OPO can provide these output fields, as the statistical properties of the pump field are reproduced with little additional noise (theoretically shown in [Gra68]).

3.5 Quantum Description of Parametric Down Conversion

Like before when we considered the SFG process, we now have to look at the quantum description of the DFG process to understand the generation of squeezed and thus non-classical light fields. For the generation of squeezed vacuum states of light the OPO is operated below threshold and therefore called optical parametric amplifier (OPA). Apart from this, the DFG is degenerate, i.e. one pump photon at frequency ω_2 decays in pairs of two signal photons at frequency $\omega_1 = \frac{1}{2}\omega_2$. Therefore, this process is also called *degenerate parametric down-conversion*. The Hamiltonian for this process is given by [Ger10]

$$\hat{H}_{\text{OPA}} = \hbar\omega_1\hat{a}_1^\dagger\hat{a}_1 + \hbar\omega_1\hat{a}_2^\dagger\hat{a}_2 + i\hbar\chi^{(2)}(\hat{a}_1^2\hat{a}_2^\dagger - \hat{a}_1^\dagger\hat{a}_2), \quad (3.45)$$

where $\hat{a}_{1,2}$ and $\hat{a}_{1,2}^\dagger$ are the annihilation and creations operators of the signal and pump field, respectively. With the assumption of a strong, coherent, undepleted pump field, the operators \hat{a}_2 and \hat{a}_2^\dagger can be approximated by $\alpha e^{-i\omega_2 t}$ and $\alpha^* e^{-i\omega_2 t}$. When we additionally drop irrelevant constant terms, the Hamiltonian reduces to

$$\hat{H}_{\text{OPA}} = \hbar\omega_1\hat{a}_1^\dagger\hat{a}_1 + i\hbar\left(\eta^*\hat{a}_1^2 e^{i\omega_2 t} - \eta\hat{a}_1^{\dagger 2} e^{-i\omega_2 t}\right), \quad (3.46)$$

with $\eta = \chi^{(2)}\alpha$. In the interaction picture we obtain

$$\hat{H}_{\text{Int}}(t) = i\hbar\left(\eta^*\hat{a}_1^2 e^{i(\omega_2-\omega_1)t} - \eta\hat{a}_1^{\dagger 2} e^{-i(\omega_2-\omega_1)t}\right). \quad (3.47)$$

Since we consider the degenerate case and thus $\omega_2 = 2\omega_1$, we obtain the time-independent interaction Hamiltonian of the OPA process

$$\hat{H}_{\text{Int}} = i\hbar\left(\eta^*\hat{a}_1^2 - \eta\hat{a}_1^{\dagger 2}\right), \quad (3.48)$$

and its corresponding evolution operator

$$\hat{U}_{\text{Int}}(t, 0) = \exp(-i\hat{H}_{\text{Int}}t/\hbar) = \exp(\eta^*t\hat{a}_1^2 - \eta t\hat{a}_1^{\dagger 2}). \quad (3.49)$$

This evolution operator equals the squeezing operator from Eq. 2.25 introduced in Section 2.7 $\hat{U}_{\text{Int}}(t, 0) = \hat{S}(\xi)$ for $\xi = 2\eta t$. Thus, an OPA consisting of a nonlinear medium can be used for the generation of squeezed states.

3.6 Phase-Matching

For the nonlinear processes, which have been described in this chapter, phase-matching is a crucial requirement. A perfect phase-matching (for plan waves: $\Delta k = 0$) means that a specific phase relation of the generated fields is maintained with respect to the nonlinear polarization so that they are amplified by constructive interference and not attenuated by destructive interference.

The condition of a non-vanishing wave vector mismatch for the processes where three different light fields are involved (like SFG and DFG)

$$\Delta k = k_1 + k_2 - k_3 = 0 \quad (3.50)$$

can also be written within the plane wave approximation as [Boy08]

$$\frac{n_1\omega_1}{c_0} + \frac{n_2\omega_2}{c_0} = \frac{n_3\omega_3}{c_0}, \quad (3.51)$$

where c_0 is the speed of light in vacuum. Usually, we can assume that $\omega_1 \leq \omega_2 \leq \omega_3$. Therefore, the phase-matching condition cannot be achieved, since in most nonlinear crystals the refractive index n is an increasing function of frequency. This effect is known as *normal dispersion*.

To overcome this obstacle birefringence in crystals can be exploited. If a medium is birefringent, its refractive index is dependent on the direction of polarization of the optical radiation. This property reveals two different ways to achieve phase matching known as type I and II. A third possibility is quasi phase-matching. All three possibilities will be explained in the next two paragraphs.

Type I and II phase-matching

For the type I phase-matching the field at the highest frequency ω_3 is polarized in the direction with the lower refractive index and the other two fields are orthogonally polarized to this axis, while for type II phase-matching the two other fields are not identically polarized, but one of them is in the same polarization as the field at ω_3 . Due to the temperature dependence of the refractive index the phase matching condition can be satisfied by temperature tuning of the crystal. This technique is applied to several crystals used for the generation of squeezed light within this thesis. Since their phase-matching temperature is around 70° we tended to use quasi phase-matching, where we can also use crystals with a higher nonlinear susceptibility, which are not birefringent.

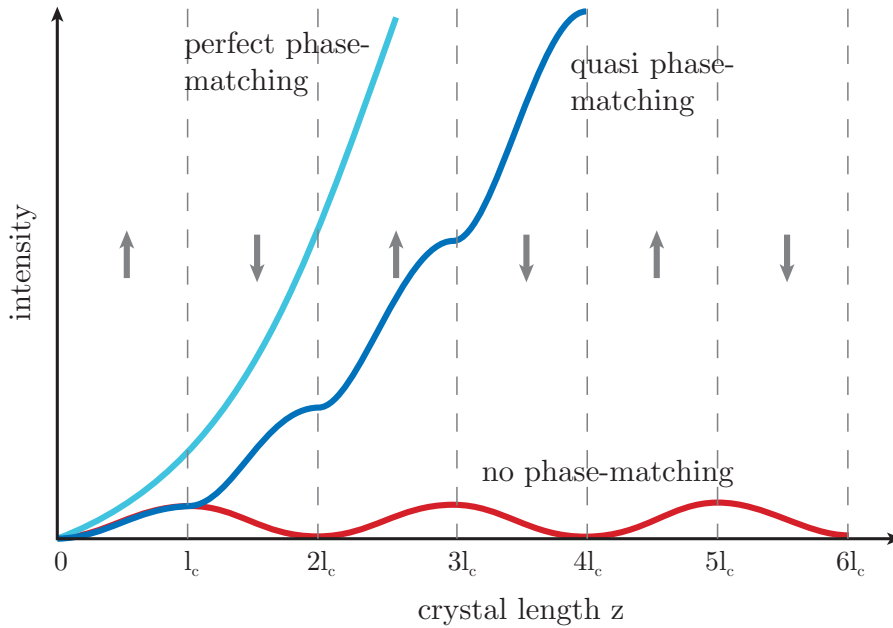


Figure 3.9: Different methods of phase-matching. The red curve illustrates the situation without phase-matching, the light blue one shows the intensity of the generate field for perfect phase-matching and the dark blue curve the intensity for quasi phase-matching. The gray arrows correspond to the orientation of one of the crystalline axes, when quasi phase-matching is used. The graph is based on a figure in [Fej92].

Quasi phase-matching

Sometimes the phase-matching temperature for type I or II phase-matching is too high or the birefringence of the crystal is insufficient to compensate the dispersion (especially for shorter wavelengths). In such cases a periodically poled crystal can be used to implement the technique of quasi phase-matching. In a periodically poled material the orientation of one of the crystalline axes is inverted periodically, most efficient after the coherence length l_c . That means that each time the field amplitude of the generated field begins to decrease due to the wave vector mismatch, the sign of the effective susceptibility d_{eff} is changed. This results in a monotonically growing field amplitude. The optimum poling period is two times the coherence length

$$\Lambda = 2 \times l_c = \frac{2\pi}{k_1 + k_2 - k_3} \quad (3.52)$$

and is in the regime of a few micrometers for the crystals we use in our experiments. In Fig. 3.9 a comparison between the intensities of the generated waves at no phase-matching, phase-matching and quasi phase-matching is depicted.

Basic Experimental Techniques

This chapter deals with some of the experimental techniques which were used for the experiments performed for this thesis. The first section illustrates the experimental generation of squeezed states with an optical parametric amplifier (OPA). In Section 4.2 the principle of homodyne detection is explained, which is used for all experiments to measure arbitrary quadratures of a certain quantum state. The technique of locking a phase gate or a homodyne detector with a single sideband in Section 4.3 and the thermal state generation in Section 4.4 was only used for distributing entanglement by separable states (cf. Chapter 6) and will be explained at the end of this chapter.

4.1 Squeezed-Light Generation

Sections 2.7 and 3.5 have already introduced theoretically the generation of squeezed states. Here, we want to show how the generation is realized experimentally. The generation scheme is depicted in Fig. 4.1. The OPA as the actual squeezing source consists of a nonlinear crystal with a curved, high reflective coated end surface and a front mirror mounted on a piezo-electric transducer (PZT). Details of the assembling of the OPA cavity used within the experiments of this thesis are e.g. given in [Kha11]. In the experimental chapters 5 and 6 the corresponding reflectivities for the pump and squeezed beams for each OPA cavity can be found.

The pump field at ω_2 is transmitted by a dichroic beam splitter (DBS) and enters the cavity of the OPA through the front mirror. Its phase, which determines the squeezed quadrature, can be shifted by a phase shifter (PS). The generated squeezed field at frequency $\omega_1 = \frac{1}{2}\omega_2$ leaves the cavity at the front mirror and is reflected by the DBS. For stabilizing the length of the cavity or for alignment purposes a control

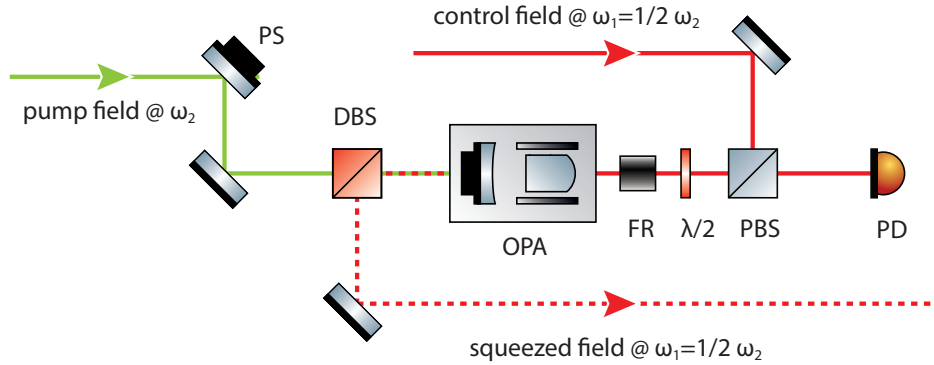


Figure 4.1: Experimental generation of squeezed states. The pump field enters the cavity through the front mirror. The dichroic beam splitter (DBS) in front of the cavity separates the pump field and the outgoing squeezed field. For length control of the cavity or alignment purposes a control field enters the cavity from the back side and its reflection is detected by the photo diode (PD), since it passes the polarizing beam splitter (PBS), a wave plate ($\lambda/2$), and a Faraday rotator (FR).

field at the same frequency as the squeezed field enters the OPA from the back side. As it passes a polarizing beam splitter (PBS), a half-wave plate ($\lambda/2$), and a Faraday rotator (FR), its back reflection can be detected in transmission of the PBS by a photo diode (PD), which can provide an error signal for locking the cavity length. Generally, this photodiode can also provide the error signal for stabilizing the phase of the pump field. Furthermore, the locking of the cavity length can also be done with the pump field, if the cavity is doubly-resonant. This technique is realized in the quantum up-conversion experiment (cf. Chapter 5).

4.2 Homodyne Detection

For detecting and measuring light fields usually a photo diode is used, which detects the intensity of the light field and thus measures its amplitude quadrature. If we want to characterize squeezed or entangled states of light, it is necessary to measure the amplitude and the phase quadrature of the light fields. For this purpose we use homodyne detectors. In Fig. 4.2 the setup of a homodyne detector is shown. The signal field, which we want to measure, is superimposed at a beam splitter with a strong light field, called *local oscillator* (LO), which matches the signal field in frequency, beam parameters, and polarization. The two outputs of the beam splitter are detected by photo diodes. Their photon current is directly subtracted on the circuit board. Since we use a 50/50 beam splitter this detection scheme is also called *balanced* homodyne detector. If we denote the signal field with mode \hat{a} and the local

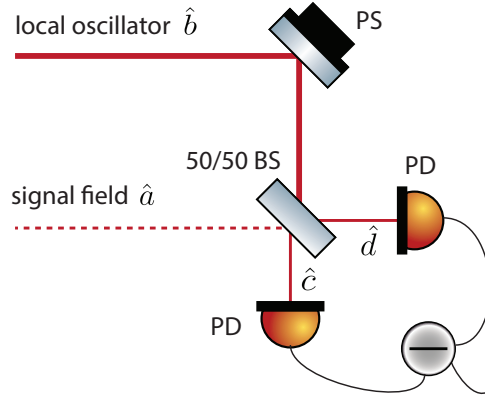


Figure 4.2: Principle of homodyne detection. For *balanced* homodyne detection a local oscillator (LO) and the signal light field which shall be measured are superimposed at a 50/50 beam splitter (BS). The phase between the two light fields can be changed by the phase shifter PS. The outputs of the beam splitter are detected by photo diodes (PD), whose photo currents are directly subtracted electronically.

oscillator field with mode \hat{b} , we obtain the output modes of the beam splitter \hat{c} and \hat{d}

$$\begin{aligned}\hat{c} &= \frac{1}{\sqrt{2}}(\hat{a} + i\hat{b}), \\ \hat{d} &= \frac{1}{\sqrt{2}}(\hat{b} + i\hat{a}),\end{aligned}\tag{4.1}$$

[Ger10]. This output modes are detected by the two photo diodes and the mean of their subtracted photo currents are given by

$$\begin{aligned}I_c - I_d &\propto \langle \hat{c}^\dagger \hat{c} - \hat{d}^\dagger \hat{d} \rangle \\ &= i \langle \hat{a}^\dagger \hat{b} - \hat{a} \hat{b}^\dagger \rangle.\end{aligned}\tag{4.2}$$

If the local oscillator field is much larger than the signal field we can presume the LO to be in the coherent state $|\beta e^{i\omega t}\rangle$ with $\beta = |\beta|e^{i\Psi}$ and Ψ being the LO's phase. Thus, we obtain

$$I_c - I_d \propto |\beta| \langle \hat{a} e^{i\omega t} e^{-i\theta} + \hat{a}^\dagger e^{-i\omega t} e^{i\theta} \rangle,\tag{4.3}$$

where $\theta = \Psi + \frac{\pi}{2}$. As the modes \hat{a} and \hat{b} have the same frequency ω (usually this modes originate from the same laser source), we can set $\hat{a} = \hat{a}_0 e^{-i\omega t}$ and with the quadrature operator

$$\hat{X}(\theta) = \frac{1}{2} \left[\hat{a}_0 e^{-i\theta} + \hat{a}_0^\dagger e^{i\theta} \right]\tag{4.4}$$

at the angle θ we obtain

$$I_c - I_d \propto |\beta| \langle \hat{X}(\theta) \rangle.\tag{4.5}$$

This means, that we can measure every quadrature of the signal field by changing the phase of the LO. Apart from that, the measurement signal scales with the LO's amplitude and can thus be amplified. This detection scheme enables a whole tomography and the reconstruction of the covariance matrix of a quantum state.

4.3 Single Sideband Locking Scheme

For stabilizing various phases in our setup for entanglement distribution by separable states a stable single sideband in addition to our states was required. The setup we used for generating a stable single sideband utilized a frequency shifted auxiliary laser, which was phase-locked at 15 MHz with respect to the master laser. A fraction of the auxiliary laser was overlapped with the control field and provided thus the single sideband. Since the single sideband is weak compared to the signal field, its addition corresponds to a modulation of the amplitude and phase quadrature with a low modulation depth. The resulting field can thus be written as

$$\hat{a}_1 = \alpha_{\text{sig}}(1 + me^{i\omega_{\text{beat}}t}), \quad (4.6)$$

where α_{sig} is the field amplitude of the signal field, m denotes the modulation strength and ω_{beat} is the detuning of the auxiliary field with respect to the signal field.

In the following the locking scheme of a phase gate utilizing the single side band is introduced. In this thesis we call a phase gate a balanced beam splitter, where two light fields are overlapped with a specific, tunable phase. In Fig. 4.3 such a device is depicted including the locking devices needed for stabilizing the phase of the two incoming fields \hat{a}_1 and \hat{a}_2 . The error signal is obtained by detecting a fraction ($\approx 1\%$) of the two outgoing light fields and the direct substration of the two photo currents. We presume that the field \hat{a}_1 contains the single sideband and is given by Eq. 4.6. After the interference with the field \hat{a}_2 at the balanced beam splitter the two outgoing fields result in

$$\begin{aligned} \hat{a}_3 &= \frac{1}{\sqrt{2}}(\alpha_{\text{sig}}(1 + me^{i\omega_{\text{beat}}t}) + \alpha_2 e^{i\theta}), \\ \hat{a}_4 &= \frac{1}{\sqrt{2}}(\alpha_{\text{sig}}(1 + me^{i\omega_{\text{beat}}t}) - \alpha_2 e^{i\theta}). \end{aligned} \quad (4.7)$$

Two photo diodes, one behind a high reflective mirror and the other one in reflection of a 99/1 beam splitter (since the quantum states \hat{a}_3 and \hat{a}_4 should not be attenuated), detect this two fields and their alternating currents (AC) are subtracted.

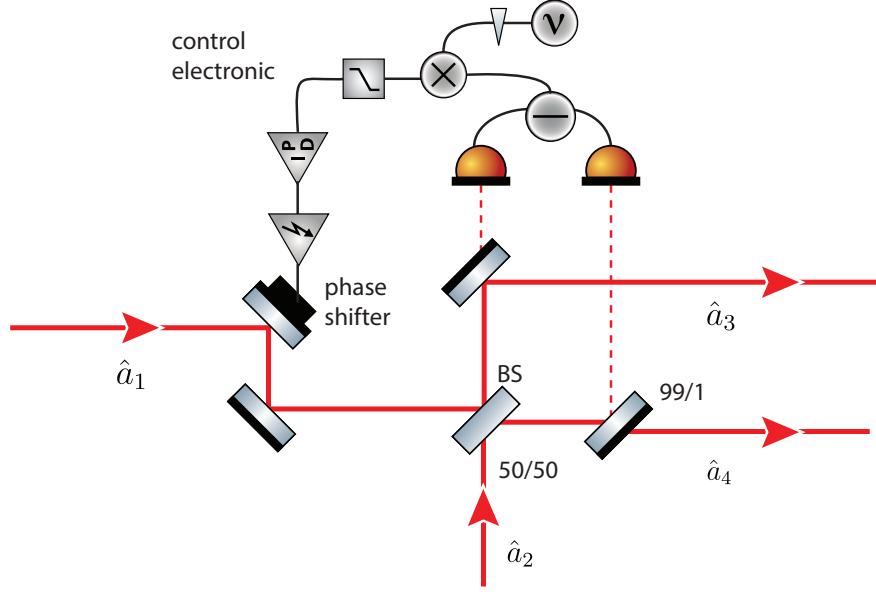


Figure 4.3: Stabilization scheme of a phase gate. Two light fields are superimposed at a balanced beam splitter (BS). The phase between these fields is actively controlled by the phase shifter at mode \hat{a}_1 . We obtain an error signal by detecting a fraction of the outgoing light fields and subtracting the photo currents electronically.

This leads to the subtracted signal

$$\begin{aligned} \hat{i}_{\text{sub}} &\propto \hat{a}_1^* \hat{a}_1 - \hat{a}_2^* \hat{a}_2 \\ &= 2\alpha_{\text{sig}} \alpha_2 m \cos(\omega_{\text{beat}} t - \theta). \end{aligned} \quad (4.8)$$

The error signal for setting the phase gate to a certain phase relation is then obtained by mixing the signal with the electronic local oscillator $\sin(\omega_{\text{beat}} t - \phi)$ and low-pass filtering

$$\hat{i}_{\text{error}} \propto \alpha_{\text{sig}} \alpha_2 m \sin(\theta - \phi), \quad (4.9)$$

with ϕ being the phase of the electronic local oscillator. The expression shows that a zero crossing of the error signal is achieved if $\phi = \theta$. Thus, we can stabilize the phase gate to any phase relation between \hat{a}_1 and \hat{a}_2 by setting the phase of the electronic local oscillator to the corresponding angle. In Fig. 4.4 different error signals for different phases ϕ are depicted.

The same scheme also works for locking a homodyne detector to a certain quadrature. Such a stabilization is required when we want to reconstruct the covariance matrix of a quantum state (cf. Chapter 6) and therefore need a stable quadrature readout for arbitrary quadratures.

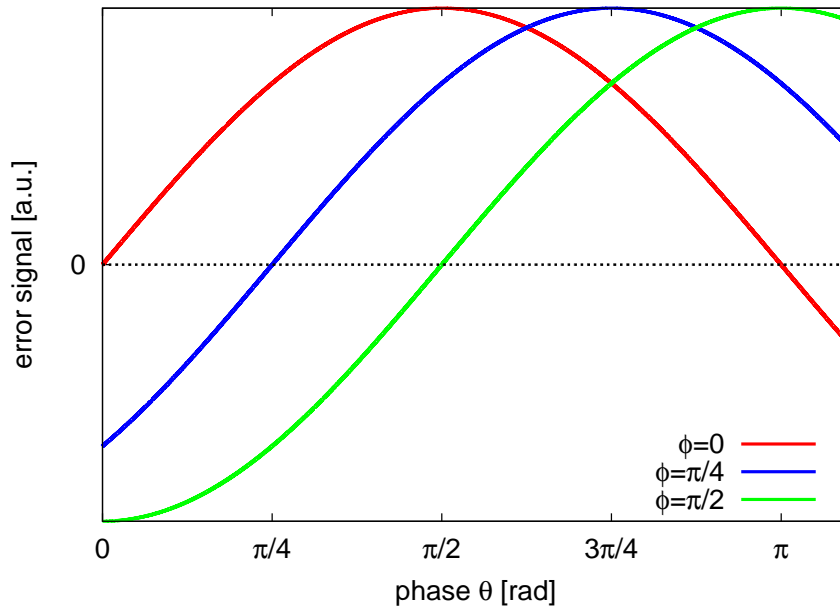


Figure 4.4: Error signals for stabilizing a phase gate. The zero crossing and thus the stabilization point corresponds to the phase of the electronic oscillator ϕ . Thereby, we can set a phase gate or a homodyne detector to an arbitrary angle θ .

4.4 Thermal State Generation

For the entanglement distribution by separable states thermal states are a crucial requirement (cf. Chapter 6). These states, whose noise in each quadrature is above the vacuum noise, can be generated in several ways. One possibility is the superposition of two squeezed states with a phase shift of 90° at a balanced beam splitter. Their outputs are then entangled [Kim02], but each single output is a thermal state. This technique, however, requires two squeezers and an additional phase lock of the phase between the two squeezed fields. Another possibility is the usage of an electro-optical modulator (EOM), which imprints a phase modulation on the light field, and an acousto-optical oscillator, which imprints an amplitude modulation on the light field. However, this technique is challenging if a broadband thermal state is required. In our experimental setup we used a squeezed state and an electro-optical modulator for generating thermal states. The generation scheme is depicted in Fig. 4.5. In principle, it is the same setup as for generating squeezed states of light. In addition, the coherent control field has to pass an EOM which phase modulates the light field. The phase modulation originates from vacuum noise which is measured with the homodyne detector (HD) and is perfectly random. The vacuum noise signal is electronically enhanced and generates a phase modulation of the control field at a certain side band frequency. Generally, just a small fraction of this

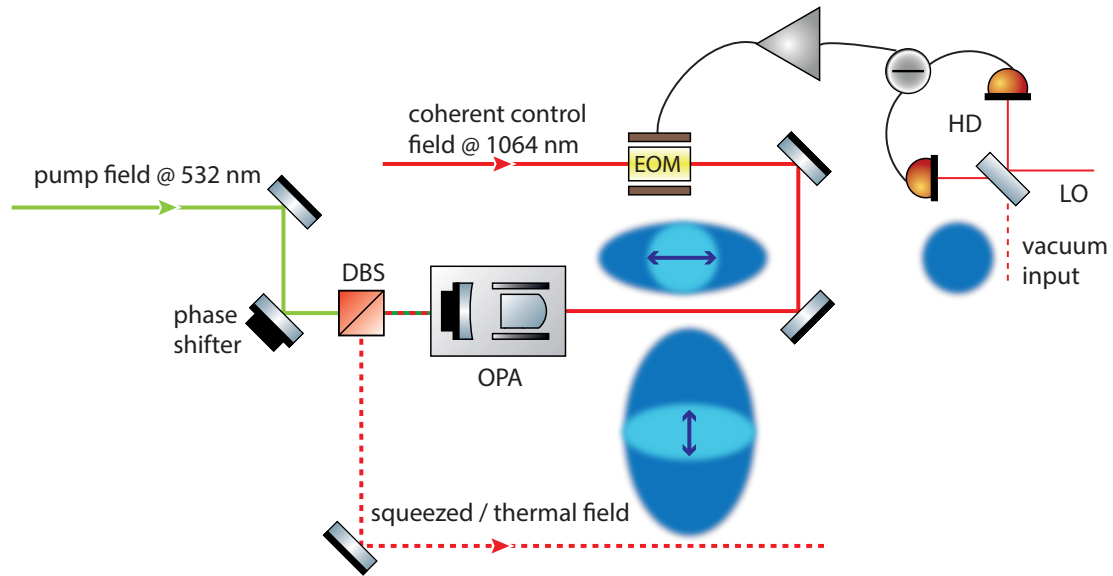


Figure 4.5: Generation of a thermal state. The OPA generates a phase-squeezed light field, whose phase quadrature has been modulated by an electro-optical modulator (EOM). Vacuum noise which is detected by a homodyne detector (HD) and amplified electronically causes a phase modulation of the control field since it is used as a modulation signal of the EOM.

sideband will leave the OPA cavity. However, if the modulation is strong, this leads to a sufficiently strong noise in the phase quadrature. Since the OPA is stabilized to squeeze the phase quadrature and anti-squeeze the amplitude quadrature, this setup leads to states, whose noise is above the vacuum noise in each quadrature. The variance of this noise can be determined by the amplification of the vacuum noise for the phase modulation and by the squeezing strength.

Quantum Up-Conversion

The technique of quantum up-conversion gives access to quantum states in wavelength regimes that cannot be reached by usual methods. For instance, highly non-classical states like Schrödinger Kitten states [Our06, NN06] or squeezed states of light can thus be generated at wavelengths not accessible by well developed methods like parametric down-conversion. In particular, squeezed states of light at various wavelengths have a variety of applications like quantum imaging [Tre03, Bri10], quantum spectroscopy [Pol92, Tay13], teleportation [Fur98, Bow03], gravitational wave astronomy [Cav81, Sch10] or quantum key distribution [Cer01, Fur12].

Squeezed states of light are usually generated by parametric down-conversion (cf. Section 3.5) in the infrared wavelength regime. For shorter wavelengths this method is no longer suitable, since the second harmonic of the squeezed field, which is required as a pump field, would be in the ultra violet (UV) regime. Up to now, no materials with good non-linear properties and low absorption are available for UV light. A further alternative for generating squeezed states of light is second harmonic generation [Kür93]. However, with this method only bright squeezed states of light can be generated. For gravitational wave detectors, as well as for quantum imaging, squeezed *vacuum* states of light are required. For generating these states at shorter wavelengths quantum up-conversion is an excellent alternative method.

By up-converting one mode of an entangled state (generated by a squeezed vacuum state and a balanced beam splitter, cf. Section 2.9.2) entanglement between different wavelengths can be established and thus, different tasks in quantum optics can be connected. For instance, quantum states can be transmitted over reasonable distances by standard telecommunications fibers at a wavelength of 1550 nm [Sas11]. To store quantum states in quantum memories, wavelengths corresponding to accessible atomic transitions are necessary [Hed10, Lvo09].

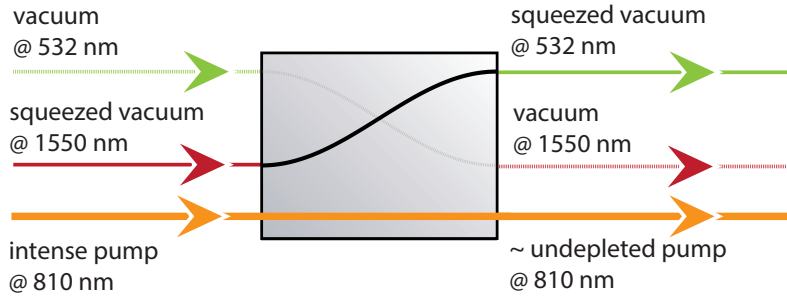


Figure 5.1: Schematic of quantum up-conversion of a squeezed vacuum field from 1550 nm to 532 nm. With the intense pump field at 810 nm the squeezed vacuum state at 1550 nm is up-converted to a squeezed vacuum state at 532 nm via sum-frequency generation.

In the following chapter I will present the experimental realization of quantum up-conversion of a squeezed field from 1550 nm to 532 nm, utilizing a strong pump field at 810 nm. A schematic of this experiment is depicted in Fig. 5.1. The quantum up-conversion was based on sum-frequency generation of 810 nm and 1550 nm. This process maintains the quantum properties, as explained in Section 3.3.

As a first step a squeezed vacuum field at 532 nm was detected. These results are presented in Section 5.2. Next, by adding a balanced beam splitter to the squeezed vacuum field at 1550 nm, an entangled state at 1550 nm was obtained. One part of that state was up-converted to establish entanglement between 1550 nm and 532 nm, which is shown in Section 5.3. At the beginning of this chapter the experimental setup, which is almost identical for the two experiments, is illustrated in Section 5.1. In Section 5.4 the results of the experimental quantum up-conversion of squeezed and entangled states of light are concluded.

5.1 Experimental Setup

Figure 5.2 illustrates the entire experimental setup for the quantum up-conversion. The individual steps of the setup will be described and explained in detail in the following.

5.1.1 Laser Preparation

The light source of the experiment was a Neodymium-doped Yttrium Aluminum Garnet (Nd:YAG) solid state laser from *Inno-light* (model Mephisto) as the main laser source. It provided 2 W of optical power in a single spatial mode at 1064 nm, which was sent to the second-harmonic generation (SHG) cavity after passing a

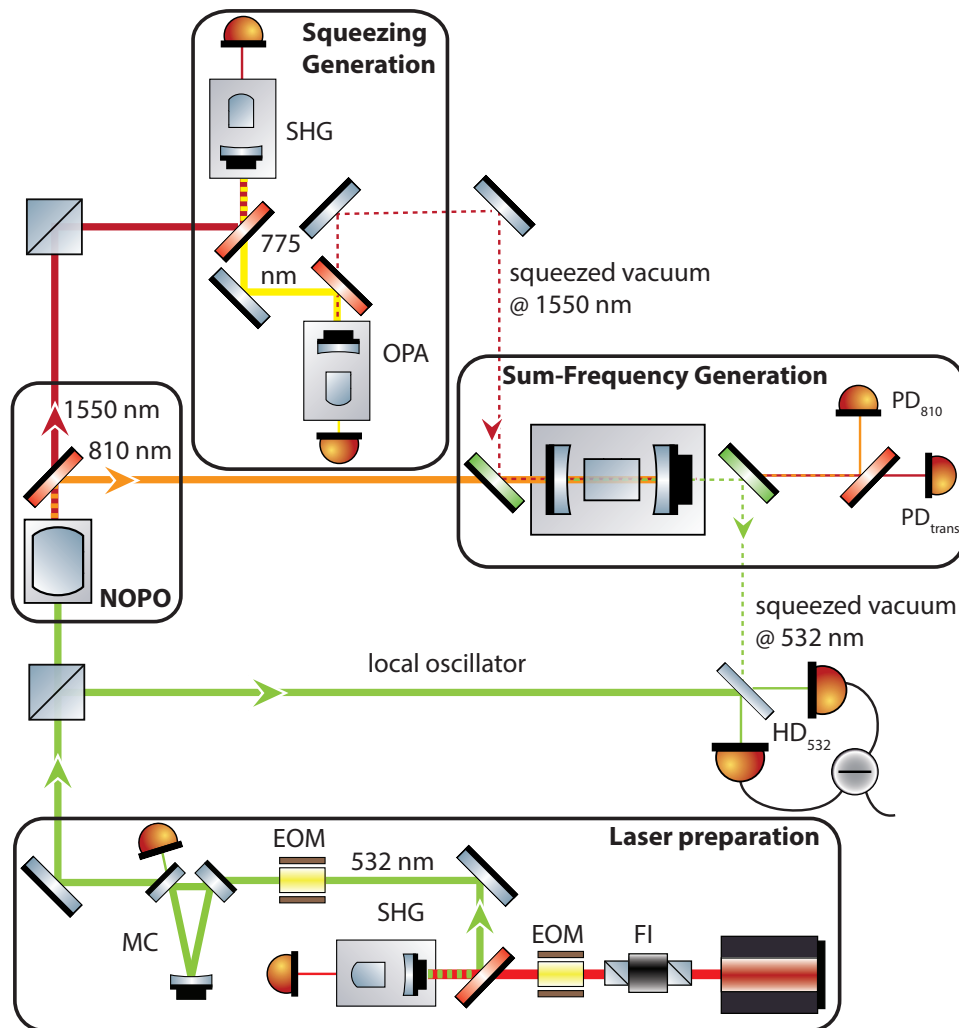
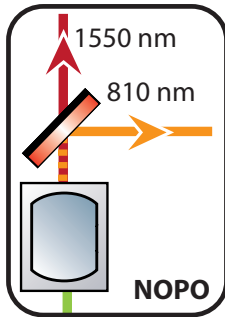


Figure 5.2: Experimental setup of quantum up-conversion. The individual parts of the setup are described in detail in the text. The setup consisted of 4 stages: the laser preparation, where a strong coherent laser field at 532 nm was generated; the non-degenerate optical parametric oscillator (NOPO), which provided two light fields at 1550 nm and 810 nm; the squeezing generation, where squeezed vacuum states at 1550 nm were generated and the sum-frequency generation, where a squeezed vacuum field at 1550 nm and a pump field at 810 nm were converted to a squeezed vacuum field at 532 nm, which could be measured with the homodyne detector HD_{532} . FI: faraday isolator, EOM: electro-optical modulator, SHG: second harmonic generation, MC: mode cleaner, HD: homodyne detector, NOPO: non-degenerate optical parametric oscillator, PDC: parametric down-conversion, PD: photo diode.

Faraday Isolator (FI) to avoid back reflections, and an electro-optical modulator (EOM). The SHG consisted of a 7% doped $\text{MgO}:\text{LiNbO}_3$ crystal with a curved back surface and a coupling mirror. The coupling mirror had a power reflectivity of $R = 90\%$ for 1064 nm and $R < 4\%$ for 532 nm. The flat surface of the nonlinear crystal had an anti-reflection coating and the curved back surface had a high-reflection coating for both wavelengths. The phase modulation at a sideband frequency of 15 MHz generated by the EOM was used to stabilize the length of the cavity with the Pound-Drever-Hall (PDH) locking scheme [Bla01]. In addition to that, the temperature of the crystal was also actively stabilized by Peltier elements. The SHG produced the second harmonic field with an optical power of 1 W, which was sent to a mode cleaner cavity (MC) to filter the TEM_{00} spatial mode profile and to suppress technical noise. The MC had a linewidth of 1.3 MHz, and its length was stabilized with sidebands at 29.5 MHz again using the PDH locking scheme. With this setup, we had a stable laser beam at 532 nm, which could be used as a pump beam for the following non-degenerate optical parametric oscillator.

5.1.2 Non-Degenerate Optical Parametric Oscillator (NOPO)



The NOPO was pumped with the 532 nm beam from the SHG and generated two output beams at 810 nm and 1550 nm. It provided the pump field at 810 nm for the sum-frequency generation (SFG), while the 1550 nm output beam was used to generate squeezed vacuum states at this wavelength. The NOPO consisted of a periodically poled Potassium Titanyl Phosphate (PPKTP) nonlinear crystal, whose two curved surfaces (radii of curvature $r = 8$ mm) formed a monolithic standing-wave cavity for the two output fields. Reflectivities for both outgoing wavelengths of 99.9% at the front surface and 94% at the back surface created a cavity with a finesse of $\mathcal{F} = 100$, a linewidth of 91 MHz and a free spectral range of 9.15 GHz. The pump beam at 532 nm passed the crystal twice, as its back surface was high-reflective and its front surface was anti-reflective coated for this wavelength. The threshold power for the NOPO depended on the wave vector matching and the spatial mode filtering. Since we used different phase matching temperatures, the threshold power was between 70 and 130 mW. The crystal's temperature was controlled and stabilized with Peltier elements to a temperature around 60°C. The wave vector matching determined the efficiency of the process and the outgoing wavelengths. The relationship between wave vector matching and output wavelength was not linear, but evolves in steps,

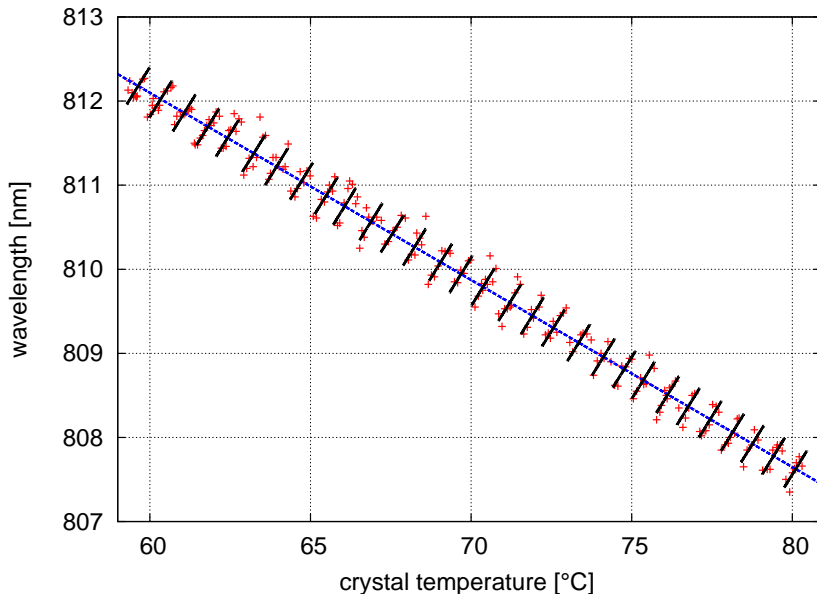


Figure 5.3: Wavelength tuning of the NOPO. Tuning of the NOPO’s crystal temperature resulted in an incremental wavelength tuning of the NOPO, illustrated here for 810 nm. As described in Section 3.4 the wavelength tuning of the NOPO was not smooth but mode hops and cluster jumps occurred, see also Reference [Sam12].

and is illustrated in Fig. 5.3 for 810 nm. Details about this incremental behaviour are described in Section 3.4 and can be found in [Eck91].

The output power of the outgoing beams depended on the pump power at 532 nm and on the crystal’s temperature (due to the wave vector matching). In Fig. 5.4 the output power for 810 nm (red) and the corresponding conversion efficiency (blue) is illustrated for two different temperatures of the crystal (dashed and solid lines). This measurement was made in the absence of any mode hops or cluster jumps. The conversion efficiency was calculated by

$$\eta_{\text{NOPO}} = \frac{N_{810}}{N_{532}} = \frac{P_{810} \times 810 \text{ nm}}{P_{532} \times 532 \text{ nm}}, \quad (5.1)$$

where N is the number of photons and P is the incoming or outgoing optical power. The 532 nm pump intensity used in the following experiments was typically around 700 mW. Therefore, the optical powers of the outgoing fields only differed due to different crystal temperatures and were around 100 mW for 1550 nm and 230 mW for 810 nm.

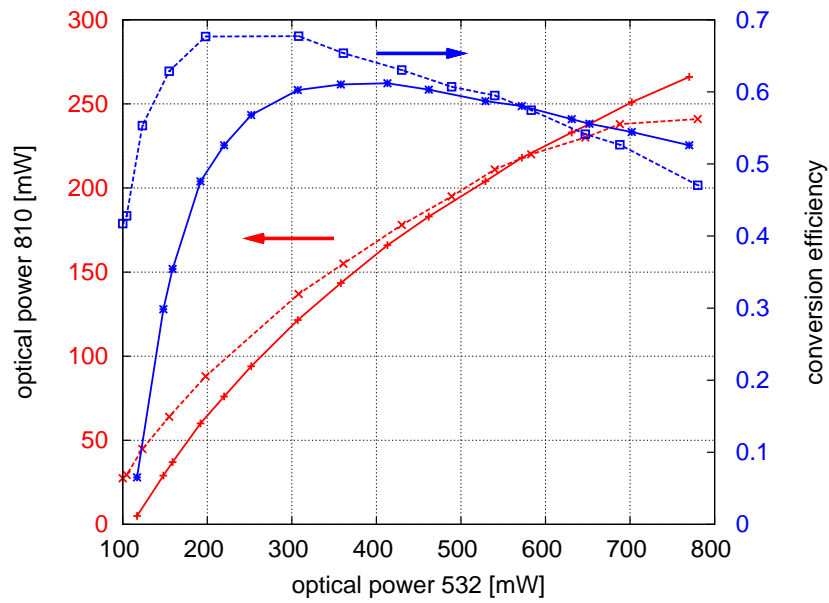
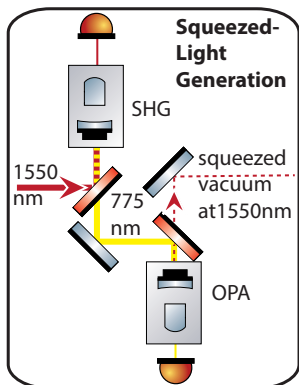


Figure 5.4: Output power and conversion efficiency of the NOPO. The blue curves show the conversion efficiency of the NOPO with respect to the incoming power at 532 nm, while the red curves depict the corresponding output power at 810 nm. The two different line styles represent two different phase matching temperatures and, thus, also two different outgoing wavelengths around 810 nm. Details can also be found in Reference [Sam12].

Table 5.1: Parameters of the two coupling mirrors for the SHG and OPA

Parameter	Mirror Sqz. Conv.	Mirror Ent. Conv.
Reflectivity at 1550 nm	90%	85%
Reflectivity at 775 nm	20%	97.5%

5.1.3 Squeezed-Light Generation



For the quantum up-conversion of squeezing and entanglement, two similar setups for the squeezing generation were used, which only differed in the reflectivities of the coupling mirrors and, thus, in the stabilization scheme. The theoretical background of the underlying nonlinear processes in this setup can be found in Chapter 3.

The generation of squeezed vacuum states at 1550 nm required a pump field at 775 nm, which was provided by second-harmonic generation (SHG) of the 1550 nm output beam from the NOPO. The OPA and the SHG both used the same type of nonlinear material, and the OPA generated a squeezed vacuum at 1550 nm again, by taking as input field the coherent 775 nm output of the SHG. Both devices consisted of a nonlinear PPKTP crystal and a coupling mirror, and were temperature stabilized to achieve good wave vector matching. The nonlinear crystal had a curved back surface with a high reflective coating and a flat front surface with an anti-reflective coating for 775 nm and 1550 nm.

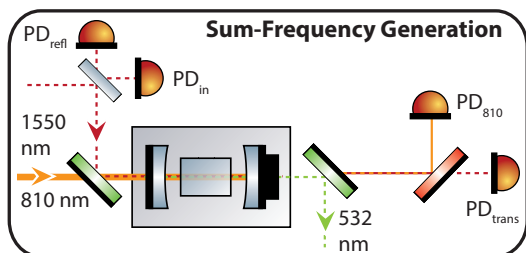
For the conversion of squeezed vacuum states we used an already existing setup, where the coupling mirror had a reflectivity of 90 % for 1550 nm and of 20 % for 775 nm. Therefore, the SHG cavity was locked with the 1550 nm beam, while the OPA cavity was not stabilized in length, but held on resonance manually. This setup was optimized for input powers around 1 W and could generate squeezed vacuum states with a quantum noise reduction of 12.3 dB [Meh11, Ebe13].

For the conversion of entanglement we used doubly-resonant devices, i.e. the coupling mirror had a reflectivity of 85 % for 1550 nm and 97.5 % for 775 nm. Hence, the SHG was also locked with 1550 nm, while the OPA was locked with 775 nm. Furthermore, the double-resonance led to a lower threshold power for the OPA (around 15 mW) and a higher conversion efficiency for pump powers around 100 mW for the SHG. The reflectivity values for both coupling mirrors can also be found in Table 5.1.

Table 5.2: Parameters of the two incoupling mirrors for the SFG

Parameter	Mirror Sqz. Conv.	Mirror Ent. Conv.
Reflectivity at 1550 nm	96%	91%
Reflectivity at 810 nm	96%	97%
Max. Conversion Efficiency	84.4%	89.2%
Corresponding pump power	71.5 mW	165 mW

5.1.4 Sum-Frequency Generation (SFG)



The quantum up-conversion was realized via sum-frequency generation utilizing a pump field at 810 nm. Due to energy conservation an incoming field at 1550 nm is up-converted to a field at 532 nm. This process is theoretically described in Sections 3.2 (classical) and 3.3 (quantum-mechanical). For the sum-frequency generation we used a nonlinear PPKTP crystal and two external mirrors, which can be seen in the picture above. The crystal was anti-reflective coated on both sides for all three wavelengths. The back mirror was high-reflective coated for 810 nm and 1550 nm and anti-reflective coated for 532 nm. For the two conversion experiments we used two different coupling mirrors.

For the up-conversion of squeezed vacuum states we used a mirror with a reflectivity of 96% for 810 nm and 1550 nm, which yielded a maximum conversion efficiency of 84.4% with a pump power of 71.5 mW [Sam13].

For entanglement up-conversion we used a mirror with a reflectivity of 97% for 810 nm and 91% for 1550 nm, to obtain a maximum conversion efficiency of 89.2% with a pump power of 165 mW. Both incoupling mirrors were high-reflective for 532 nm so that the converted field passed the crystal at most twice. The values for the two incoupling mirrors can also be found in Table 5.2. The cavity was stabilized in length with the PDH-technique using sidebands at 24.5 MHz on the 810 nm field, which were imprinted by an EOM. The error signal was measured in reflection of the cavity.

Before we performed the experiments we first measured the conversion efficiency of the SFG with the new coupling mirror. For this purpose we converted a signal field at 1550 nm, which was dim (2 mW) to ensure an undepleted pump field at 810 nm. The conversion efficiency was determined in two ways: a) by measuring the ratio of the outgoing photons over the incoming photons, which corresponded to a measurement of the incoming and outgoing light power scaled by the respective

wavelengths

$$\eta_{\text{SFG}, 532} = \frac{N_{532}}{N_{1550}} = \frac{P_{532} \times 532 \text{ nm}}{P_{1550} \times 1550 \text{ nm}} \quad (5.2)$$

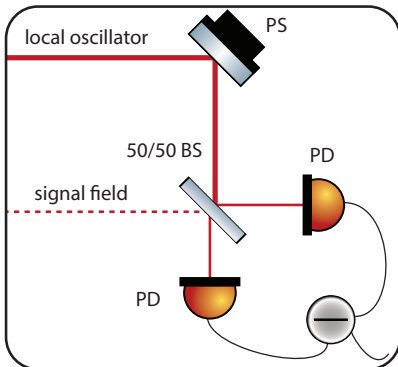
and b) by measuring the depletion of the 1550 nm field

$$\eta_{\text{SFG}, \text{depl}} = \frac{P_{1550, \text{refl}} + P_{1550, \text{trans}}}{P_{1550, \text{in}}} . \quad (5.3)$$

The reflected and transmitted parts of the field were measured by photo diodes in reflection and transmission, respectively. To measure the incoming light power, we used a 50/50 beam splitter in front of the SFG.

Since the first measurement method was susceptible to the measurement failures of the power meters, and the depletion method was sensitive to absorption of the crystal, we combined both measurements and fitted the data to theoretical values with a nonlinear cavity simulator program called *NLCS* written by Nico Lastzka [Las10]. The fitting procedure was executed by a *Python* script utilizing the *Nelder-Mead* fitting algorithm [Nel65] written by Aiko Samblowski [Sam12]. With this procedure we could determine the conversion efficiency of the SFG and its cavity parameters. The maximum conversion efficiency with the second incoupling mirror can be seen in Fig. 5.5. The red curve shows the theoretical values for $\eta_{\text{SFG}, 532}$ and the blue curve for $\eta_{\text{SFG}, \text{depl}}$. The blue data points represent the measured data for $\eta_{\text{SFG}, \text{depl}}$, while the red data points correspond to the measured data for $\eta_{\text{SFG}, 532}$, scaled by a correction factor for the power meter, which was calculated by the simulation program. The calculated reflectivities were $R = 94.5\%$ for 1550 nm and $R = 97.4\%$ for 810 nm, and varied slightly from the manufacturer's data. However, for different measurements with different wave vector matching the calculated values for the reflectivities stayed the same and showed thereby the reliability of the calculation.

5.1.5 Homodyne Detectors



The schematic of a homodyne detector is shown on the left side and explained in detail in Section 4.2. For the up-conversion experiments we used a custom-made homodyne detector for 532 nm, which utilized two silicon photo diodes (PD) from *Hamamatsu* (SI5971-3) with a quantum efficiency of 80 % and a custom-made homodyne detector for 1550 nm with two InGaAs photo diodes from *OSI Optoelectronics* (FC InGaAs-300) with a quantum efficiency

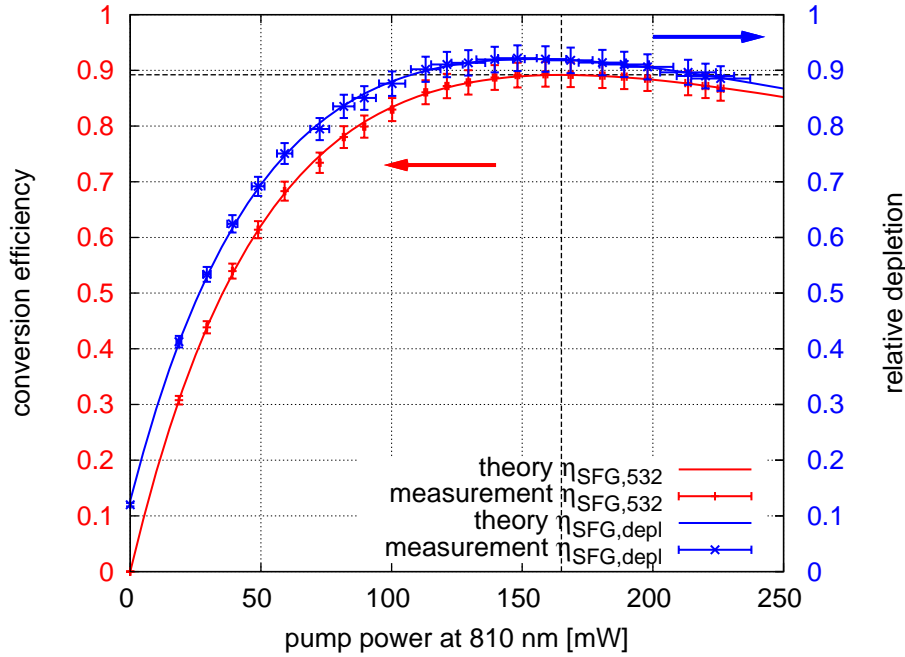


Figure 5.5: Conversion efficiency of the SFG. The red points represent the values for the conversion efficiency measured by the ratio of the outgoing photons over the incoming photons, scaled by a correction factor from the imperfect power meter. The blue points show the measurement of the relative depletion of the incoming 1550 nm field. We measured a maximum conversion efficiency of $89.2 \pm 2.5\%$ at a pump power of 165 mW at 810 nm. The theory curves were obtained by simulations with the nonlinear cavity simulator written by Nico Lastzka [Las10].

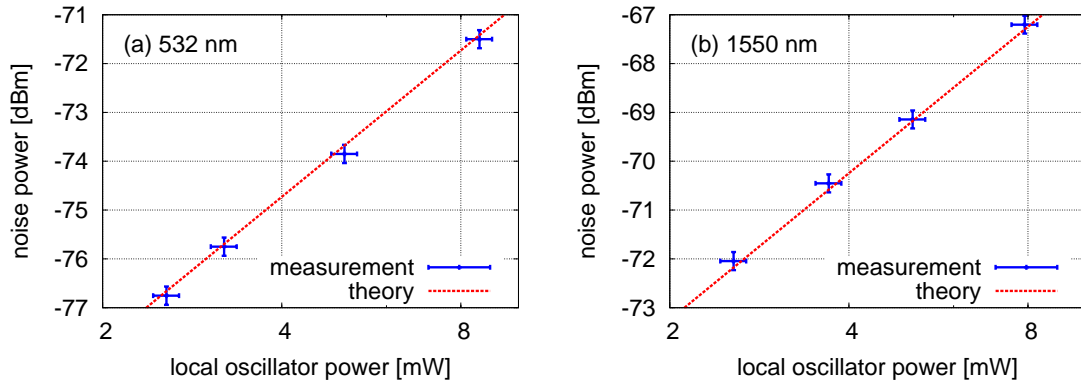


Figure 5.6: Characterization of the homodyne detectors. The linearity of the homodyne detectors at 532 nm and 1550 nm was checked by increasing the LO's power and measuring the corresponding output noise power (blue). By comparison with the theoretical values (red) the linearity is guaranteed over the optical power range of the LO used in the experiments (2–8 mW).

of also 80%. In Fig. 5.6 the linear behavior of the two homodyne detectors is depicted. The blue crosses represent the noise power measured with a specific local oscillator power by the homodyne detector. The red line shows the theoretical values, which correspond to a linear increase of the noise power. The homodyne detectors behaved linearly over the optical power range of the LO used in the experiments (2–8 mW).

5.2 Squeezing Conversion

The up-conversion of squeezed vacuum states of light from 1550 nm to 532 nm was accomplished with an external setup for the generation of squeezed vacuum states at 1550 nm. This means that the 1550 nm output beam from the NOPO was sent through a fiber to a SHG and an OPA to the other side of the optical table and the resulting squeezed vacuum field was inserted to our experiment by a flip mirror. The squeezed vacuum field at 1550 nm was overlapped with the pump field at 810 nm and sent into the SFG. The up-converted squeezed vacuum field at 532 nm, which left the SFG through the back side of the crystal, was measured with a homodyne detector. The homodyne detector's LO was provided by the same source as the pump field for the NOPO (cf. Fig. 5.2), i.e. the LO and the squeezed vacuum field matched in frequency automatically due to the energy conservation of all involved nonlinear processes.

Results

The result of the up-conversion of squeezed vacuum states from 1550 nm to 532 nm is illustrated in Fig. 5.7, showing the squeezing measurement with the 532 nm homodyne detector. We measured at a sideband frequency of $f = 8$ MHz, with a resolution bandwidth of $\Delta f = 300$ kHz and a video bandwidth of $v = 30$ Hz. The traces are normalized to the measured vacuum noise, which was obtained by blocking the input signal before the homodyne detector. We detected a nonclassical noise reduction of 1.5 dB below the vacuum noise and a corresponding anti-squeezing of 2.4 dB, without any corrections for the homodyne detector's dark noise. By subtracting the homodyne detector's dark noise, which was 10 dB below the shot noise, we inferred 1.7 dB squeezing and 2.6 dB anti-squeezing. These values correspond to a 4 dB pure squeezed state at 1550 nm with 47% optical loss. The individual loss channels are listed in Table 5.3.

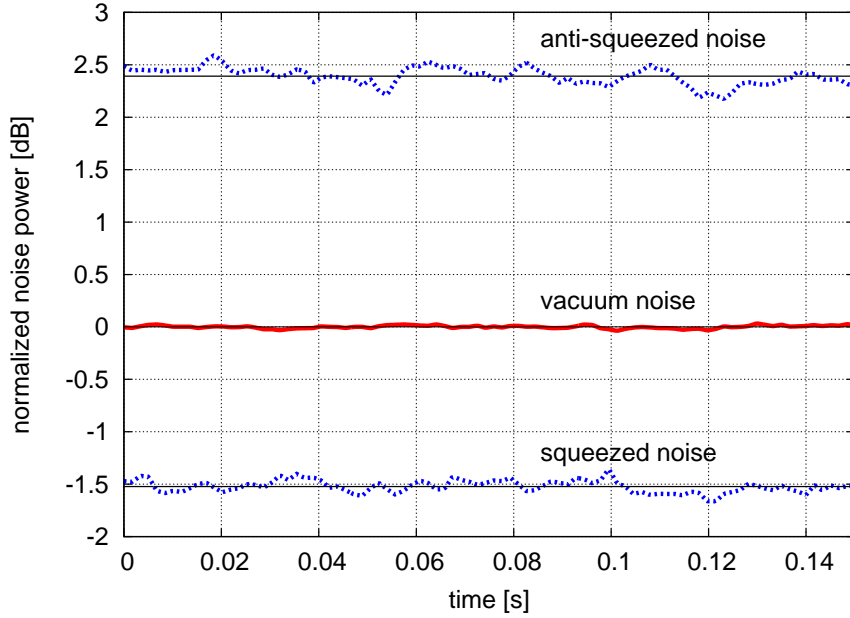


Figure 5.7: Measurement of the up-converted squeezed vacuum states at 532 nm. The squeezed and anti-squeezed quadratures were measured with the 532 nm homodyne detector by manually varying the phase between the signal and the LO (blue). The vacuum noise (red) was measured by blocking the signal before the detector. From the figure we read a nonclassical noise reduction of 1.5 dB below the vacuum noise and a corresponding anti-squeezing of 2.4 dB at a sideband frequency of $f = 8$ MHz. All traces are normalized to the vacuum noise power, but not corrected for the detector’s dark noise.

Table 5.3: Optical efficiency for the squeezing measurement

Loss channel	Efficiency
Escape efficiency of OPA	96%
Mode matching of SFG	99.4%
Conversion	75%
Propagation to homodyne detector	97%
Visibility on homodyne detector	96%
Quantum efficiency of photodiodes	80%
Overall	53%

Table 5.4: Improvements for squeezing up-conversion

Improvement	New Value
Initial squeezing value	12 dB
Escape efficiency of OPA	97.7%
Conversion efficiency	90%
Quantum efficiency of photo diodes	90%

Discussion

With the presented scheme of quantum up-conversion via sum-frequency generation it was possible to obtain a squeezed vacuum state at 532 nm with a noise reduction of -1.5 dB, which is the highest measured squeezing value at this wavelength. Two main factors limited the measured squeezing to -1.5 dB: the initial squeezing was only 4 dB and the conversion efficiency was 75%. Since the external experimental setup for the squeezing generation was not optimized for an input power of about 100 mW, we only had a 4 dB pure squeezed state at 1550 nm for the quantum frequency conversion, instead of more than 10 dB that the setup could in principle provide [Ebe13]. By using a new setup, with a SHG and an OPA that were designed for input powers of about 100 mW (i.e. their coupling mirrors had different reflectivities), we solved this problem for the conversion of entangled states of light. Intertwined with this issue is the wavelength dependence of the conversion efficiency of the SFG and SHG, especially for low light powers. This means that both the conversion efficiency of the SFG, and the conversion efficiency of the SHG providing the pump field for squeezing generation, depended strongly on the wavelengths from the NOPO. Therefore, we had to find a trade-off between a strong pump field for the OPA, which would generate higher initial squeezing, and a high conversion efficiency of the SFG. Finally, we ended up with a conversion efficiency of 75% for the SFG (instead of 84.4%, which was the highest measured value) and 18 mW of optical power for the OPA's pump field, which generated a 4 dB squeezed vacuum state at 1550 nm, before losses.

In an improved setup we could also increase the SFG's conversion efficiency by changing the incoupling mirror. If the reflectivity for 810 nm is increased and the reflectivity for 1550 nm is decreased, the conversion efficiency should be around 90% for reasonable pump powers (below 200 mW). By utilizing photo diodes with higher quantum efficiency ($> 90\%$), the detection efficiency of the squeezed states will be strongly enhanced and lead thus to a higher detectable squeezing value. With all possible improvements (listed in Table 5.4) in the loss channels and to the initial squeezing value, it should be possible to detect squeezed vacuum states at 532 nm of about 6 dB.

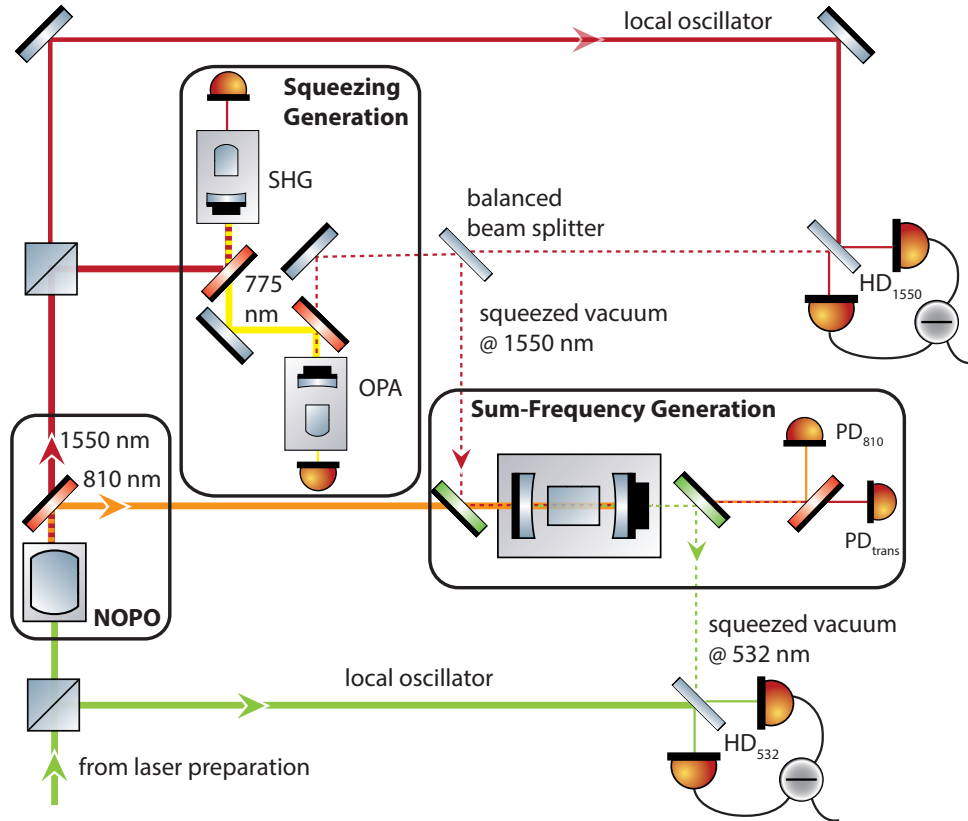


Figure 5.8: Experimental setup of entanglement conversion. In addition to the experimental setup for squeezing conversion, this setup included an additional balanced beam splitter to generate an entangled state at 1550 nm and the homodyne detector HD_{1550} , which was used for measuring entanglement between 532 nm and 1550 nm.

5.3 Entanglement Conversion

For the up-conversion of entangled states of light, we added a 50/50 beam splitter to the 1550 nm squeezed vacuum path (illustrated in Fig. 5.8), to obtain two entangled light fields at 1550 nm in the two output ports (cf. Section 2.9.2). One output was sent directly to a balanced homodyne detector HD_{1550} , while the other was up-converted via SFG to 532 nm. The up-converted field was detected with the balanced homodyne detector HD_{532} (see faint part of Fig. 5.2). The signal of the homodyne detector HD_{1550} was split, and one part was used to check the measured quadrature of HD_{1550} . The other part was sent to a subtraction/addition device, which added or subtracted the signals of HD_{1550} and HD_{532} .

In contrast to the squeezing up-conversion experiment, we used a different in-coupling mirror for the SFG. Thereby, we could achieve a maximum conversion efficiency of 89.2% (cf. Section 5.1.4). Furthermore, we used a SHG and OPA that

were designed for generating 10 dB squeezed states at 1550 nm with low input powers (~ 100 mW).

Results

In Fig. 5.9 the subtraction and addition of the two homodyne detectors HD₁₅₅₀ and HD₅₃₂ are shown. The homodyne detector at 532 nm is ramped periodically to measure all quadratures, while the homodyne detector at 1550 nm is controlled manually to measure the X quadrature (red trace) or the P quadrature (blue curve). The black traces in the two figures shows the vacuum noise of the subtraction and addition of the two homodyne detectors. All traces were measured at a sideband frequency of $f = 8$ MHz with a resolution bandwidth of $\Delta f = 300$ kHz and a video bandwidth of $v = 300$ Hz. The two figures illustrate the success of the entanglement conversion, which can be verified by the Duan criterion (cf. Section 2.9.1):

$$\mathcal{I} = \text{Var}(X_{1550} - X_{532}) + \text{Var}(P_{1550} + P_{532}) \leq 4. \quad (5.4)$$

The subtraction and addition measurements both fulfill this criteria for entanglement, since both measurements show the same values (0 dB for the addition of the P quadratures and -3.4 dB for the subtraction of the X quadratures) and the Duan value \mathcal{I} reads

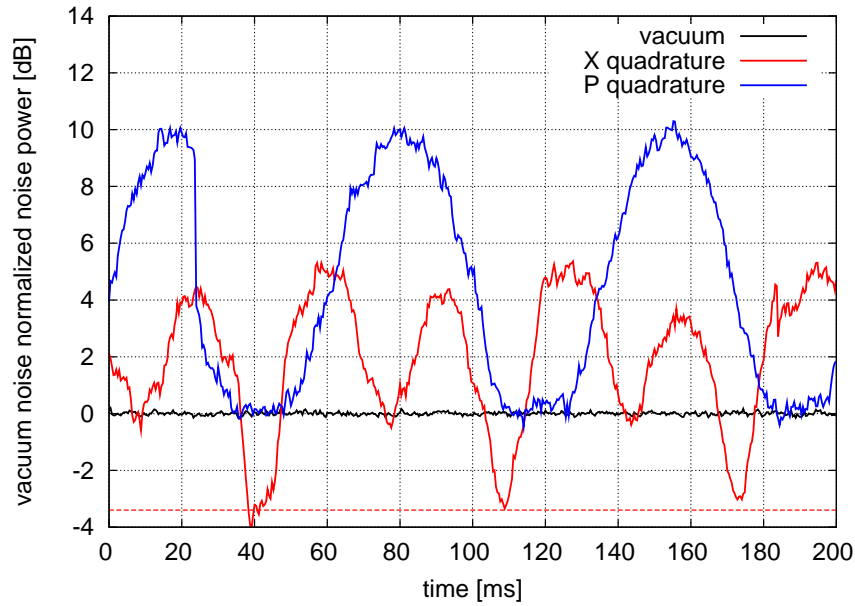
$$\mathcal{I} = 0.9 + 2 = 2.9 \leq 4, \quad (5.5)$$

which corresponds to an entanglement of -1.4 dB. Thus, an entangled state at 1550 nm was successfully up-converted to an entangled state between 1550 nm and 532 nm.

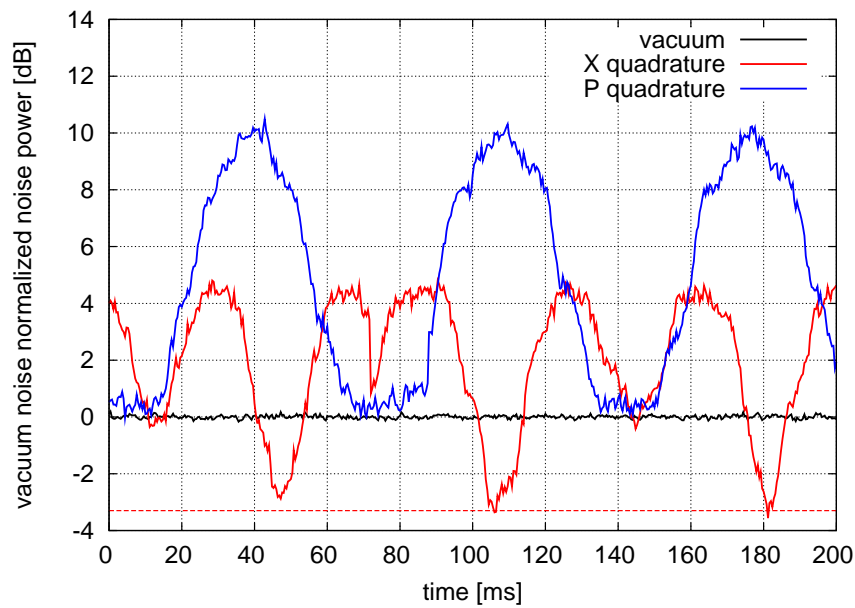
With this setup we also measured squeezing conversion, though with the additional balanced beam splitter, which introduced 50% loss. For this purpose we took data only from the homodyne detector at 532 nm, under the same conditions as for the entanglement measurement. The data is depicted in Fig. 5.10. From the figure we see a noise reduction of 1.3 dB and a corresponding anti-squeezing of 7.2 dB, which correspond to an initial squeezing of 12.1 dB and 72.5% optical loss. If we subtract the optical loss from the balanced beam splitter (50%) and the optical loss due to the imperfect escape efficiency of the OPO (97.7%), we are left with 44% optical loss for the homodyne detector and the conversion efficiency.

Discussion

The squeezing measurement shows that the part of the entangled state at 1550 nm, which was sent to the SFG suffered from 44% optical loss. Since we could not put



(a) Subtraction of homodyne detectors, output signal



(b) Addition of homodyne detectors, output signal

Figure 5.9: Results of entanglement measurement between 1550 nm and 532 nm. The traces were normalized to the vacuum noise (black) without any correction for dark noise. We see a quantum noise reduction of -3.4 dB in the X quadrature and, as expected, of 0 dB in the P quadrature for the subtraction of the homodyne detectors at 532 nm and 1550 nm (a) as well as for the addition of them (b). Data was taken at a sideband frequency of $f = 8$ MHz with a resolution bandwidth of $\Delta f = 300$ kHz and a video bandwidth of $\nu = 300$ Hz.

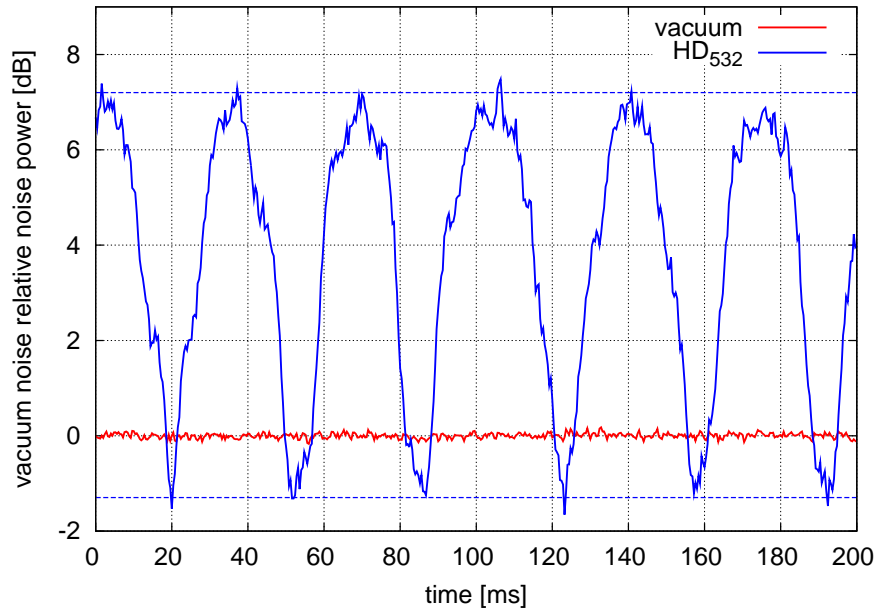


Figure 5.10: Result of squeezing conversion with an additional balanced beam splitter. The traces were normalized to the vacuum noise (red). The blue trace shows the data from the homodyne detector at 532 nm when the phase between squeezed vacuum state and local oscillator was varied periodically. We measured a squeezed state with a noise reduction of -1.3 dB and a corresponding anti-squeezing of 7.2 dB. These values correspond to an initial squeezing of 12.1 dB and 72.5% optical loss. Data was taken at a sideband frequency of $f = 8$ MHz with a resolution bandwidth of $\Delta f = 300$ kHz and a video bandwidth of $\nu = 300$ Hz.

the homodyne detector at the Brewster angle due to space limitations, its quantum efficiency was about 75 % for this measurement. Considering also the visibility of the homodyne detector HD₅₃₂ (97%), we can calculate the SFG's conversion efficiency to be 80% for the entanglement conversion measurement.

As before, when we discussed the up-conversion of squeezed vacuum states, we encounter the problem that the SFG's conversion efficiency strongly depended on the outgoing wavelengths of the NOPO. However, the SHG's conversion efficiency and the gain of the OPA also depended on the incoming wavelengths. Therefore, we had to find wavelengths provided by the NOPO that correspond to a good efficiency in all devices, and consequently could not use the highest measured value of 89% for the SFG's efficiency. Nevertheless, we could use a highly squeezed state at 1550 nm and did demonstrate entanglement between 1550 nm and 532 nm via quantum up-conversion. If we were able to use 90 % conversion efficiency for the SFG, the same initial squeezed state at 1550 nm of 12 dB, homodyne detectors with quantum efficiencies of 90% for 532 nm and 95% for 1550 nm and with 99 % visibility, we could have measured entanglement between 1550 nm and 532 nm of 2.1 dB. In a perfect setup without loss, a maximum 3 dB entanglement is achievable, since the initial entanglement was generated with one squeezed state and a balanced beam splitter.

5.4 Conclusion

In this chapter I presented the successful demonstration of quantum up-conversion via sum-frequency generation by means of the up-conversion of a squeezed vacuum state from 1550 nm to 532 nm and the up-conversion of one part of an entangled state to establish entanglement between 1550 nm and 532 nm. The highest known squeezing value at 532 nm of -1.5 dB, with an corresponding anti-squeezing of 2.5 dB and entanglement between 1550 nm and 532 nm with a Duan value of -1.4 dB were measured. The technique of quantum up-conversion via sum-frequency generation can potentially generate non-classical states of light in the visible wavelength regime with high efficiency. However, in both experiments we found that the wavelength dependence of the single devices made truly efficient quantum up-conversion difficult. In particular, the wavelength dependence of the conversion efficiency of the SFG in combination with the stepwise wavelength tuning of the NOPO was crucial. However, this obstacle can be overcome by a setup which can provide more pump power, so that the wavelength dependence of the squeezing generation is no longer a limiting factor. By using photo diodes with a higher quantum efficiency the detected squeezing and entanglement factors should be easily increased.

The successful demonstration of quantum up-conversion paves the way towards quantum states at any desired wavelength, since by this technique non-classical states of light can be generated highly efficient in the visible wavelength regime. Of special interest are squeezed vacuum states of light, which can be used for quantum imaging, quantum spectroscopy or gravitational wave detection. Now that the generation of these states is extended to the visible wavelength regime, they could potentially be used to improve the sensitivity of new detectors operating at shorter wavelengths.

A source of entanglement between two different wavelengths in the infrared and in the visible wavelength regime represents a key resource for future quantum memories as a basis for quantum repeaters. These devices need to bridge the two wavelength regimes of quantum information transfer (1550 nm) and quantum storage (500-800 nm).

Entanglement Distribution by Separable States

Distribution of entanglement between macroscopically separated parties is crucial for future quantum information networks since entanglement is a fundamental resource for quantum information processing [Kim08, Hor09]. Most quantum protocols are intended to be executed between remote parties, which are commonly called ‘Alice’ and ‘Bob’. Usually the distribution of bipartite entanglement is performed by generating the entangled modes at Alice’s place and sending one of the modes to the distant party Bob. Thereby the mode sent from Alice to Bob is obviously entangled with the mode kept by Alice. However, Cubitt *et al.* [Cub03] showed in 2003, that if more than two modes are involved, bipartite entanglement can also be distributed by sending fully separable states. This remarkable and seemingly paradoxical protocol is made possible by a specific structure of quantum correlations within an underlying state of three modes A, B, and C. The protocol demands the state to be separable with respect to the B|AC and C|AB splittings and to be inseparable with respect to the A|BC splitting. The original protocol by Cubitt *et al.* as well as further analysis done in [Chu12, Kay12] considered discrete variables. Mišta and Korolkova recently showed that entanglement distribution by separable states is also possible for continuous variables [Miš08, Miš09].

In the following chapter I will present the experimental realization of distributing continuous variable entanglement by separable states. In Section 6.1 the underlying protocol is introduced. Section 6.2 describes the requirements for the three-mode state, which makes the entanglement distribution by separable states possible. The experimental setup is illustrated in Section 6.3, while Section 6.4 describes the measurement procedure. Section 6.5 presents the experimental results. The following discussion in Section 6.6 includes considerations about possible error sources, while

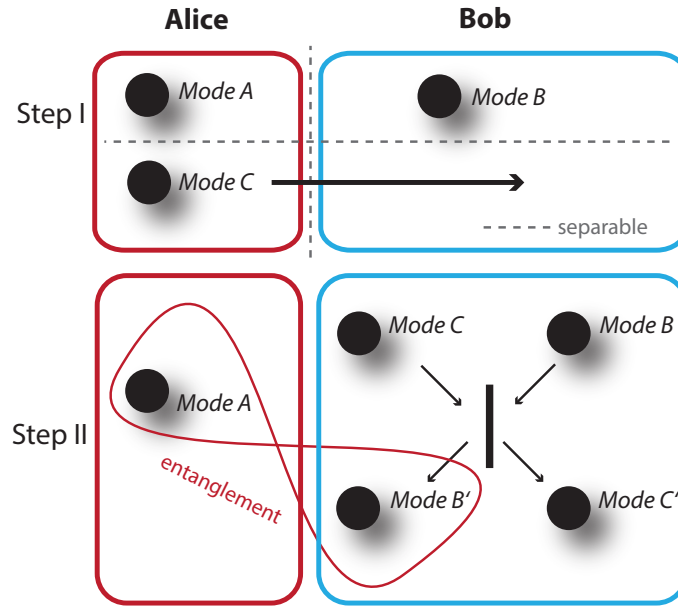


Figure 6.1: Principle of entanglement distribution by separable states. In the beginning Alice possesses the two separable modes A and C. Both modes are also separable with respect to Bob’s mode B. Alice sends mode C to Bob and he combines his mode B with the received mode C. Finally, Alice and Bob share an entangled system $A|B'$, which can be traced back to the initial entanglement for the $A|BC$ splitting.

Section 6.7 summarizes the results.

The results of this chapter have recently been published in [Vol13].

6.1 Protocol of Entanglement Distribution by Separable States

The principle of entanglement distribution by separable states is depicted in Fig. 6.1. In the beginning Alice possesses the two separable modes A and C, while Bob possesses the mode B, which is separable to Alice’s modes. In a first step Alice sends the ancilla mode C, which is neither entangled with mode A nor with mode B, to Bob. To obtain two-mode entanglement Bob mixes his modes B and C in the second step of the protocol. One output mode is then discarded, while the other one turns out to be entangled with mode A. The entanglement between modes A and B can be traced back to the initial separability properties of the underlying three-mode Gaussian state, which is prepared by an external source. For the protocol to work the state must be separable with respect to the $B|AC$ and $C|AB$ splittings and inseparable with respect to the $A|BC$ splitting. According to the classification

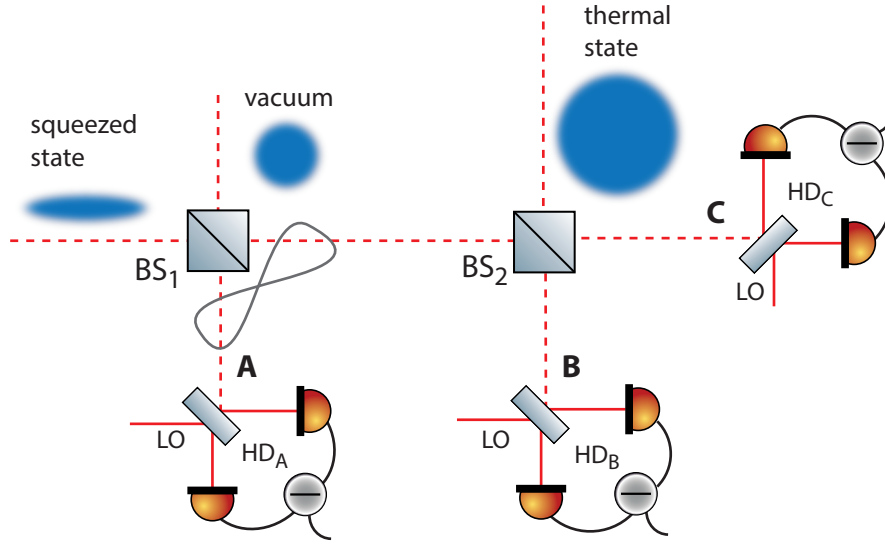


Figure 6.2: State preparation scheme of the three-mode state. The required three-mode state is prepared by overlapping a squeezed state, a vacuum state and a thermal state at two balanced beam splitters BS₁ and BS₂ and measured with the homodyne detectors HD_A, HD_B, and HD_C, respectively.

introduced in [Gie01], we therefore need a three-mode Gaussian entangled state belonging to Class III. The preparation of such a three-mode state is illustrated in Fig. 6.2. The preparation starts with a squeezed state, which interferes with a vacuum state at the balanced beam splitter BS₁. The beam splitter output A is sent to the homodyne detector HD_A, while the other output is superimposed with a thermal state at a second balanced beam splitter BS₂. Its outputs B and C are sent to the homodyne detectors HD_B and HD_C, respectively. The separability properties of the three-mode state (ABC) are checked by a tomographic reconstruction of the full three-mode covariance matrix with the homodyne detectors HD_A, HD_B, and HD_C. In the following section we will investigate the influence of the squeezing strength and the variance of the thermal state on the properties and applicabilities of the three-mode state.

6.2 Requirements for the three-mode state

As we have seen in the previous section the three-mode state required for the entanglement distribution by separable states has to be inseparable with respect to the A|BC splitting and separable with respect to the B|AC and C|AB splittings. That means that the PPT value (cf. Section. 2.9.1) for the A|BC splitting has to be below 1 ($\text{PPT}_A < 1$), and for the other two splittings above or equal to 1 ($\text{PPT}_B \geq 1$ and

$\text{PPT}_C \geq 1$). These specifications for the three-mode state give us the requirements for the squeezed and the thermal state which we have to use for the state preparation. Generally, the variance of the thermal state has to be sufficiently large to demolish the entanglement which is generated by the superposition of a squeezed vacuum state and a vacuum state at beam splitter BS_1 (cf. Fig. 6.2). To investigate the effects of the squeezed state and the thermal state, a simulation with *Python* (see Appendix A) was made, which reproduced the three-mode state preparation and calculated the resulting separability properties. In principle the following parameters within our experimental setup can be varied: the variance of the thermal state as well as the variances of the squeezed and anti-squeezed quadratures of the squeezed state. The latter two can be changed independently of each other by variation of the pump power of the squeezed-light source and by variation of additional optical losses.

For the simulations we make the approximation that the variance of thermal state is equal in all quadratures. Note that without additional optical loss in the path from the state preparation to the homodyne detectors (which we assume for the simulations) the PPT_B value always equals the PPT_C value. Furthermore, with our setup the PPT_A value is always below 1 as long as we use a squeezed state as an input state. Thus, we will not consider this value in the following.

In Fig. 6.3 the PPT_B values with respect to the variance of the thermal state and the variance of the squeezed state are shown. For the simulation in this figure we assumed that there is no optical loss affecting the squeezed state. The figure shows that in this case the PPT_B value cannot be above 1 and thus the three-mode state does not fulfill the requirements.

In Fig. 6.4 (a) the effect of the optical loss applied to the squeezed input state is illustrated. We used a 20 dB thermal state with a symmetric variance as an input state and varied the optical loss and the variance of the initial squeezed state. Surprisingly, the figure shows that independent of the squeezed state's variance 33.3% optical loss is always required to obtain PPT_B values above 1. In Fig. 6.4 (b) we assumed a -10 dB squeezed state and varied the optical loss applied to the squeezed state and the variance of the thermal state. Since the black threshold line converges asymptotically to 33.3%, this figure also shows that the threshold of 1 cannot be achieved with less than 33.3% loss, even for an arbitrary large variance of the thermal state. This is exactly the threshold for which the bipartite entangled state, generated by the superposition of a squeezed and a vacuum state at the first balanced beam splitter, is no longer Einstein-Podolsky-Rosen entangled [Ebe11]. Einstein-Podolsky-Rosen entangled states are a subclass of general entanglement, exhibiting stronger quantum correlations. Indeed, the properties of our three-mode state show that these correlations are so strong that the entanglement in the bipartite

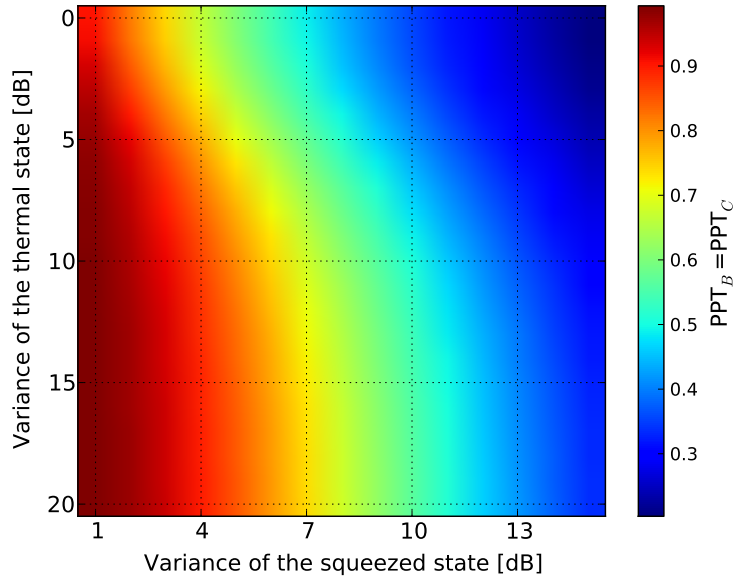


Figure 6.3: PPT_B value with respect to the variance of the initial states. No optical loss is assumed. Thus, the PPT_B value cannot exceed 1 and the three-mode state cannot be separable with respect to the B|AC splitting.

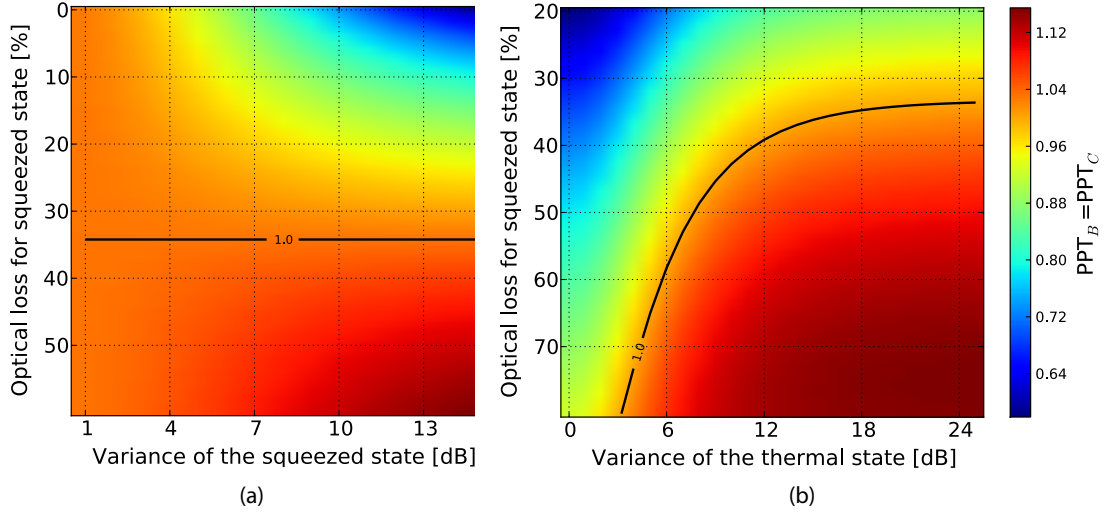


Figure 6.4: PPT_B value for different variances of the input states. (a) The thermal state's variance is set to 20 dB. The variance of the squeezed state and the optical loss which is applied to the squeezed state are varied. The black line corresponds to a PPT value of 1 and shows that regardless to the variance of the squeezed state, the optical loss has to be greater than 33.3%. (b) Here, the pure squeezed state's variance is set to 10 dB, while the variance of the thermal state and the optical loss are varied. The threshold of 33.3% optical loss is also visible in this figure by the black line marking a PPT value of 1.

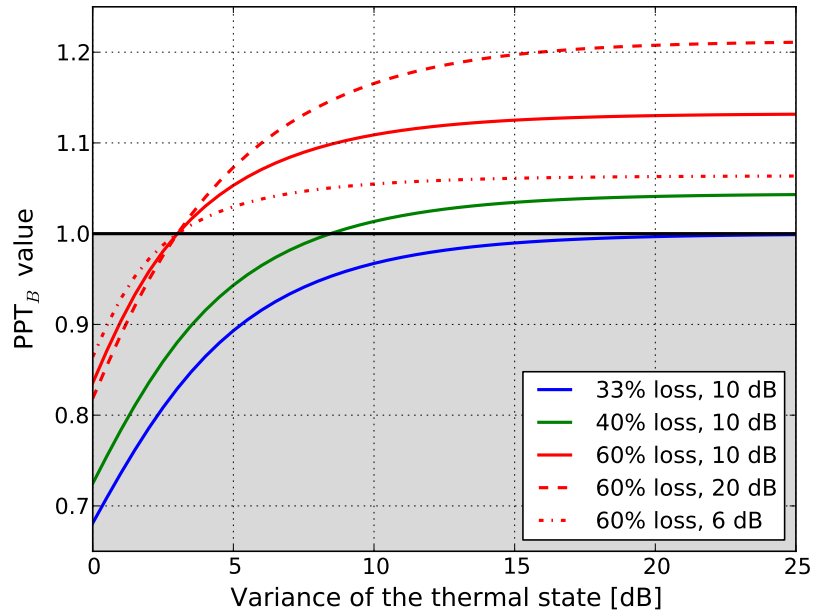


Figure 6.5: PPT_B value with respect to the thermal state's variance. The solid curves correspond to a 10 dB initial squeezed state. They show that for more optical loss the required variance of the thermal state can be lower. The red curves show that for a certain amount of optical loss the threshold of 1 (for a separable state) is not dependent on the initial amount of squeezing.

splittings cannot be prevented by classical noise. Furthermore, Figure 6.4 (b) shows that for more optical loss the variance of the thermal state can be smaller than for less optical loss. However, with more optical loss the entanglement, which can be distributed by separable states, becomes also less. Therefore, one has to find a compromise between a reasonable amount of distributed entanglement and a thermal state with an experimentally feasible variance.

Figure 6.5 shows a summary of the aspects considered before. Here, the PPT_B value is shown with respect to the variance of the thermal state for different initial squeezed states and different optical loss. All solid lines correspond to a 10 dB initial squeezed state. For 60% loss the curves for 20 dB and 6 dB are also shown in dotted lines (red curves). They illustrate the fact that for a certain amount of optical loss the initial squeezing value does not determine the required variance of the thermal state; though, as mentioned before, it determines the amount of the distributed entanglement.

Altogether, we now know that for the distribution of entanglement by separable states we need more than 33.3% optical loss applied to the initial squeezed state, the

variance of the squeezed state determines the amount of the distributed entanglement and the variance of the thermal state has to be sufficiently large to demolish the initial entanglement created at the first beam splitter.

6.3 Experimental Setup

The experimental setup for entanglement distribution by separable states is depicted in Fig. 6.6. In this section we will describe the setup step by step and describe the individual stages in detail.

6.3.1 Laser Source

The laser source was a Neodymium-doped Yttrium Aluminum Garnet (Nd:YAG) continuous-wave solid-state laser from *Inno-light* (model Diabolo). This device generated a single-mode output field at 1064 nm of about 300 mW light power and the frequency doubled field at 532 nm of about 500 mW light power using second harmonic generation.

The green light field served as the pump field for the squeezed-light sources (see next subsection). For this purpose the field was split in two parts by a half-wave plate and a polarizing beam splitter (PBS). This combination was often used for tunable power splitting throughout the experiment.

The infrared light field passed an electro-optical modulator (EOM), which phase modulated the light field at a frequency of 30 MHz. The sidebands were used to stabilize the length of all cavities in the experiment with the Pound-Drever-Hall (PDH) locking technique [Bla01]. The infrared light field was used to stabilize the cavities' length of the squeezed-light sources, to align the beams at the balanced beam splitters and homodyne detectors, and as the local oscillator for the homodyne detectors. To utilize as a local oscillator the light field was filtered by a mode cleaning ring cavity (MC) with a linewidth of 55 kHz. This device ensured that the light field was shot-noise limited at frequencies above 5 MHz and that its mode was spatially filtered.

The homodyne detector HD_E also belonged to the laser preparation stage since it provided the random noise for the thermal state generation by measuring vacuum fluctuations.

6.3.2 Squeezed-Light Sources

The device for the generation of the squeezed and the thermal state was a type I optical parametric amplifier (OPA). For details of the generation schemes see

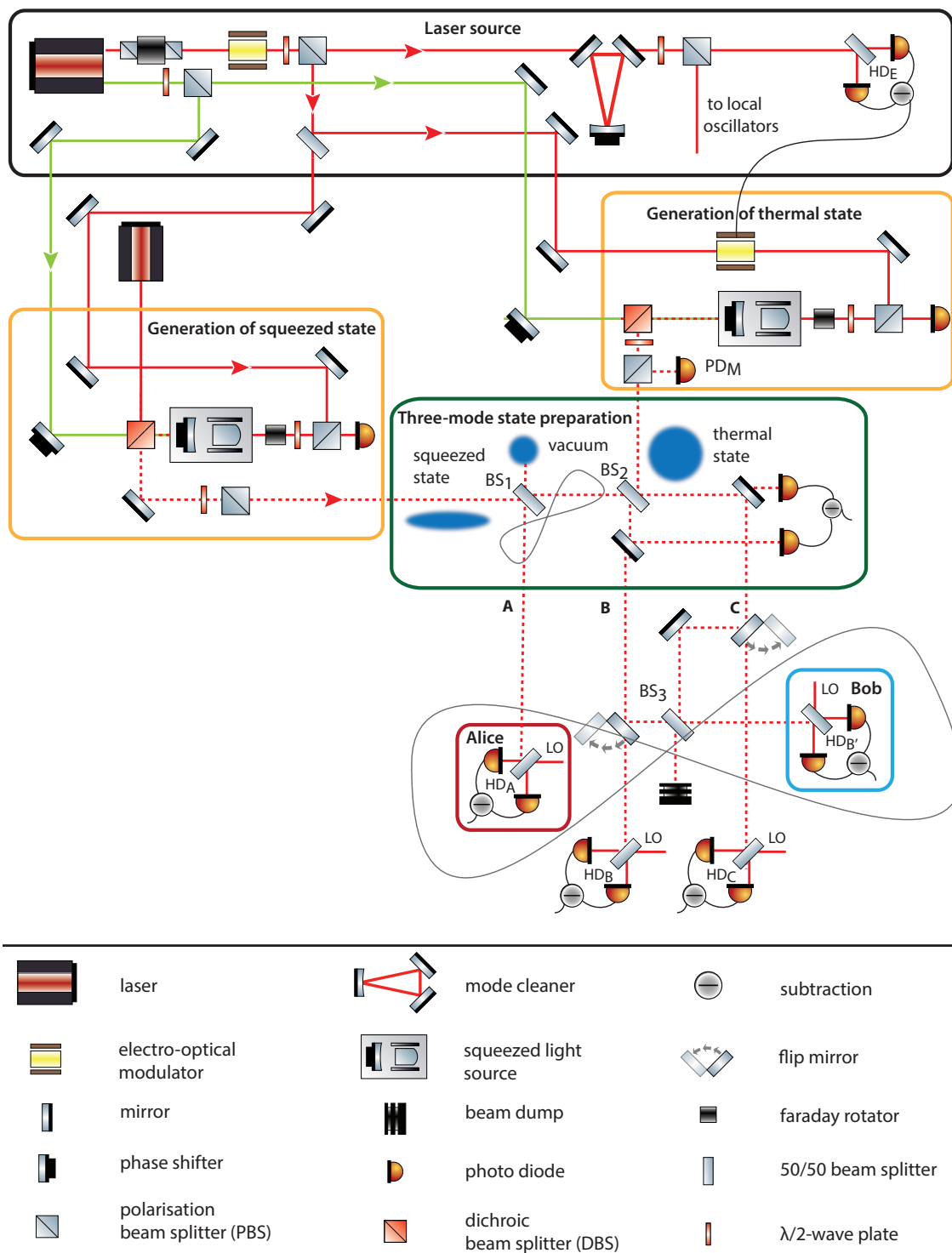


Figure 6.6: Experimental setup for the entanglement distribution by separable states. Details are provided in the text.

Sections 4.1 and 4.4. As the squeezed-light sources were already built up and used for former experiments, details about their specifications can be found in [Che07, Hag10a].

The standing-wave cavity of such a squeezed-light source was built up of a $\chi^{(2)}$ nonlinear crystal with one curved end surface and a mirror, which was mounted on a piezo-electric transducer (PZT). The mirror had a reflectivity of 94% for 1064 nm and of 25% for 532 nm. The crystal consisted of 7% Magnesium oxide doped Lithium Niobate ($\text{MgO}:\text{LiNbO}_3$) and had dimensions of $2.5 \times 5 \times 6.5 \text{ mm}^3$. The flat incoupling surface had an anti-reflective coating for 1064 and 532 nm, while the back surface was curved and its reflectivity for both wavelengths was greater than 99.96%. This resulted in a finesse of 100 for 1064 nm and of 4.3 for 532 nm. The free spectral range of the cavity was determined by the length of the cavity and yielded 4 GHz. The outgoing squeezed-light field was spatially separated from the reflected pump field by a dichroic beam splitter (DBS). With a $\lambda/2$ wave plate and a PBS we could add additional optical loss to adjust the squeezing variances.

The phase matching of the two light fields was achieved by type I phase-matching (cf. Sec. 3.6). Therefore, the crystal's temperature was actively stabilized by Peltier elements to a temperature of about 60° C.

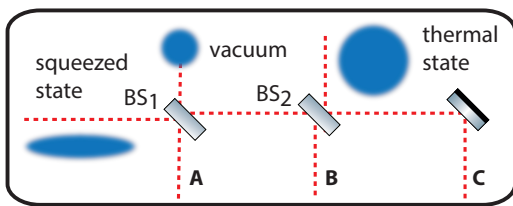
For stabilizing the length of the cavity a control field at 1064 nm was coupled from its back side. The back reflected light passed the Faraday rotator, the $\lambda/2$ wave plate, and the PBS and was detected by a photo diode. Since the control field contained sidebands at 30 MHz, the alternating current (AC) of the photo detector was demodulated at this frequency. After low pass filtering the PDH error signal was used to control the cavity's length. To generate a stable amplitude or phase squeezed vacuum state the phase of the pump field was also actively controlled. For this purpose the photo detector's AC output was demodulated with a phase shift of 90° with respect to the demodulation phase of the lengths control's error signal. The resulting error signal for stabilizing the phase drove a *phase shifter* (PS), i.e. a mirror mounted on a piezo electric transducer (PZT).

For the generation of the squeezed state as the initial input state the OPA provided amplitude squeezed vacuum states. To stabilize the phases of the phase gates and homodyne detectors, a single sideband (cf. Sec. 4.3) was imprinted to the squeezed-light field. The single sideband was generated by a second laser from *Inno-light* (model: Mephisto) which was frequency stabilized to the main laser source with a frequency shift of 15 MHz.

For the generation of the thermal state the second OPA provided phase squeezed states, whose phase quadrature was enhanced by an additional noise modulation of the control field. For this purpose the cavity had to be stabilized to amplification of the amplitude. That stabilization was more difficult to achieve than the stabilization

of the control beam's phase to generate amplitude squeezed states since the stabilization scheme used the detected amplitude of the control field. To have a better control of the stabilization we added the monitor photo detector PD_M in reflection of a PBS. The imperfection of the PBS's transmission was sufficient to monitor the amplitude of the control field. The measurements were thus only performed when the detected amplitude was stable. Details about the thermal state generation can be found in Section 4.4.

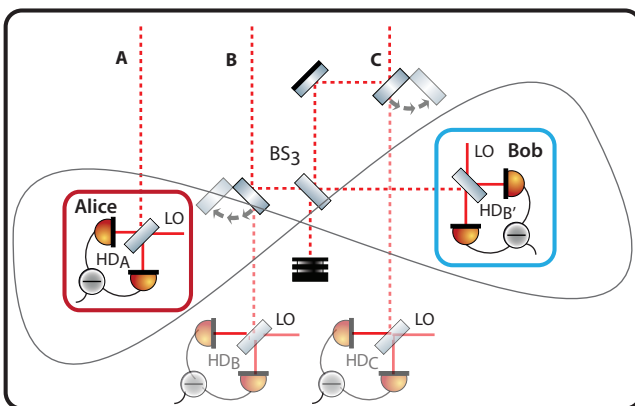
6.3.3 Three-Mode State Preparation



For the three-mode state preparation the squeezed state was superimposed with a vacuum state at the balanced beam splitter BS_1 . One output was sent to Alice's homodyne detector HD_A , while the other output

was overlapped with the thermal state on the second balanced beam splitter BS_2 . Its two outputs were detected with the homodyne detectors HD_B and HD_C . With those three homodyne detectors the three-mode state was checked for its separability properties. They had a quantum efficiency about $90\% \pm 5\%$ and their visibilities were measured before each measurement. The local oscillators had a total light power of 2 mW each. The homodyne detectors were locked to a certain quadrature using the single sideband (cf. Sec. 4.3). With the data of the homodyne detectors the covariance matrix of the three-mode state could be reconstructed (see Section 6.4.1) and by applying the PPT criterion the requirements for the three-mode state were checked.

6.3.4 Entanglement Distribution



If the three-mode state was as required, two flip mirrors were used to superimpose modes B and C at Bob's balanced beam splitter BS_3 . One output was discarded, while the other one was detected by Bob's homodyne detector HD_D . The phase of the beam splitter was set to the opposite phase of phase gate BS_2 to generate entanglement between Alice and Bob and was controlled manually. With Alice's detec-

tion, the entanglement was distributed between Alice and Bob.

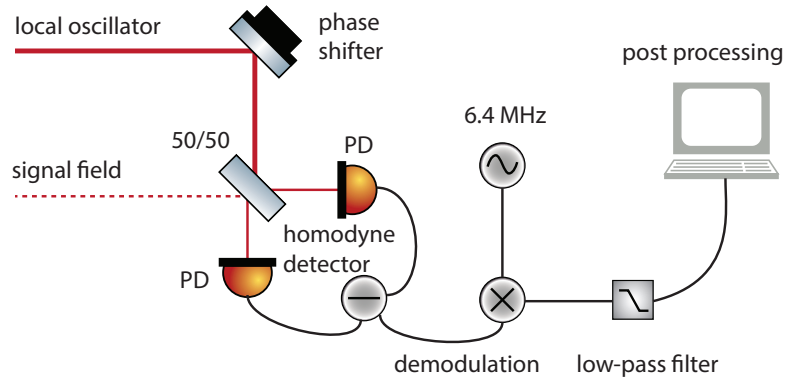


Figure 6.7: Data Acquisition. For the data acquisition the AC-currents of the photo diodes were subtracted, mixed with an electronic local oscillator at 6.4 MHz and low-pass filtered. An analog-to-digital conversion card recorded the data and a *LabView* program made the post-processing. The measured quadrature of the homodyne detector was also set by a *LabView* program.

tor HD_A and Bob's detector HD_D the entanglement between modes A and B' was checked by applying the Duan criterion (cf. Sec. 2.9) to the measured covariance matrix of the bipartite state.

6.4 Measurement Procedure

After all stabilization schemes for generating the squeezed and the thermal states and for setting their phases at the balanced beam splitter had been set, the following measurement procedure involved into two tasks: the reconstruction of the covariance matrix of the three-mode state to check for its requirements and the entanglement measurement. For these tasks the subtracted signal from both photo diodes of a homodyne detector was mixed with an electronic local oscillator at a frequency of 6.4 MHz. The resulting signal was low-pass filtered by a sixth order anti-alias filter with a corner frequency of 400 kHz. The data was sampled with the 14-bit analog-to-digital conversion card *PCI-6133* from National Instruments. For each measurement a total number of 10^6 data points was recorded and post-processed with a *LabView* program. The data acquisition is illustrated in Fig. 6.7.

6.4.1 Reconstruction of the Covariance Matrix

For checking the separability properties of the three-mode state, we measured the X , P , and the 45° quadratures of the modes A , B , and C in different combinations with

the stabilized homodyne detectors HD_A , HD_B , and HD_C , reconstructed the three-mode-state's covariance matrix and applied the PPT-criterion to the covariance matrix (cf. Sec. 2.9).

Table 6.1: Homodyne detector settings for the reconstruction of the three-mode covariance matrix.

setting #	HD_A	HD_B	HD_C
1	X_A	X_B	X_C
2	P_A	P_B	P_C
3	P_A	X_B	X_C
4	X_A	P_B	X_C
5	X_A	X_B	P_C
6	$X_A + P_A$	$X_B + P_B$	$X_C + P_C$

We performed measurements for six different settings of the detected quadratures, illustrated in Table 6.1. The measured quadratures of the different modes were stabilized using the single sideband and were set by a *LabView* program. First, we measured the variances of the amplitude quadratures X_j . In a second step we repeated the procedure for the phase quadratures P_j . In the third (fourth, fifth) step we determine the covariances of the phase quadrature P_A (P_B , P_C) with the amplitude quadratures of the other two modes. For determining the cross correlations of the three modes, we measured in a last step the quadratures at an angle of 45° , since we cannot measure different quadratures of the same mode simultaneously. The cross correlation of amplitude and phase quadrature of one stationary mode can be calculated by

$$\langle \hat{X}_j \hat{P}_j \rangle = \frac{1}{2} (\langle \hat{X}_j \hat{P}_j + \hat{P}_j \hat{X}_j \rangle) = \langle \hat{X}_j (45^\circ)^2 \rangle - \frac{1}{2} \langle (\hat{X}_j^2) + (\hat{P}_j^2) \rangle. \quad (6.1)$$

Details about this calculation can be found e.g. in [Sam12].

For calibration purposes we also performed a vacuum noise measurement. The entire reconstructed 6×6 covariance matrix γ consisted of the following entries

$$\gamma = \begin{pmatrix} \langle \hat{X}_A^2 \rangle & \langle \hat{X}_A \hat{P}_A \rangle & \langle \hat{X}_A \hat{X}_B \rangle & \langle \hat{X}_A \hat{P}_B \rangle & \langle \hat{X}_A \hat{X}_C \rangle & \langle \hat{X}_A \hat{P}_C \rangle \\ & \langle \hat{P}_A^2 \rangle & \langle \hat{P}_A \hat{X}_B \rangle & \langle \hat{P}_A \hat{P}_B \rangle & \langle \hat{P}_A \hat{X}_C \rangle & \langle \hat{P}_A \hat{P}_C \rangle \\ & & \langle \hat{X}_B^2 \rangle & \langle \hat{X}_B \hat{P}_B \rangle & \langle \hat{X}_B \hat{X}_C \rangle & \langle \hat{X}_B \hat{P}_C \rangle \\ & & & \langle \hat{P}_B^2 \rangle & \langle \hat{P}_B \hat{X}_C \rangle & \langle \hat{P}_B \hat{P}_C \rangle \\ & & & & \langle \hat{X}_C^2 \rangle & \langle \hat{X}_C \hat{P}_C \rangle \\ & & & & & \langle \hat{P}_C^2 \rangle \end{pmatrix} \quad (6.2)$$

For sake of readability we omitted the lower part of the covariance matrix since the matrix is symmetric.

6.4.2 Verifying the Entanglement

After the three-mode state had been measured and checked for its separability properties, mode C was sent to Bob and superimposed with mode B at the balanced beam splitter BS₃. The homodyne detectors at Alice and Bob measured the complete covariance matrix of the two-mode state AB', which corresponds in principle to the upper left 4 × 4-matrix from Eq. 6.2 if mode B is replaced by B'. Afterwards the Duan criterion was applied to the covariance matrix to check whether the two-mode state had been entangled.

6.5 Results

To investigate the required three-mode state we measured its covariance matrix with several different initial settings for the squeezed and thermal state. In the following our measurement results will be presented for different input states, i.e. for squeezed states with different squeezing and anti-squeezing values and for thermal states with different variances. For remembering the modes' and homodyne detector's names, a schematic of the setup is depicted in Fig. 6.8.

Measurement without the Thermal State

To show that the measurement procedure worked, we first generated the three-mode state without implementing the thermal state at the beam splitter BS₂. The advantage of this procedure was that we did not need a phase lock at the beam splitter BS₂ and we knew that we should measure a squeezed state at all homodyne detectors.

For this measurement we used a green pump field of about 90 mW for the squeezing generation and obtained a squeezed vacuum state with a noise reduction of -6.5 dB. With an entire optical loss of 38 % the resulting squeezed state had a noise reduction and amplification of -2.9,dB and 5 dB, respectively. The other two input states were vacuum states.

The reconstructed covariance matrix for that three-mode state reads

$$\gamma = \begin{pmatrix} 0.76 & 0.00 & 0.15 & 0.07 & 0.15 & 0.01 \\ 0.00 & 2.09 & 0.09 & -0.66 & 0.01 & -0.73 \\ 0.15 & 0.09 & 0.89 & -0.03 & -0.13 & -0.05 \\ 0.07 & -0.66 & -0.03 & 1.53 & -0.05 & 0.52 \\ 0.15 & 0.01 & -0.13 & -0.05 & 0.88 & 0.00 \\ 0.01 & -0.73 & -0.05 & 0.52 & 0.00 & 1.54 \end{pmatrix}. \quad (6.3)$$

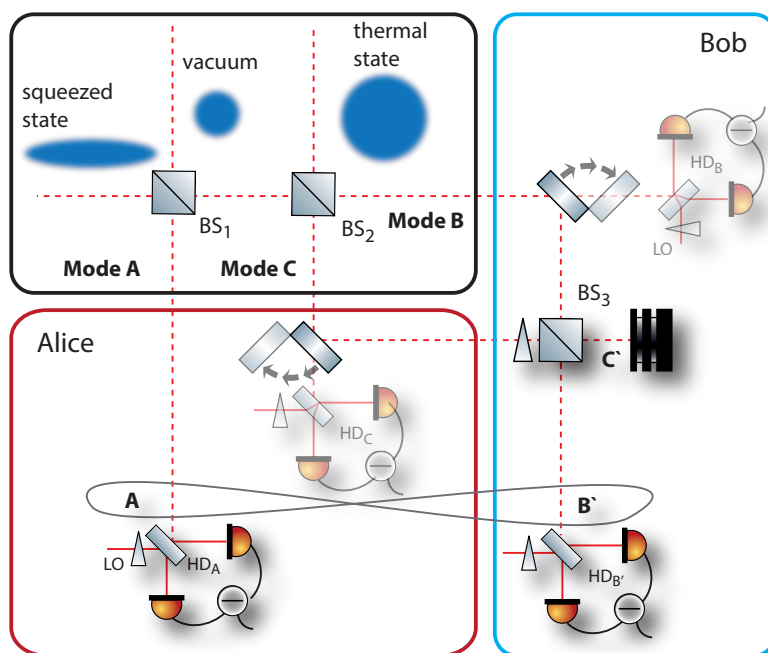


Figure 6.8: Schematic of the experimental setup. In the black box the three-mode state generation is depicted. Modes A and C were sent to Alice, while mode B was sent to Bob. If the homodyne detectors HD_A , HD_B , and HD_C measured the required three-mode state, mode C was sent to Bob, where it was superimposed at the balanced beam splitter BS_3 with mode B. The entanglement was checked with the Duan criterion with the homodyne detectors HD_A and $HD_{B'}$.

Since all variances of the amplitude quadrature are below 1, every homodyne detector measured a squeezed vacuum state as we had expected. The PPT values for the three-mode state were

$$\text{PPT}_A = 0.76, \quad \text{PPT}_B = 0.79, \quad \text{PPT}_C = 0.77. \quad (6.4)$$

Thus, the state was inseparable in all splittings. The measured Duan value for the distributed entanglement was $\mathcal{I} = 3.7 < 4$, which shows, that entanglement was distributed among Alice and Bob, though, with inseparable states.

Entanglement Distribution by Separable States

In a next step we also injected a thermal state with a variance of 9.6 dB in the amplitude quadrature and 10.2 dB in the phase quadrature. The squeezed vacuum state had -1.8 dB and 5.1 dB noise reduction/amplification in the amplitude and phase quadrature, respectively. The corresponding covariance matrix for the resulting three-mode state was given by

$$\gamma = \begin{pmatrix} 0.76 & 0.04 & 0.12 & -0.03 & 0.19 & -0.07 \\ 0.04 & 2.20 & 0.05 & -0.78 & -0.10 & -0.74 \\ 0.12 & 0.05 & 5.70 & -0.29 & -3.92 & 1.14 \\ -0.03 & -0.78 & -0.29 & 6.84 & -0.96 & -3.94 \\ 0.19 & -0.10 & -3.92 & -0.96 & 4.73 & 0.09 \\ -0.07 & -0.74 & 1.14 & -3.94 & 0.09 & 5.92 \end{pmatrix}, \quad (6.5)$$

and led to the PPT values

$$\text{PPT}_A = 0.89, \quad \text{PPT}_B = 1.1, \quad \text{PPT}_C = 1.07. \quad (6.6)$$

Thus, the three-mode state seems to be as required and can distribute entanglement by separable states. After we had turned the flip mirrors to distribute the entanglement, we measured a Duan value of $\mathcal{I} = 3.7$, which is below the threshold of 4. Thereby, the successful demonstration of entanglement distribution by separable states is shown. Considerations concerning the reliability of the measured values, especially due to homodyne losses, can be found in Sec. 6.6, where it is verified that we indeed distributed entanglement by separable states.

Table 6.2: Experimental Results for different squeezed input states. The text colors correspond to the crosses in Fig. 6.9.

#	Squeezing	Loss	PPT _B
1	7.2	38%	1.02
2	7.2	58%	1.06
3	6.6	60%	1.07

Variation of the Squeezed State

To show the influence of the squeezed state we varied the initial squeezing value and the losses applied to the state and kept the thermal state constant. The initial squeezing value was varied by using more or less pump power for the OPA to achieve a higher or lower gain and the losses were varied by a half-wave plate and a PBS, which the squeezed vacuum field had to pass. In Fig. 6.9 the theoretical values for such a variation are plotted. The colored crosses mark our measurements, whose details can be found in Table 6.2 with the corresponding text color. To obtain comparable results we subtracted the individual homodyne losses from the covariance matrix and used the PPT values obtained from this matrix. The variances of the thermal state we used for the theoretical simulation and within the experiments were 14 dB and 11 dB in the amplitude and phase quadrature, respectively. It is visible that our experimental results are in perfect agreement with the theoretical simulations. For this measurements we did not measure the resulting two-mode state to check the entanglement. However, due to the PPT values of the three-mode state and the already demonstrated success of distributing the entanglement, we knew that those states were suitable to distribute entanglement by separable states.

6.6 Discussion

On a first glance the measurement results show the successful demonstration of entanglement distribution by separable states. Also the results for different input states are in good agreement with theoretical simulations (cf. Fig. 6.9). However, we have to consider that three main effects can in principle cause masking the actual presence of entanglement in the B|CA and C|AB splitting or could make the three-mode state non-Gaussian. As illustrated in Fig. 6.10 these effects consists of the inefficient homodyne detection, phase fluctuations due to imperfect phase locking between signal beams and local oscillator beams, and the generation of the thermal state by random displacements of the originally squeezed quadrature where the distribution of random displacements may slightly deviate from a Gaussian distribution. In this section these effects will be considered in detail.

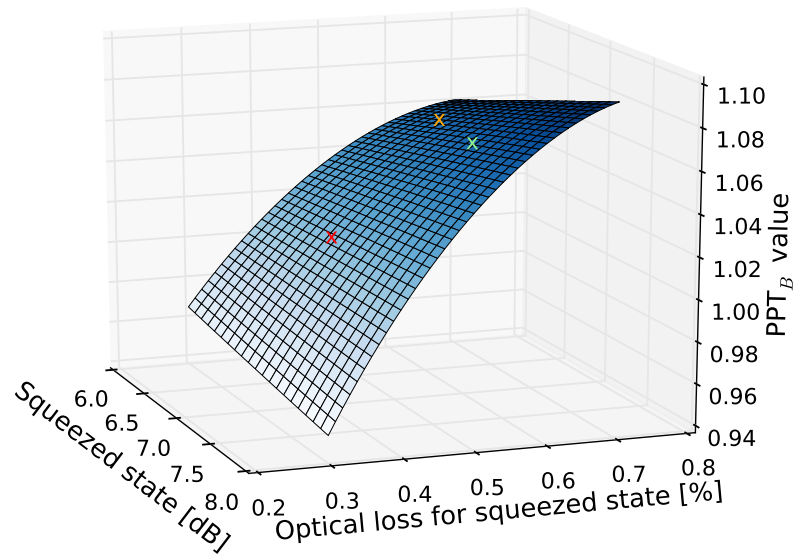


Figure 6.9: Variation of the squeezed input state. The blue and white surface shows the theoretical values for the PPT_B value with respect to the squeezed input state. We varied the squeezing parameter as well as the optical loss. The colored crosses mark our experimental results, whose details can be found in Table 6.2.

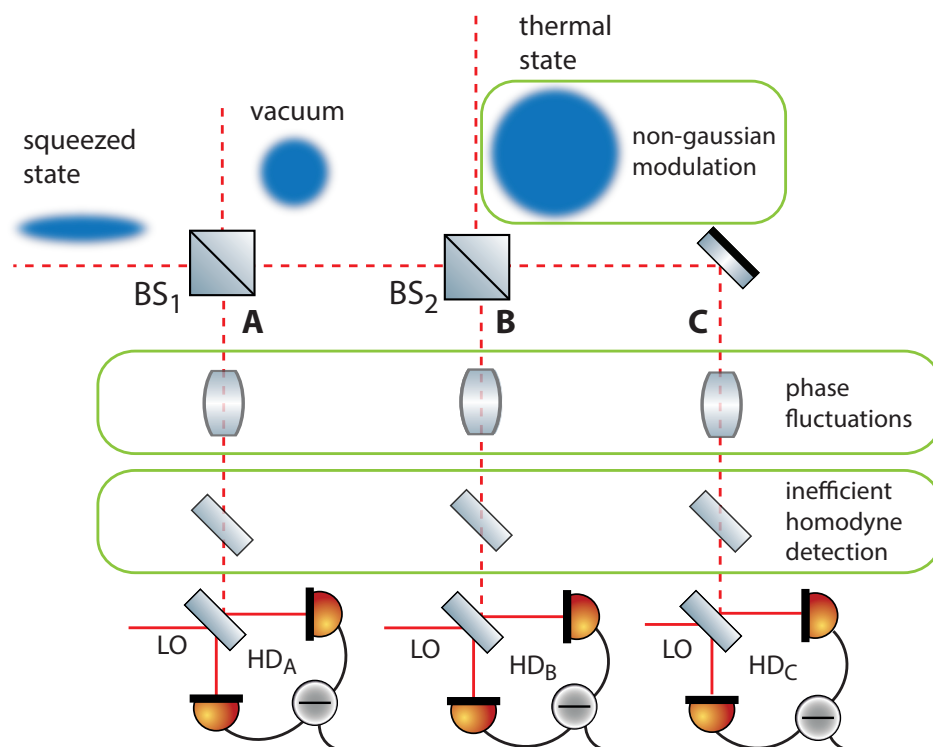


Figure 6.10: Experimental setup including effects that can potentially mask entanglement of the resulting three-mode state. After the preparation of the three-mode state each mode could be subject to phase fluctuations and losses. Phase fluctuations could occur due to imperfect phase stability between signal and local oscillator beams of the homodyne detection and to instabilities in locking schemes. A non-Gaussian modulation within the thermal state generation can also cause phase noise. Inefficient homodyne detection could mask the real properties in such a way that the initially inseparable state seems separable.

6.6.1 Inefficient Homodyne Detection

Since the three-mode state is probed with three balanced homodyne detectors and the covariance matrix of the state is determined from the homodyne data, we have to consider the effect of the homodyne detectors which are characterized by their efficiency η_i , $i \in \{A, B, C\}$. The efficiency is limited by the quantum efficiency of the photo diodes and the mode-matching of the signal field to the local oscillator (also called *visibility*). The detection loss can be simulated by the transmission through a lossy channel with transmission η . The reconstructed covariance matrix γ_m obtained from the measured data is then given by

$$\gamma_m = S_\eta \gamma_r S_\eta^T + G_\eta, \quad (6.7)$$

where γ_r denotes the covariance matrix without detection loss,

$$S_\eta = \begin{pmatrix} \sqrt{\eta_A} & 0 & 0 & 0 & 0 & 0 \\ 0 & \sqrt{\eta_A} & 0 & 0 & 0 & 0 \\ 0 & 0 & \sqrt{\eta_B} & 0 & 0 & 0 \\ 0 & 0 & 0 & \sqrt{\eta_B} & 0 & 0 \\ 0 & 0 & 0 & 0 & \sqrt{\eta_C} & 0 \\ 0 & 0 & 0 & 0 & 0 & \sqrt{\eta_C} \end{pmatrix}, \quad (6.8)$$

and $G_\eta = I - S_\eta S_\eta^T$ with the identity matrix I . By inverting Eq. 6.7 we obtain the real covariance matrix γ_r

$$\gamma_r = S_\eta^{-1} (\gamma_m - G_\eta) S_\eta^{T-1}. \quad (6.9)$$

The homodyne detector's inefficiency can cause that the three-mode state looks like the required one, however, the actual three-mode state without optical loss is inseparable in all splittings. This behavior is illustrated in Fig. 6.11, where the influence of detections loss on the PPT values for an arbitrary inseparable three-mode state is depicted. The three-mode state is actually inseparable in all splittings. However, if the detection loss exceeds 20%, the three-mode state seems to fulfill the requirements since it seems to be separable in the B|AC and C|AB splittings. Thus, we have to correct our measured covariance matrix for detection loss. For our measurement result in Eq. 6.4 we therefore have a look at the PPT_B and PPT_C value with respect to the homodyne detection loss as illustrated in Fig. 6.12. The magenta curves represent the PPT_B and PPT_C values of the covariance matrix γ , if optical loss within the homodyne detection is subtracted. The black vertical lines mark the regime of our estimated detection efficiency (quantum efficiency + visibility). We

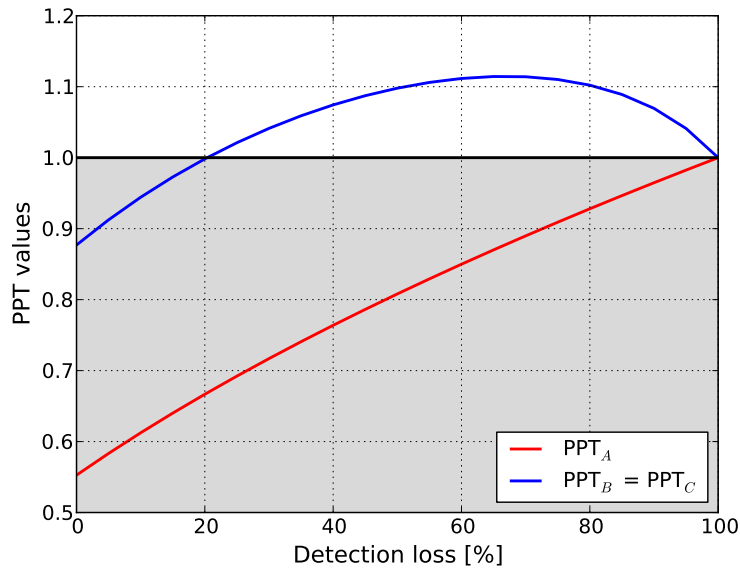


Figure 6.11: PPT values versus detection loss. Initially the three-mode state is inseparable in all splittings. If the homodyne detections suffer from loss which is greater than 20% each (for this example), the state seems to be separable in the $B|AC$ and $C|AB$ splittings.

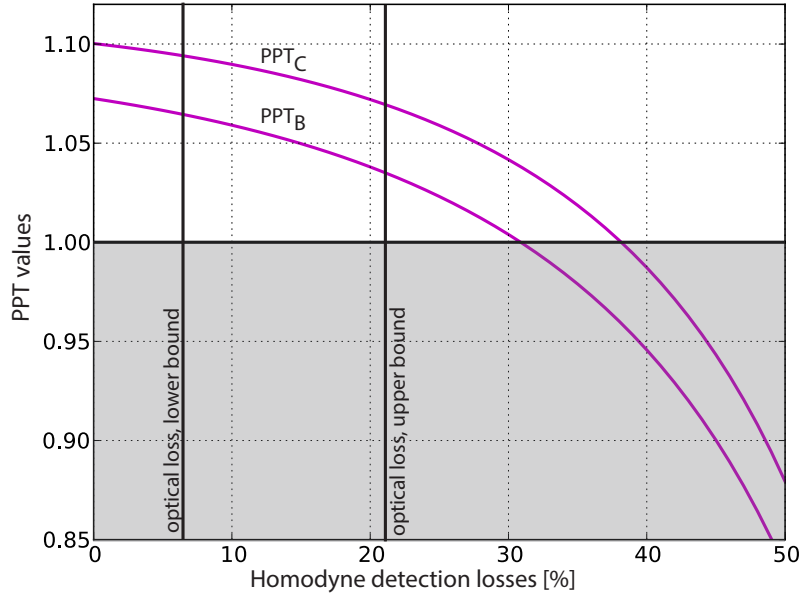


Figure 6.12: Measured PPT values with subtraction of detection loss. The magenta curves show the inferred PPT_B and PPT_C values of the measured covariance matrix for a spectrum of computationally eliminated detection losses. Based on independent measurements we estimate the actual detection loss to be greater 6% and smaller 22%. These losses do not push the PPT values below unity and, thus, into the inseparable regime.

estimated the quantum efficiency of the homodyne detector's photo diodes to be about 90%. The visibilities of the homodyne detectors were measured before each measurement and laid in a regime of 93–98%. Thus, for the covariance matrix γ the detection losses were $11\% \pm 5\%$ for the homodyne detector BHD_A , $17\% \pm 5\%$ for BHD_B and $16.6\% \pm 5\%$ for BHD_C , which leads to a lower bound of 6% and an upper bound of 22% loss. If we use the upper bounds for the detection loss we obtain the real covariance matrix for the measured data

$$\gamma_r = \begin{pmatrix} 0.71 & 0.05 & 0.15 & -0.04 & 0.23 & -0.09 \\ 0.05 & 2.43 & 0.06 & -0.96 & -0.12 & -0.91 \\ 0.15 & 0.06 & 7.03 & -0.37 & -5.01 & 1.46 \\ -0.04 & -0.96 & -0.37 & 8.49 & -1.23 & -5.04 \\ 0.23 & -0.12 & -5.01 & -1.23 & 5.76 & 0.11 \\ -0.09 & -0.91 & 1.46 & -5.04 & 0.11 & 7.28 \end{pmatrix}, \quad (6.10)$$

which lead to the PPT-values

$$\text{PPT}_A = 0.85, \quad \text{PPT}_B = 1.07, \quad \text{PPT}_C = 1.04. \quad (6.11)$$

This shows the correctness of the separability properties regardless whether the detection loss is considered to be part of the detected state or not. The same is also valid for all measured values presented in Table 6.2, where homodyne losses were already considered.

6.6.2 Phase Noise

Since all considerations and criteria we used are only valid for Gaussian states, we had to check the gaussianity of our measured data. In our setup we just have Gaussian operations. However, fluctuations of electronics (used for the stabilization loops or the thermal state generation) or of the beams itself can cause phase noise, which would lead to a non-Gaussian statistic. For verifying the gaussianity of the data we used a QQ-plot, which compares a measured distribution to a Gaussian one. Therefore, the sample quantiles of the data were plotted versus the theoretical quantiles of a perfect Gaussian distribution. Data with a Gaussian statistic are thus distributed along a straight line (representing a perfect Gaussian distribution), while data with phase noise deviates from such a distribution. In Fig. 6.13 three QQ-plots of the three homodyne detector's data are exemplarily shown for one data set of the measurements. Since the measured data (blue dots) does not significantly deviate from a perfect Gaussian distribution (red straight line) we can state that our measured data is indeed Gaussian.

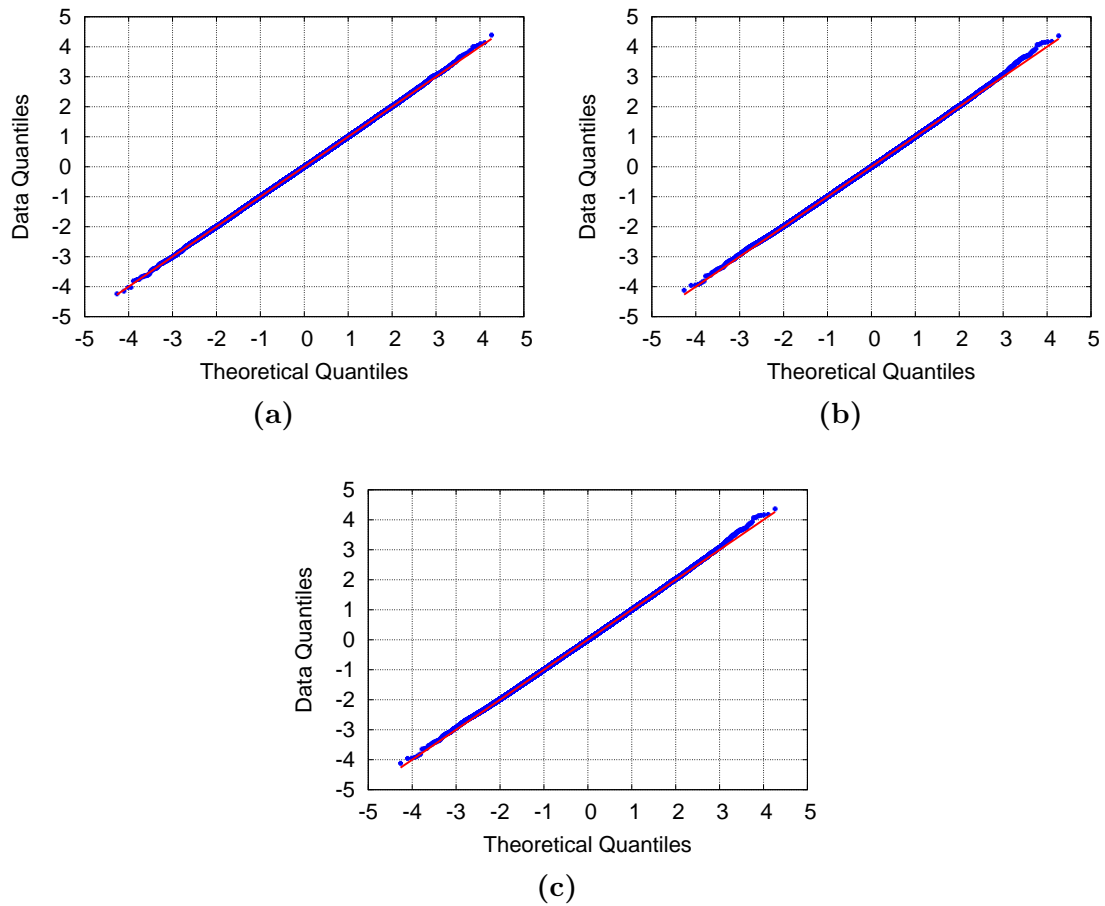


Figure 6.13: QQ-plots of the homodyne data. The three plots show the QQ-plot of one data set sampled with the three homodyne detectors. The blue dots mark the data points, while the red line represents a perfect Gaussian distribution. The figures show that there is no significant deviation from a Gaussian distribution, which demonstrates that there was no phase noise.

6.6.3 Statistical Errors

To determine the statistical errors of the symplectic eigenvalues PPT_j calculated from the estimated covariance matrices, a Monte Carlo simulation of the whole experiment was performed assuming Gaussian statistics of the measured quadratures. For each run of the Monte Carlo simulation we have reconstructed the covariance matrix and calculated the symplectic eigenvalues. This procedure was repeated 1000 times which provided a statistical ensemble for each estimate PPT_j . The mean values and statistical errors determined with the use of these ensembles read

$$\begin{aligned} \text{PPT}_A &= 0.849 \pm 0.001, \\ \text{PPT}_B &= 1.069 \pm 0.001, \\ \text{PPT}_C &= 1.036 \pm 0.001. \end{aligned} \tag{6.12}$$

This confirms that the statistical errors are very small compared to the deviations of PPT_j from 1. Hence, the observed separability properties are statistically significant.

6.7 Conclusion

In this chapter the experimental realization of entanglement distribution by separable states was demonstrated. It was shown that for this protocol a specific three-mode state is suitable, whose thermal noise prevented entanglement in two of the three bipartite splittings. After transmission of a separable state, entanglement was revealed via quantum interference. Simulations showed that the protocol does not work with Einstein–Podolsky–Rosen–entangled states, since with states of this class of entanglement, separability cannot be enforced by introducing thermal noise. By subtracting the detection loss of the covariance matrix it was verified that no disturbing effect masked the presence of entanglement and that actually separable states were used to distribute the entanglement. Furthermore, it was demonstrated that the data was Gaussian and, thus, the used criteria were valid to show the separability.

This experimental realization of a counterintuitive phenomena provides an insight into the underlying physical mechanism behind the protocol, such that this work can help to understand the possibilities and restrictions offered by multi-mode entangled quantum states and future multipartite quantum communication networks.

Its importance is also visible by the fact that two other demonstrations of entanglement distribution by separable states, with continuous as well as with discrete variables, respectively [Peu13, Fed13], were shown recently.

Conclusion

Future quantum networks require non-classical states of light and their successful distribution and detection. Therefore, a thorough knowledge about entanglement, multimode entanglement and its distribution is important as well as the efficient generation of non-classical states of light in the entire wavelength regime. This thesis presents what is currently the highest measured squeezed vacuum state of light at 532 nm corresponding to a -1.5 dB noise reduction. In addition, entanglement of -1.4 dB between squeezed vacuum states at 1550 nm and 532 nm, is demonstrated. In the second part of the thesis the successful distribution of entanglement by separable states of light is realized for the first time. The quantum up-conversion as well as the entanglement distribution by separable states are useful tools for future quantum engineering tasks.

Quantum Up-Conversion

With the technique of quantum up-conversion non-classical states of light can also be generated in the visible wavelength regime, in contrast to the convenient generation methods. In this thesis it was shown that squeezed and entangled states of light can be up-converted via sum-frequency generation. This process used a strong coherent pump field at 810 nm. Due to energy conservation the photons at 1550 nm got up-converted to 532 nm. A squeezed vacuum state with a noise reduction of -1.5 dB at 532 nm was thereby obtained and entanglement between 1550 nm and 532 nm with a Duan value of -1.4 dB was generated. The quantum properties were maintained during this process as already proposed in 1990 [Kum90] and experimentally shown via second harmonic generation in 1992 [Hua92]. However, with the technique of second harmonic generation no squeezed vacuum states could be generated. These states are mandatory for the improvement of the sensitivity of gravitational wave detectors [Sch10] and for quantum imaging beyond the stan-

dard quantum limit [Tre03, Bri10] since an additional carrier field would disturb the measurement sensitivity.

By means of quantum up-conversion it is also possible to generate other non-classical states of light, e.g. Schrödinger Kitten states. At the moment they can be generated in the infrared wavelength regime [Our06] by subtracting one single photon of a squeezed vacuum state, but with the presented technique of sum-frequency conversion they can be up-converted to the visible regime.

With the technique of frequency up-conversion, especially from the infrared to the visible wavelength regime, it is also possible to detect the transferred quantum states with a high efficiency, as commercially available single photon detectors are most efficient in the visible wavelength regime [Van04].

The generation of entanglement via sum-frequency generation provides a new scheme for establishing quantum links between different wavelengths. With such a technique the two important tasks in a quantum network, the transmission and the storage of information, can be simultaneously fulfilled.

Entanglement Distribution via Separable States

Cubitt et al. showed in 2003 that it is in principle possible to distribute entanglement with separable states [Cub03]. Mišta and Korolkova theoretically constructed the seemingly paradoxical protocol for the continuous variable regime [Miš08, Miš09]. The experimental realization was demonstrated for the first time within this thesis by the preparation of a specific three-mode state, which was separable in two of the three splittings [Vol13]. The three-mode state was composed of a squeezed state, a thermal state, a vacuum state, and two balanced beam splitter. The requirements for the initial states were investigated and it was found that the protocol cannot work if Einstein-Podolsky-Rosen entangled states as initial squeezed states are used, since their entanglement is too strong to be masked with thermal noise.

The three-mode state was checked for its separability properties by reconstructing the covariance matrix and applying the PPT criterion. It was verified that neither homodyne detection loss, nor phase noise masked any entanglement so that truly separable states were used to distribute entanglement between Alice and Bob.

With the experimental realization of the original protocol from Cubitt et al. the feasibility of such multipartite protocols was shown and our understanding grew deeper. Multimode or multipartite quantum states will play an important role for future protocols dealing with quantum teleportation [Bow03] and communication [Bra04] since they are a valuable resource for applications concerning quantum computing [Rau01, Wal05, Uka11].

Python Simulation

The following python simulation is the basis for all simulations, illustrations, and data analyses concerning the entanglement distribution by separable states.

```
import lab.analysis.tripartite as tripartite
import lab.analysis.covariance as bipartite
import lab.analysis.squeezing
from lab.analysis.covariance import dB2r
from numpy import *
```

```
# squeezing parameter
dB1=21 # amplitude quadrature thermal state
dB3=21 # phase quadrature thermal state
dB2=13 # amplitude quadrature squeezed state
```

```
# optical loss of the initial states
L_OPA1=0
L_OPA2=0.6
L_OPA3=0
# optical loss at phase gates
L_PG1=0.
L_PG2=0.1
L_PG3=0.00
# optical loss at homodyne detectors
L_HOMOA=0.2 #0.13
L_HOMOB=0.20
```

```

L_HOMOC=0.2 #0.33
L_HOMOD=0.2

# generation of the thermal state
# by superimposing the two squeezing ellipses 1 & 3
cm_thermal=bipartite.vacuum()
cm_thermal.squeeze(dB2r(dB1),0,dB2r(dB3),pi/2)
cm_thermal.opticalloss(L_OPA1,L_OPA3)
cm_thermal.entangle()
cm_thermal.opticalloss(L_PG1,L_PG1)

# generation of covariance matrix for the input states
cm_all=tripartite.vacuum()
# generation of squeezed vacuum state
cm_all.squeeze(((dB2r(dB2),pi/2),(0,0),(0,0)))
cm_all.opticalloss((L_OPA2,0,0))
cm_all[4:,4:]=cm_thermal[0:2,0:2]
# beam splitter BS1
cm_all.entangle(1,2)
#cm_all.rotate((pi/3,pi/4,0))
# check for entanglement after beam splitter BS1
cm_EPR1=bipartite.covariancematrix(cm_all[:4,:4])
cm_EPR1.opticalloss(L_HOMOA,L_HOMOB)
print cm_EPR1.duan()

# beam splitter BS2
cm_all.entangle(2,3)
cm_all.opticalloss((0,L_PG2,L_PG2))
# cm_all.rotate((pi/10,pi/10,pi/11))
# PPT criterion
print cm_all
print cm_all.PPT()

# optical loss at homodyne detectors
cm_detection=tripartite.covariancematrix(cm_all)
# cm_detection.rotate((pi/30,pi/20,pi/21))
cm_detection.opticalloss((L_HOMOA,L_HOMOC,L_HOMOD))
print cm_detection
savetxt("CM_EDS_TestSim.txt", cm_detection)

```

```
print cm_detection.PPT()

# send separable states to Bob, superimpose both modes
# at beam splitter BS3
cm_test=tripartite.covariancematrix(cm_all)
cm_test.rotate((0,0,pi))
cm_test.entangle(2,3)
cm_test.opticalloss((0,L_PG3,L_PG3))
cm_EPR=bipartite.covariancematrix(cm_test[:4,:4])
cm_EPR.opticalloss(L_HOMOA,L_HOMOB)
#measure distributed entanglement
print cm_EPR.duan()
```


Bibliography

- [App08] J. Appel, E. Figueroa, D. Korystov, M. Lobino and A. Lvovsky, “Quantum Memory for Squeezed Light,” *Physical Review Letters* **100**, 093602 (2008).
- [Asp82] A. Aspect, P. Grangier and G. Roger, “Experimental realization of Einstein-Podolsky-Rosen-Bohm Gedankenexperiment: a new violation of Bell’s inequalities,” *Physical review letters* **49**, 91 (1982).
- [Bel64] J. Bell, “On the Einstein-Podolsky-Rosen Paradox,” *Physics* **1**, 195 (1964).
- [Ben96] C. Bennett, G. Brassard and S. Popescu, “Purification of noisy entanglement and faithful teleportation via noisy channels,” *Physical Review Letters* **76**, 722 (1996).
- [Ber91] K. Bergman and H. A. Haus, “Squeezing in fibers with optical pulses.” *Optics letters* **16**, 663 (1991).
- [Bla01] E. D. Black, “An introduction to Pound–Drever–Hall laser frequency stabilization,” *American Journal of Physics* **69**, 79 (2001).
- [Bou97] D. Bouwmeester, J. Pan, K. Mattle, M. Eibl, H. Weinfurter and A. Zeilinger, “Experimental quantum teleportation,” *Nature* **390**, 575 (1997).
- [Bow03] W. P. Bowen, P. K. Lam and T. C. Ralph, “Biased EPR entanglement and its application to teleportation,” *Journal of Modern Optics* **50**, 801 (2003).
- [Boy08] R. W. Boyd, *Nonlinear Optics* (Academic Press, 2008), 3rd ed., ISBN 0123694701.
- [Bra04] S. L. Braunstein and P. Van Loock, “Quantum information with continuous variables,” *Reviews of Modern Physics* **77**, 513 (2004).

- [Bra07] E. Brambilla, L. Caspani, O. Jedrkiewicz, L. A. Lugiato and A. Gatti, “High-sensitivity imaging with multi-mode twin beams,” *Physical Review A* **77**, 13 (2007).
- [Bri98] H. Briegel, W. Dür, J. Cirac and P. Zoller, “Quantum repeaters: The role of imperfect local operations in quantum communication,” *Physical Review Letters* **81**, 5932 (1998).
- [Bri10] G. Brida, M. Genovese and I. Berchera, “Experimental realization of sub-shot-noise quantum imaging,” *Nature Photonics* **4**, 227 (2010).
- [Cav81] C. Caves, “Quantum-mechanical noise in an interferometer,” *Physical Review D* **28** (1981).
- [Cer01] N. Cerf, M. Lévy and G. Assche, “Quantum distribution of Gaussian keys using squeezed states,” *Physical Review A* **63**, 052311 (2001).
- [Che07] S. Chelkowski, H. Vahlbruch, K. Danzmann and R. Schnabel, “Coherent control of broadband vacuum squeezing,” *Physical Review A* **75**, 1 (2007).
- [Chi06] L. Childress, J. Taylor, A. Sørensen and M. Lukin, “Fault-Tolerant Quantum Communication Based on Solid-State Photon Emitters,” *Physical Review Letters* **96**, 070504 (2006).
- [Cho08] K. S. Choi, H. Deng, J. Laurat and H. J. Kimble, “Mapping photonic entanglement into and out of a quantum memory.” *Nature* **452**, 67 (2008).
- [Chr13] A. Christ, B. Brecht, W. Mauerer and C. Silberhorn, “Theory of quantum frequency conversion and type-II parametric down-conversion in the high-gain regime,” *New Journal of Physics* **15**, 053038 (2013).
- [Chu12] T. K. Chuan, J. Maillard, K. Modi, T. Paterek, M. Paternostro and M. Piani, “Quantum Discord Bounds the Amount of Distributed Entanglement,” *Physical Review Letters* **109**, 070501 (2012).
- [Cub03] T. Cubitt, F. Verstraete, W. Dür and J. Cirac, “Separable States Can Be Used To Distribute Entanglement,” *Physical Review Letters* **91**, 037902 (2003).
- [DiG07] J. DiGuglielmo, B. Hage, A. Franzen, J. Fiurášek and R. Schnabel, “Experimental characterization of Gaussian quantum-communication channels,” *Physical Review A* **76**, 012323 (2007).

- [Don08] R. Dong, M. Lassen, J. Heersink, R. Filip, G. Leuchs and U. L. Andersen, “Experimental entanglement distillation of mesoscopic quantum states,” *Nature Photonics* **4**, 919 (2008).
- [Dua00] L. Duan, G. Giedke, J. Cirac and P. Zoller, “Inseparability criterion for continuous variable systems,” *Physical review letters* **84**, 2722 (2000).
- [Dua01] L. M. Duan, M. D. Lukin, J. I. Cirac and P. Zoller, “Long-distance quantum communication with atomic ensembles and linear optics,” *Nature* **414**, 413 (2001).
- [Ebe10] T. Eberle, S. Steinlechner, J. Bauchrowitz, V. Händchen, H. Vahlbruch, M. Mehmet, H. Müller-Ebhardt and R. Schnabel, “Quantum Enhancement of the Zero-Area Sagnac Interferometer Topology for Gravitational Wave Detection,” *Physical Review Letters* **104**, 251102 (2010).
- [Ebe11] T. Eberle, V. Händchen, J. Duhme, T. Franz, R. F. Werner and R. Schnabel, “Strong Einstein-Podolsky-Rosen entanglement from a single squeezed light source,” *Physical Review A* **83**, 052329 (2011).
- [Ebe13] T. Eberle, “Realization of Finite-Size Quantum Key Distribution based on Einstein-Podolsky-Rosen Entangled Light,” Dissertation, University of Hannover (2013).
- [Eck91] R. Eckardt, C. Nabors, W. Kozlovsky and R. Byer, “Optical parametric oscillator frequency tuning and control,” *JOSA B* **8**, 646 (1991).
- [Ein35] A. Einstein, B. Podolsky and N. Rosen, “Can quantum-mechanical description of physical reality be considered complete?” *Physical review* **47**, 777 (1935).
- [Fed13] A. Fedrizzi, M. Zuppardo and G. Gillett, “Experimental distribution of entanglement via separable states,” *arXiv preprint arXiv:1303.4634* (2013).
- [Fej92] M. Fejer, G. Magel, D. Jundt and R. Byer, “Quasi-phase-matched second harmonic generation: tuning and tolerances,” *IEEE Journal of Quantum Electronics* **28**, 2631 (1992).
- [FG13] X. Fernandez-Gonzalvo and G. Corrielli, “Quantum frequency conversion of quantum memory compatible photons to telecommunication wavelengths,” *Optics Express* **21**, 19473 (2013).

- [Fiu07] J. Fiurásek, P. Marek, R. Filip and R. Schnabel, “Experimentally feasible purification of continuous-variable entanglement,” *Physical Review A* **75**, 050302 (2007).
- [Fur98] A. Furusawa, J. L. Sørensen, S. L. Braunstein, C. A. Fuchs, H. Kimble and E. S. Polzik, “Unconditional Quantum Teleportation,” *Science* **282**, 706 (1998).
- [Fur12] F. Furrer, T. Franz, M. Berta, A. Leverrier, V. B. Scholz, M. Tomamichel and R. F. Werner, “Continuous Variable Quantum Key Distribution: Finite-Key Analysis of Composable Security against Coherent Attacks,” *Physical Review Letters* **109**, 100502 (2012).
- [Ger10] C. Gerry and P. Knight, *Introductory Quantum Optics* (Cambridge University Press, 2010), ISBN 052152735.
- [Gie01] G. Giedke, B. Kraus, M. Lewenstein and J. I. Cirac, “Separability Properties of Three-mode Gaussian States,” *Physical Review A* **64**, 11 (2001).
- [Gla63] R. Glauber, “Coherent and incoherent states of the radiation field,” *Physical Review* **131**, 2766 (1963).
- [Gob04] C. Gobby, Z. L. Yuan and A. J. Shields, “Quantum key distribution over 122 km of standard telecom fiber,” *Applied Physics Letters* **84**, 3762 (2004).
- [Gra68] R. Graham and H. Haken, “The quantum-fluctuations of the optical parametric oscillator. I,” *Zeitschrift für Physik* **210**, 276 (1968).
- [Gro13] H. Grote, K. Danzmann, K. Dooley, R. Schnabel, J. Slutsky and H. Vahlbruch, “First Long-Term Application of Squeezed States of Light in a Gravitational-Wave Observatory,” *Physical Review Letters* **110**, 181101 (2013).
- [Hag08] B. Hage, A. Samblowski, J. DiGuglielmo, A. Franzen, J. Fiurásek and R. Schnabel, “Preparation of distilled and purified continuous variable entangled states,” *Nature Physics* **4**, 915 (2008).
- [Hag10a] B. Hage, “Purification and Distillation of Continuous Variable Entanglement,” Dissertation, Leibniz Universität Hannover (2010).
- [Hag10b] B. Hage, A. Samblowski and R. Schnabel, “Towards Einstein-Podolsky-Rosen quantum channel multiplexing,” *Physical Review A* **81**, 062301 (2010).

-
- [Hed10] M. P. Hedges, J. J. Longdell, Y. Li and M. J. Sellars, “Efficient quantum memory for light.” *Nature* **465**, 1052 (2010).
- [Hon08] K. Honda, D. Akamatsu, M. Arikawa, Y. Yokoi, K. Akiba, S. Nagatsuka, T. Tanimura, A. Furusawa and M. Kozuma, “Storage and Retrieval of a Squeezed Vacuum,” *Physical Review Letters* **100**, 093601 (2008).
- [Hor97] P. Horodecki, “Separability criterion and inseparable mixed states with positive partial transposition,” *Physics Letters A* **232**, 333 (1997).
- [Hor09] R. Horodecki, M. Horodecki and K. Horodecki, “Quantum entanglement,” *Reviews of Modern Physics* **81**, 865 (2009).
- [How04] J. C. Howell, R. S. Bennink, S. J. Bentley and R. W. Boyd, “Realization of the Einstein-Podolsky-Rosen Paradox Using Momentum- and Position-Entangled Photons from Spontaneous Parametric Down Conversion,” *Physical Review Letters* **92**, 210403 (2004).
- [Hua92] J. Huang and P. Kumar, “Observation of quantum frequency conversion,” *Physical Review Letters* **68**, 2153 (1992).
- [Iku12] R. Ikuta, H. Kato, Y. Kusaka, S. Miki, T. Yamashita, H. Terai, M. Fujiwara, T. Yamamoto, M. Koashi, M. Sasaki, Z. Wang and N. Imoto, “High-fidelity conversion of photonic quantum information to telecommunication wavelength with superconducting single-photon detectors,” *arXiv* 1207.1585 (2012).
- [Jia04] X. Jia, X. Su, Q. Pan, J. Gao, C. Xie and K. Peng, “Experimental Demonstration of Unconditional Entanglement Swapping for Continuous Variables,” *Physical Review Letters* **93**, 250503 (2004).
- [Jul04] B. Julsgaard, J. Sherson, J. I. Cirac, J. Fiurásek and E. S. Polzik, “Experimental demonstration of quantum memory for light,” *Nature* **432**, 482 (2004).
- [Kam08] H. Kamada, M. Asobe, T. Honjo, H. Takesue, Y. Tokura, Y. Nishida, O. Tadanaga and H. Miyazawa, “Efficient and low-noise single-photon detection in 1550 nm communication band by frequency upconversion in periodically poled LiNbO₃ waveguides,” *Optics letters* **33**, 639 (2008).
- [Kaw11] S. Kawamura, M. Ando, N. Seto, S. Sato, T. Nakamura, K. Tsubono, N. Kanda, T. Tanaka, J. Yokoyama, I. Funaki, K. Numata, K. Ioka, T. Takashima, K. Agatsuma, T. Akutsu, K.-s. Aoyanagi, K. Arai,

- A. Araya, H. Asada, Y. Aso, D. Chen, T. Chiba, T. Ebisuzaki, Y. Ejiri, M. Enoki, Y. Eriguchi, M.-K. Fujimoto, R. Fujita, M. Fukushima, T. Futamase, T. Harada, T. Hashimoto, K. Hayama, W. Hikida, Y. Himemoto, H. Hirabayashi, T. Hiramatsu, F.-L. Hong, H. Horisawa, M. Hosokawa, K. Ichiki, T. Ikegami, K. T. Inoue, K. Ishidoshiro, H. Ishihara, T. Ishikawa, H. Ishizaki, H. Ito, Y. Itoh, K. Izumi, I. Kawano, N. Kawashima, F. Kawazoe, N. Kishimoto, K. Kiuchi, S. Kobayashi, K. Kohri, H. Koizumi, Y. Kojima, K. Kokeyama, W. Kokuyama, K. Kotake, Y. Kozai, H. Kunimori, H. Kuninaka, K. Kuroda, S. Kuroyanagi, K.-i. Maeda, H. Matsuhara, N. Matsumoto, Y. Michimura, O. Miyakawa, U. Miyamoto, S. Miyoki, M. Y. Morimoto, T. Morisawa, S. Moriwaki, S. Mukohyama, M. Musha, S. Nagano, I. Naito, K. Nakamura, H. Nakano, K. Nakao, S. Nakasuka, Y. Nakayama, K. Nakazawa, E. Nishida, K. Nishiyama, A. Nishizawa, Y. Niwa, T. Noumi, Y. Obuchi, M. Ohashi, N. Ohishi, M. Ohkawa, K. Okada, N. Okada, K. Oohara, N. Sago, M. Saijo, R. Saito, M. Sakagami, S.-i. Sakai, S. Sakata, M. Sasaki, T. Sato, M. Shibata, H. Shinkai, A. Shoda, K. Somiya, H. Sotani, N. Sugiyama, Y. Suwa, R. Suzuki, H. Tagoshi, F. Takahashi, K. Takahashi, K. Takahashi, R. Takahashi, R. Takahashi, T. Takahashi, H. Takahashi, T. Akiteru, T. Takano, N. Tanaka, K. Taniguchi, A. Taruya, H. Tashiro, Y. Torii, M. Toyoshima, S. Tsujikawa, Y. Tsunesada, A. Ueda, K.-i. Ueda, M. Utashima, Y. Wakabayashi, K. Yagi, H. Yamakawa, K. Yamamoto, T. Yamazaki, C.-M. Yoo, S. Yoshida, T. Yoshino and K.-X. Sun, “The Japanese space gravitational wave antenna: DECIGO,” *Classical and Quantum Gravity* **28**, 094011 (2011).
- [Kay12] A. Kay, “Using Separable Bell-Diagonal States to Distribute Entanglement,” *Physical Review Letters* **109**, 080503 (2012).
- [Kha11] A. Khalaidovski, “Beyond the Quantum Limit,” Dissertation, Leibniz University Hannover (2011).
- [Kim02] M. S. Kim, W. Son, V. Bužek and P. L. Knight, “Entanglement by a beam splitter: Nonclassicality as a prerequisite for entanglement,” *Physical Review A* **65**, 032323 (2002).
- [Kim08] H. Kimble, “The quantum internet,” *Nature* **453**, 1 (2008).
- [Koe06] W. Koechner, *Solid-State Laser Engineering (Springer Series in Optical Sciences)* (Springer, 2006), ISBN 038729094X.
- [Koz00] A. Kozhekin, K. Mølmer and E. Polzik, “Quantum memory for light,” *Physical review* **62**, 033809 (2000).

- [Kum90] P. Kumar, “Quantum frequency conversion,” *Optics letters* **15**, 1476 (1990).
- [Kür93] P. Kürz and R. Paschotta, “Bright squeezed light by second-harmonic generation in a monolithic resonator,” *EPL (Europhysics Letters)* **24** (1993).
- [Kwi99] P. G. Kwiat, E. Waks, A. G. White, I. Appelbaum and P. H. Eberhard, “Ultrabright source of polarization-entangled photons,” *Physical Review A* **60**, R773 (1999).
- [Las10] N. Lastzka, “Numerical modelling of classical and quantum effects in nonlinear optical systems,” Dissertation, Leibniz Universität Hannover (2010).
- [Leo08] U. Leonhardt, *Measuring the Quantum State of Light (Cambridge Studies in Modern Optics)* (Cambridge University Press, 2008), ISBN 0521023521.
- [Li08] M.-J. Li and D. A. Nolan, “Optical Transmission Fiber Design Evolution,” *Journal of Lightwave Technology* **26**, 1079 (2008).
- [Lou00] B. Lounis and W. E. Moerner, “Single photons on demand from a single molecule at room temperature,” *Nature* **407**, 491 (2000).
- [Lvo09] A. I. Lvovsky, B. C. Sanders and W. Tittel, “Optical quantum memory,” *Nature Photonics* **3**, 706 (2009).
- [McG10] H. J. McGuinness, M. G. Raymer, C. J. McKinstrie and S. Radic, “Quantum Frequency Translation of Single-Photon States in a Photonic Crystal Fiber,” *Physical Review Letters* **105**, 093604 (2010).
- [Meh11] M. Mehmet, S. Ast, T. Eberle, S. Steinlechner, H. Vahlbruch and R. Schnabel, “Squeezed light at 1550 nm with a quantum noise reduction of 12.3 dB,” *Optics Express* **19**, 25763 (2011).
- [Mej12] L. Mejling, C. J. McKinstrie, M. G. Raymer and K. Rottwitt, “Quantum frequency translation by four-wave mixing in a fiber : low-conversion regime,” *Optics Express* **20**, 695 (2012).
- [Miš08] L. Mišta and N. Korolkova, “Distribution of continuous-variable entanglement by separable Gaussian states,” *Physical Review A* **77**, 050302 (2008).
- [Miš09] L. Mišta and N. Korolkova, “Improving continuous-variable entanglement distribution by separable states,” *Physical Review A* **80**, 032310 (2009).

- [Nel65] J. Nelder and R. Mead, “A simplex method for function minimization,” *The Computer Journal* **7**, 308 (1965).
- [NN06] J. Neergaard-Nielsen, B. Nielsen, C. Hettich, K. Mølmer and E. Polzik, “Generation of a Superposition of Odd Photon Number States for Quantum Information Networks,” *Physical Review Letters* **97**, 083604 (2006).
- [Ou92] Z. Ou, S. Pereira, H. Kimble and K. Peng, “Realization of the Einstein-Podolsky-Rosen paradox for continuous variables,” *Physical Review Letters* **68**, 3663 (1992).
- [Our06] A. Ourjoumtsev, R. Tualle-Brouri, J. Laurat and P. Grangier, “Generating optical Schrödinger kittens for quantum information processing,” *Science* **312**, 83 (2006).
- [Pel12] J. S. Pelc, Q. Zhang, C. R. Phillips, L. Yu, Y. Yamamoto and M. M. Fejer, “Cascaded frequency upconversion for high-speed single-photon detection at 1550 nm,” *Optics Letters* **37**, 476 (2012).
- [Per96] A. Peres, “Separability criterion for density matrices,” *Physical Review Letters* **77**, 1413 (1996).
- [Peu13] C. Peuntinger, V. Chille, L. Mišta, N. Korolkova, M. Förtsch, J. Korger, C. Marquardt and G. Leuchs, “Distributing entanglement with separable states,” *arXiv preprint arXiv: 1304.0504* (2013).
- [Pol92] E. Polzik, J. Carri and H. J. Kimble, “Spectroscopy with squeezed light,” *Physical Review Letters* **68**, 3020 (1992).
- [Rau01] R. Raussendorf and H. J. Briegel, “A One-Way Quantum Computer,” *Physical Review Letters* **86**, 5188 (2001).
- [Sag11] E. Saglamyurek, N. Sinclair, J. Jin, J. A. Slater, D. Oblak, F. Bussières, M. George, R. Ricken, W. Sohler and W. Tittel, “Broadband waveguide quantum memory for entangled photons,” *Nature* **469**, 512 (2011).
- [Sam11] A. Sambrowski, C. E. Laukötter, N. Grosse, P. K. Lam and R. Schnabel, “Two Color Entanglement,” *AIP Conference Proceedings* **1363** (2011).
- [Sam12] A. Sambrowski, “State Preparation for Quantum Information Science and Metrology,” Dissertation, Leibniz Universität Hannover (2012).

- [Sam13] A. Sambrowski, C. E. Vollmer, C. Baune, J. Fiurášek and R. Schnabel, “Weak-signal conversion from 1550nm to 532nm with 84% efficiency,” *arXiv:1310.0712* (2013).
- [San11] N. Sangouard, C. Simon, H. de Riedmatten and N. Gisin, “Quantum repeaters based on atomic ensembles and linear optics,” *Reviews of Modern Physics* **83**, 33 (2011).
- [Sas11] M. Sasaki, M. Fujiwara, H. Ishizuka, W. Klaus, K. Wakui and E. Al., “QKD in Standard Optical Telecommunications Networks,” *Optics Express* **19**, 10387 (2011).
- [Sch35] E. Schrödinger, “Discussion of Probability Relations Between Separated Systems,” *Proc. Camb. Phil. Soc.* **47**, 555 (1935).
- [Sch01] W. P. Schleich, *Quantum Optics in Phase Space* (Wiley-VCH, 2001), ISBN 352729435.
- [Sch10] R. Schnabel, N. Mavalvala, D. E. McClelland and P. K. Lam, “Quantum metrology for gravitational wave astronomy.” *Nature Communications* **1**, 121 (2010).
- [Sim94] R. Simon, N. Mukunda and B. Dutta, “Quantum-noise matrix for multi-mode systems: U (n) invariance, squeezing, and normal forms,” *Physical Review A* **49**, 1567 (1994).
- [Sim00] R. Simon, “Peres-horodecki separability criterion for continuous variable systems,” *Physical Review Letters* **84**, 2726 (2000).
- [Ste13] S. Steinlechner, J. Bauchrowitz, T. Eberle and R. Schnabel, “Strong continuous variable EPR-steering with a detection efficiency above 96%,” *Physical Review A* **87**, 022104 (2013).
- [Tay13] M. A. Taylor, J. Janousek, V. Daria, J. Knittel, B. Hage, H.-A. Bachor and W. P. Bowen, “Biological measurement beyond the quantum limit,” *Nature Photonics* **7**, 229 (2013).
- [The11] The LSC, “A gravitational wave observatory operating beyond the quantum shot-noise limit,” *Nature Physics* **7**, 962 (2011).
- [Tit09] W. Tittel, M. Afzelius, T. Chanelière, R. Cone, S. Kröll, S. Moiseev and M. Sellars, “Photon-echo quantum memory in solid state systems,” *Laser & Photonics Reviews* **4**, 244 (2009).

- [Tre03] N. Treps, N. Grosse, W. P. Bowen, C. Fabre, H.-A. Bachor and P. K. Lam, “A quantum laser pointer,” *Science (New York, N.Y.)* **301**, 940 (2003).
- [Tsu95] H. Tsuchida, “Generation of amplitude-squeezed light at 431 nm from a singly resonant frequency doubler.” *Optics Letters* **20**, 2240 (1995).
- [Żu93] M. Żukowski, A. Zeilinger, M. Horne and A. Ekert, “Event-ready-detectors” Bell experiment via entanglement swapping,” *Physical Review D* **71**, 4287 (1993).
- [Uka11] R. Ukai, N. Iwata, Y. Shimokawa, S. C. Armstrong, A. Politi, J.-i. Yoshikawa, P. van Loock and A. Furusawa, “Demonstration of Unconditional One-Way Quantum Computations for Continuous Variables,” *Physical Review Letters* **106**, 240504 (2011).
- [Van04] A. P. Vandevender and P. G. Kwiat, “High efficiency single photon detection via frequency up-conversion,” *Journal of Modern Optics* **51**, 1433 (2004).
- [Vid01] G. Vidal and R. Werner, “A computable measure of entanglement,” *Physical Review A* **65**, 032314 (2001).
- [Vil05] A. Villar, L. Cruz, K. Cassemiro, M. Martinelli and P. Nussenzveig, “Generation of Bright Two-Color Continuous Variable Entanglement,” *Physical Review Letters* **95**, 243603 (2005).
- [Vol13] C. Vollmer, D. Schulze, T. Eberle, V. Händchen, J. Fiurášek and R. Schnabel, “Experimental entanglement distribution by separable states,” *arXiv preprint arXiv: 1303.1082* (2013).
- [Wal05] P. Walther, K. J. Resch, T. Rudolph, E. Schenck, H. Weinfurter, V. Vedral, M. Aspelmeyer and A. Zeilinger, “Experimental one-way quantum computing.” *Nature* **434**, 169 (2005).
- [Wal10] D. Walls and G. J. Milburn, *Quantum Optics* (Springer, 2010), ISBN 3642066763.
- [Wee12] C. Weedbrook, S. Pirandola, R. García-Patrón, N. Cerf, T. Ralph, J. Shapiro and S. Lloyd, “Gaussian quantum information,” *Reviews of Modern Physics* **84**, 621 (2012).
- [Wer00] R. F. Werner and M. M. Wolf, “Bound entangled Gaussian states,” *Physical Review Letters* **86**, 3658 (2000).

- [Wig32] E. Wigner, “On the quantum correction for thermodynamic equilibrium,” *Physical Review* **40**, 749 (1932).
- [Yar89] A. Yariv, *Quantum Electronics* (John Wiley & Sons, 1989), ISBN 0471609978.
- [Zha03] Z. Zhao, T. Yang, Y.-A. Chen, A.-N. Zhang, M. Żukowski and J.-W. Pan, “Experimental Violation of Local Realism by Four-Photon Greenberger-Horne-Zeilinger Entanglement,” *Physical Review Letters* **91**, 180401 (2003).

List of Publications

2013

1. **C. E. Vollmer**, D. Schulze, T. Eberle, V. Händchen, J. Fiurášek, R. Schnabel, “Experimental Entanglement Distribution by Separable States”, *Phys. Rev. Lett.* **111**, 230505
2. **C. E. Vollmer**, C. Baune, A. Samblowski, T. Eberle, V. Händchen, J. Fiurášek, R. Schnabel, “Quantum Up-Conversion of Squeezed Vacuum States from 1550 nm to 532 nm”, accepted in *Physical Review Letters*
3. A. Samblowski, **C. E. Vollmer**, C. Baune, J. Fiurášek, R. Schnabel, “Weak-signal conversion from 1550 nm to 532 nm with 84% efficiency”, *arXiv preprint 1310.0712*, submitted to *Optics Letters*

2011

4. A. Samblowski, **C. E. Laukötter**, N. Grosse, P. K. Lam, R. Schnabel, “Two Color Entanglement”, *AIP Conference Proceedings* **1363**, 219

Acknowledgments

During the time I worked at the Albert Einstein Institute and conducted the experiments for my thesis I was surrounded by many great people, who has helped me both in and out of the Lab. Without them, I would have not been able to write this thesis in this form. I want to thank all of them! Especially:

Karsten Danzmann, for establishing this great institute, where the conditions for working, and sometimes also for living, are incredibly good.

Roman Schnabel, for supervising and supporting me in the last few years. It was great to be a member of your team.

Jaromir Fiurášek, for fruitful discussions and the theoretical basis for all of the experiments.

To the staff of the mechanical and electronic workshops, the IT guys, and the secretarial staff for helping me immediately with problems both large and small.

All people who worked with me on the experiments: Christoph Baune, Aiko Samblowski, Petrisa Zell, and Sacha Kocsis, who have built up and discussed the experiments for quantum up-conversion with me. The experimental entanglement distribution by separable states was a collaboration with Daniela Schulze as part of her master thesis. Tobias Gehring, né Eberle, and Vitus Händchen were my office and lab colleagues and supported me in every field. I really enjoyed working, discussing, and laughing with all of you!

Christoph Baune, Tobias Gehring, Rieke Heinze, Sacha Kocsis, Aiko Samblowski, and Daniela Schulze for proof-reading this thesis.

Meinen Freunden, die mir immer zuhörten, meine Begeisterung teilten und, falls nötig, die richtigen Worte fanden, um mich wieder aufzubauen.

Meiner Familie, die mich immer und überall unterstützt und ermutigt hat. Euer großes Vertrauen in mich hat mir immer den Rücken gestärkt. Ganz besonders möchte ich meinem Mann Sebastian danken: für deine grenzenlose Hilfe, die Kraft, die du mir immer wieder gegeben hast, und all die Dinge, die nicht in Worte gefasst werden können (oder manchmal in ein einziges ...).

THANK YOU!

